

AIX-MARSEILLE UNIVERSITÉ  
ECOLE DOCTORALE DES SCIENCES DE LA VIE ET DE  
LA SANTE

Thesis presented to obtain the degree of Doctor of Philosophy

Discipline: Biology  
Speciality: Developpmental biology

Weiyuan KONG

Mechanical measurements across scales in 2D and 3D  
during epithelial morphogenesis

Mesures mécaniques à travers les échelles en 2D et 3D pendant la morphogénèse  
épithéliale

Under the supervision of Pierre-François LENNE & Raphaël CLEMENT

Defense on 23/06/2021 before the jury composed of:

Isabelle BONNET	Reviewer
Cyprien GAY	Reviewer
Magali SUZANNE	Examiner
Olivier THEODOLY	Examiner
Pierre-François LENNE	Thesis supervisor
Raphaël CLEMENT	Thesis supervisor



Cette oeuvre est mise à disposition selon les termes de la [Licence Creative Commons Attribution - Pas d'Utilisation Commerciale - Pas de Modification 4.0 International](https://creativecommons.org/licenses/by-nc-nd/4.0/).

# Abstract

During development, mechanical forces cause changes in shape, position, size and gene expression in cells. Despite the importance of mechanical forces, we still lack an efficient means to measure them in space and time in vivo and therefore to relate them with cell and tissue shape changes. Among the experimental techniques that have emerged to measure forces in epithelial tissues, force inference is particularly appealing. It is non-invasive and allows quantifying forces at cell contacts during cell shape changes and rearrangements. The force inference method consists of inferring forces based on the tissue's apical geometry, with the assumption that forces are balanced at each tri-cellular junction. Although it was compared to laser ablations in a few cases, force inference has never been systematically compared to an independent method in various tissues and model systems. In this thesis work, I first implemented two force inference methods and validated them on numerical, simulated data. Then I conducted systematic comparisons of force inference with laser ablation experiments in four epithelial tissues from two animals, the fruit fly and the quail. We show that force inference accurately predicts single-junction tension, tension patterns in stereotyped groups of cells, and tissue-scale stress patterns, in wild type and mutant conditions. We emphasise its ability to capture the distribution of forces at different scales from a single image, which gives it a critical advantage over perturbative techniques such as laser ablation. Overall, our results demonstrate that force inference is a reliable and efficient method to quantify the mechanical state of epithelia

during morphogenesis, especially at larger scales when inferred tensions and pressures are binned into a coarse-grained stress tensor. Ablation, as a direct force measurement method in tissue mechanics studies, necessitates a proper image analysis. I also improved the ablation analysis by simulating ablation with a toy model.

The mechanical description of epithelial tissues is essentially 2D, while these tissues are 3D. Suppose 2D descriptions can be relevant for shape changes that preserve the cell's apical area. In that case, it is insufficient for apical expansion or constriction, which typically occurs during epithelial invagination processes. In the second part of my thesis, I have studied the mechanics associated with 3D cell shape changes during the invagination of mesoderm in the *Drosophila* embryo. The invagination begins with a phase of apical constriction and cell thickening, followed by a phase of thinning and basal expansion, leading to the formation of folds. However, the mechanism implied in the basal expansion remains unclear. To understand the coupling between apical constriction and basal expansion, I used 3D confocal imaging and laser ablation. Imaging shows that when apical contraction occurs, the cell volume is preserved on the minute timescale so that basal expansion could be a consequence of volume conservation. In the laser ablation experiments, I have perturbed the apical actomyosin, leading to either apical expansion or contraction and triggering delayed changes of the basal area, which reveals the propagation of the deformation along the apico-basal axis.

# Resumé

Au cours du développement, les forces mécaniques provoquent des changements de forme, de position, de taille des cellules et affectent l'expression génique. Malgré l'importance des forces mécaniques, nous manquons encore de moyens efficaces pour les mesurer in vivo dans l'espace et le temps et pour les relier aux changements de forme des cellules et des tissus. Parmi les techniques expérimentales qui ont émergé pour mesurer les forces dans les tissus épithéliaux, l'inférence de force est particulièrement attrayante : elle est non invasive et capable de quantifier les forces agissant aux contacts entre cellules lors des changements de forme et les réarrangements cellulaires. La méthode d'inférence de force consiste à déduire les forces sur la base de la géométrie des cellules dans le plan apical, en faisant l'hypothèse de l'équilibre des forces agissant sur les contacts. Bien que validée dans quelques cas par des mesures d'ablation laser, cette méthode n'a jamais été comparée systématiquement à une autre méthode indépendante de mesure et sur différents tissus. Dans la première partie de cette thèse, j'ai implémenté deux méthodes d'inférence de forces, et les ai validées avec des tissus simulés numériquement. Ensuite, j'ai effectué des comparaisons systématiques de l'inférence de force avec des expériences d'ablation laser dans quatre tissus épithéliaux de deux animaux, la mouche du vinaigre et la caille. Nous montrons que l'inférence de force prédit avec précision la tension à une seule jonction, les schémas de tension dans des groupes stéréotypés de cellules, et les schémas de tension à l'échelle du tissu, dans des conditions de type sauvage et mutant. Nous soulignons sa

capacité à déterminer la distribution des forces à différentes échelles à partir d'une seule image, ce qui lui confère un avantage critique par rapport aux techniques perturbatrices telles que l'ablation laser. Dans l'ensemble, nos résultats démontrent que l'inférence de force est une méthode fiable et efficace pour quantifier l'état mécanique des épithéliums, en particulier à des échelles plus grandes lorsque les tensions et les pressions inférées sont regroupées dans un tenseur de contraintes à gros grain. L'ablation, en tant que méthode de mesure directe de la force dans les études de mécanique tissulaire, nécessite une analyse d'image appropriée. J'ai amélioré l'analyse de l'ablation en simulant l'ablation avec un modèle simplifié. La description mécanique des tissus épithéliaux est souvent 2D alors que ces tissus sont 3D. Si la description 2D est pertinente lorsque les changements de forme préservent les aires apicales, elle est insuffisante lors d'évènements de constriction ou d'extension apicale, présents lors des processus d'invagination épithéliale par exemple. Dans la seconde partie de ma thèse, j'ai étudié la mécanique associée aux changements de forme cellulaire 3D lors de l'invagination du mésoderme de l'embryon de *Drosophile*. L'invagination épithéliale commence par une constriction apicale et un allongement cellulaire, conduisant à un épaissement de l'épithélium, suivi d'un raccourcissement cellulaire et d'une expansion basale, ce qui conduit à la formation de fosses ou de plis profonds. Cependant, le mécanisme impliqué dans l'expansion basale de la cellule reste mal connu. Pour comprendre le couplage entre la constriction apicale et l'expansion apicale, j'ai utilisé l'imagerie confocale 3D et l'ablation laser. L'imagerie indique que lorsque la partie apicale de la cellule se contracte, le volume de la cellule reste constant à l'échelle de la minute suggérant que les changements basaux pourraient être une conséquence de la conservation de volume cellulaire. Dans des expériences contrôlées d'ablation laser, j'ai perturbé l'actomyosine apicale, déclenchant l'expansion ou la constriction apicale des cellules, et produisant des changements d'aire basale avec un délai, qui révèle la propagation de la déformation le long de l'axe apico-basal.

# Acknowledgment

To start, I would like to express my gratitude to Pierre-François for the opportunity to work in his lab. I am grateful to him for having the time to tutor me. I would like to thank him for his diligent advices, which often provided me with new ideas to complete my Ph.D. I would also like to express my gratitude to Raphael for assisting and motivating me in every way possible during my Ph.D. He has cultivated an appreciation for teaching and mentoring students by his example. Thank you for your professionalism and friendship.

I would like to thank the jury members of my Ph.D. thesis: Dr. Isabelle Bonnet from Institute Curie Paris, Dr. Cyperien Gay from MSC Paris, Dr. Magali Suzanne from CBI Toulouse, and Dr. Olivier Théodoly from LAI Marseille for agreeing to judge my Ph.D. thesis.

My sincere thanks go to Olivier, who initiated the force inference in the team. I thank him for all the brilliant ideas he shared when I was stucked. I would also like to thank Pruthvi for teaching me the laser ablation experiments and Claire for her technical assistance with the ablation setup. I would like to thank all of our collaborators: Claudio, Mehdi, and Jerome.

I would like to thank the previous and current team members: Monika, Pierre M., Pierre R., Pritha, Ali, Eunice, Kenji, Katia, and Victoria, for providing prompts for sci-

ence or non-scientific discussion. I would like to thank Elsa for being part of the thesis comity. I would also like to thank Benoit for the help with TissueAnalyser. I would like to thank as well Jules, Anais, Alain, Steve from the Lecuit team for their flies tips. I would like to express my gratitude to Carla and Melanie from the LABEX administration for their assistance.

I cannot begin to express my gratitude to my family, my parents; thank you for everything. Your unconditional love and support have meant the world to me; I hope that I have made you proud. And to my girl, Anne, you are my inspiration to achieve greatness. You are the most incredible present I have ever had. And to Yanjia, thank you for always being there. Your love has sustained me through times when I felt like giving up.



This work is a dedication to my little princess.

I love you to the moon and back to infinity

# Contents

<b>Abstract</b>	<b>ii</b>
<b>Resumé</b>	<b>iv</b>
<b>Acknowledgment</b>	<b>vi</b>
<b>Contents</b>	<b>ix</b>
<b>List of Figures</b>	<b>xiii</b>
<b>1 Introduction</b>	<b>1</b>
1.1 Morphogenesis . . . . .	1
1.2 Epithelial Tissues . . . . .	2
1.2.1 Apical basal and lateral surfaces . . . . .	3
1.2.2 Adhesion between cells . . . . .	4
1.2.3 Description of 2D epithelial sections . . . . .	5
1.3 Model system . . . . .	5
1.3.1 <i>Drosophila</i> . . . . .	6
1.3.2 Quail . . . . .	8
1.4 Tissue mechanics . . . . .	8
1.4.1 Morphogenetic movements in epithelia . . . . .	9
1.4.2 Invaginations and folds . . . . .	9

---

1.4.3	Changes in dimensions of an epithelial sheet . . . . .	10
1.4.4	Cellular activities contribute to morphogenesis . . . . .	11
1.5	The mechanical ingredients in the cells . . . . .	14
1.5.1	Actin and myosin (tension & contraction) . . . . .	14
1.5.2	Adhesion molecules (adhesion) . . . . .	17
1.5.3	Cell surface tension as a result of cortical tension and cell-cell adhesion	20
1.5.4	Intercellular pressure . . . . .	21
1.5.5	The interplay between mechanics and biochemistry (proteins) . . .	22
1.6	Mechanical approaches . . . . .	22
1.6.1	Mechanical measurements . . . . .	23
1.7	Physical models and simulations . . . . .	27
<b>2</b>	<b>Method</b>	<b>29</b>
2.1	Sample preparation . . . . .	29
2.2	The strain used for experiments . . . . .	30
2.3	Laser ablation . . . . .	31
2.3.1	The setup of laser ablation . . . . .	31
2.3.2	Laser and material interaction . . . . .	32
2.3.3	Laser ablation protocol . . . . .	33
2.4	Image analysis . . . . .	34
2.4.1	Static analysis . . . . .	34
2.4.2	Dynamic analysis . . . . .	35
2.5	Simulation of ablation . . . . .	39
<b>3</b>	<b>Force Inference</b>	<b>41</b>
3.1	General and historical information about inference . . . . .	41
3.2	Laplace force inference . . . . .	44
3.3	Bayesian force inference . . . . .	46
3.4	Stress determination . . . . .	48

---

3.5	Implementations . . . . .	49
3.5.1	Laplace force inference . . . . .	49
3.5.2	Bayesian force inference . . . . .	49
3.6	Validation on synthetic tissues . . . . .	50
<b>4</b>	<b>Force inference cross-validation with various tissues</b>	<b>54</b>
4.1	Single junction tensions in the <i>Drosophila</i> notum . . . . .	55
4.2	Tension patterns in wild type and mutant <i>Drosophila</i> ommatidia . . . . .	57
4.3	Stress pattern in the avian embryo . . . . .	60
4.4	Stress pattern in the wild type and mutant <i>Drosophila</i> germband . . . . .	63
4.5	Comments on Laplace force inference . . . . .	66
4.6	Stress tensor based on cell shapes only . . . . .	68
4.7	Limitation and discussion . . . . .	69
<b>5</b>	<b>Apico-basal coupling</b>	<b>72</b>
5.1	Cell volume conserved by basal changes . . . . .	73
5.2	Ablation induce apical and basal variations . . . . .	74
5.3	Quantifying cell area variation with force inference . . . . .	77
5.4	Propagation of the contraction . . . . .	79
5.5	Discussion . . . . .	80
<b>6</b>	<b>Perspective and discussion</b>	<b>81</b>
6.1	Force inference for the future? . . . . .	81
6.1.1	Which method to choose . . . . .	81
6.1.2	Dynamic force inference . . . . .	83
6.1.3	The correlation with junctional molecules intensity . . . . .	86
6.1.4	3D force inference . . . . .	86
6.2	Apical basal coupling . . . . .	88
6.2.1	The height changes . . . . .	88

---

6.2.2	Molecular contribution to the coupling . . . . .	89
6.2.3	To measure the propagation . . . . .	89
<b>A</b>	<b>Appendix figures</b>	<b>91</b>
<b>B</b>	<b>Article</b>	<b>102</b>
	<b>Bibliography</b>	<b>115</b>

# List of Figures

1.1	The different types of Epithelium. . . . .	3
1.2	Junctional complexes in epithelial tissue . . . . .	5
1.3	2D Description of epithelial . . . . .	6
1.4	Intercellular junctions in vertebrates and <i>Drosophila</i> . . . . .	7
1.5	<i>Drosophila</i> ventral furrow . . . . .	10
1.6	Apical constriction of <i>Drosophila</i> mesoderm . . . . .	12
1.7	T1 transition in the germband. . . . .	13
1.8	Schematic model for myosin-dependent actin sliding cycle. . . . .	16
1.9	E-cadherin at the adherens junction. . . . .	18
1.10	Patterns of <i>Drosophila</i> eye . . . . .	18
1.11	Adhesion and cell packing patterns. . . . .	19
1.12	Interplay between cortical tension and adhesion . . . . .	21
1.13	Micropipette aspiration . . . . .	24
1.14	Liquie droplet in a tissue. . . . .	25
1.15	FRET . . . . .	25
1.16	Diagram of optical tweezers . . . . .	26
1.17	Laser ablation on single junction and tissue. . . . .	27
2.1	The setup of laser ablation . . . . .	32
2.2	An example of segmentation . . . . .	35
2.3	Kymograph of laser ablation experiment . . . . .	36

---

2.4	The intensity profile of the kymograph . . . . .	36
2.5	Pipeline of the 3D analysis. . . . .	39
2.6	Simulation of laser ablation . . . . .	40
3.1	Inferring forces with angles. . . . .	42
3.2	Laplace law governs the curved junction. . . . .	44
3.3	Laplace topological information . . . . .	45
3.4	Schematic of force balance on one vertex . . . . .	46
3.5	The indefiniteness due to topology . . . . .	47
3.6	Validation of Bayesian force inference on synthetic data . . . . .	52
3.7	Validation of Laplace force inference on synthetic data . . . . .	53
4.1	Force inference at the single junction scale in the <i>Drosophila notum</i> . . . . .	56
4.2	Force inference in the <i>Drosophila</i> retina. . . . .	58
4.3	Tissue-scale force inference in the quail embryo. . . . .	61
4.4	Tissue scale force inference in the <i>Drosophila</i> germband. . . . .	64
4.5	Errors with Laplace inference . . . . .	67
5.1	Time-lapse of a pulsed cell. . . . .	73
5.2	The plot of apical area variation ratio versus basal area variation ratio. . . . .	75
5.3	Ablation induces apical variations. . . . .	75
5.4	Apical and basal variations of ablated cells. . . . .	76
5.5	Apical and basal variations for non ablated cells. . . . .	77
5.6	Area variations compare to shape and tension of cell. . . . .	78
5.7	The apical change propagates to basal side . . . . .	79
6.1	The flowchart for force inference decision . . . . .	82
6.2	Schematic explaining how VFM works . . . . .	85
6.3	Patch of cells in 3D . . . . .	87
6.4	Junction extraction in 3D . . . . .	88

---

6.5	Track the ablation in 3D . . . . .	90
A.1	Recoil speed estimation depends on fitting time . . . . .	92
A.2	Impact of point ablation on surrounding tissue geometry . . . . .	93
A.3	Ablations in the ommatidia . . . . .	94
A.4	Supplementary results on ommatidia . . . . .	95
A.5	Stress anisotropy along the AP axis Position along AP axis . . . . .	96
A.6	Stress estimates from cell shapes only in the WT germband . . . . .	97
A.7	Stress estimates from cell shapes only in the quail embryo . . . . .	98
A.8	Ablation to isolate a cell . . . . .	99
A.9	Area changes vs mean tension and circularity . . . . .	100
A.10	Estimation of the propagation . . . . .	101



# Chapter 1

## Introduction

### 1.1 Morphogenesis

Morphogenesis is the process by which individual cells within a developing embryo move and organize themselves to form a complex organism. The majority of animals start their lives with the process of gastrulation. During gastrulation, the single-layered cell produces three different germ layers named endoderm, ectoderm, and mesoderm. The established layers will later build up different organs and tissues. A morphogen is a class of molecules that play an indispensable role in the process of gastrulation. The morphogen diffuses through a concentration gradient, carrying signals for undifferentiated cells. The morphogen concentration is a positional information that instructs undifferentiated cells (Tabata & Takei, 2004), hence driving the differentiation of unspecialized stem cells into different cell types, ultimately forming the tissues. Tissue formation requires the sorting of cells. Cell sorting consists of cells moving to sort into clusters that optimize the interaction between the same type of cells (Townes & Holtfreter, 1955). The formed tissue undergoes morphogenetic movements: elongation, invagination, and folding to form more complex structures. This tissue organization occurs as a result of a series of morphogenetic events involving cell rearrangements, shape changes, differential growth, and apoptosis. Morphogenetic events can take place at the single-cell level or coordinately in

a group of cells to organize tissues. The relationship between cell-level events and tissue organization appears to be critical for understanding morphogenesis. As rearrangements, movements and shape changes at the tissue level are driven by mechanical forces at the cell level, it is critical to understand how such forces affect tissue organization.

## 1.2 Epithelial Tissues

As one of the four main types of tissues found in the human body and many others, epithelial tissues are important for a variety of processes including organ formation and body shaping. These processes play a central role in animal development.

The essential function of epithelial tissues is to serve as a chemical and mechanical barrier. Epithelia protect the internal body from bacteria and other harmful substances, offering sensory functions in the skin, nose, eyes, and ears. Epithelia are also important secretory tissues, which secrete hormones, sweat, digestive juices, and mucus. Epithelia also have functions in absorption: they absorb nutrients in the gut and exchange gases in the lungs.

Epithelial cells are classified into three different categories according to their shape and multicellular organization (Fig.1.1). The first type is the simplest of all: the simple squamous epithelium, which is highly flat, and is also known as the basement epithelium. Its flat nature clearly states its function and location. It is primarily used to transport or precisely fuse substances across membranes and perform filtration. One finds them in the thinnest surfaces in our bodies, such as the lining of blood capillaries, the lining of alveoli, and the inner lining of our mouth. In the skin, the same squamous epithelium appears in layers; several layers, one on top of the other, form the outermost layers of the skin, which is called stratified squamous epithelium (Alomari, 2004). It protects the skin's upper surface from wear and tear. Cuboidal epithelial cells have a cube-like shape. Cuboidal epithelium are usually present in secretive tissues such as exocrine glands or absorptive tissue such as the pancreas, the lining of kidney tubules, and glandular ducts.

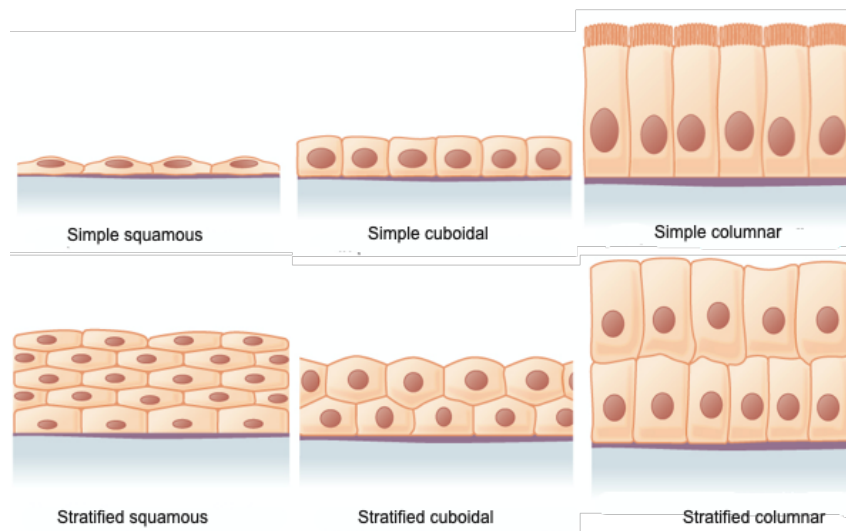


**Figure 1.1:** Sketch of simple squamous simple columnar and pseudostratified epithelia (yale.edu)

Simple cuboidal epithelium is generally differentiated to form gland secretory and ductal parts. The stratified cuboidal epithelium covers sweat gland ducts, mammary glands, and salivary glands (Kurn & Daly, 2020). The last type is a tall pillar-like structure, known as the columnar epithelium due to its column-like appearance. The tall columnar cells of these helps absorption or secretion, for example in the intestine. Tiny hairlike projections called cilia on the surface of these cells perform rhythmic movements that can aid in the movement of non-motile substances (Kurn & Daly, 2020).

### 1.2.1 Apical basal and lateral surfaces

Epithelial cells are polarized cells, with distinct plasma membrane domains designated as apical, lateral, and basal. The apical or free surface is exposed to an internal body space or the external environment. The basal surface is attached to the basement membrane. Epithelial cells form epithelial sheets by connecting to each other via the lateral membrane. Each plasma membrane domain contains a specific protein composition, conferring specific propoerties and allowing molecules to be transported in a directional manner across the epithelial sheet (Lodish et al., 2000).

Apical membranes are involved in a variety of processes, including absorption and secretion, immunological surveillance, sensory transduction, and barrier formation. The lipids of the apical plasma membrane limit water and solute flux. The channels and receptors regulate active and passive transport and sense the presence of growth factors, cytokines, and mechanical stimuli (for example stretch and shear stress) (EH Stoops, 2014).

All epithelial cells are attached on their basal surface to a basement membrane. The basement membrane is a form of extracellular matrix (ECM). This matrix consists of secreted extracellular macromolecules that form mechanical support for the epithelial cells. It helps holding cells and tissues together. Integrins in the plasma membrane help epithelial cells bind to their basement membrane components (Fig.1.2). The basement membrane also supports the growth and survival of the epithelial cells as it controls the access of epithelia to nutrients, ions, proteins, and oxygen (Michel et al., 2010).

### 1.2.2 Adhesion between cells

To form a tissue, epithelial cells are joined together by specialized protein complexes known as junctional complexes located on the lateral membrane. Looking at a cross-section (apical-basal) of an epithelial tissue (Fig.1.2), tight junctions are found at the very apical end, followed by adherens junctions, desmosomes, and gap junctions, and finally cell-ECM anchoring junctions (Albert, 2002). Each junction complex serves a specific purpose.

Tight junctions are known as zipper-like structures because they are formed from the interactions of claudins and occludins (Tsukita & Furuse, 1999). The general function of tight junctions is to prevent leakage of transported solutes and water and to seal the paracellular pathway. Both adherens junctions and desmosomes act as the anchors between cells. Adherens junctions are specialized structures that connect to the actin cytoskeleton network, allowing mechanical coupling between neighboring cells. Desmosomes are stronger connections between adjacent cells' intermediate filaments that spread

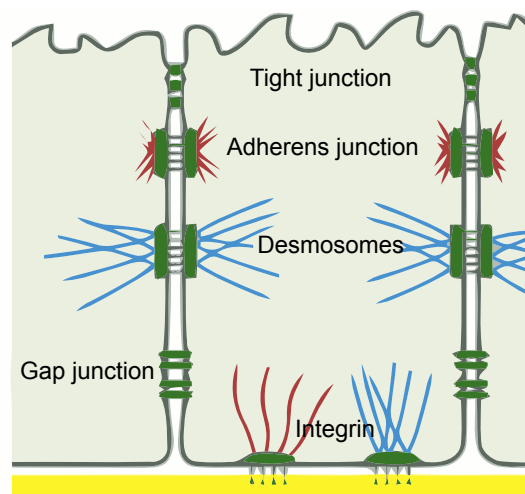


**Figure 1.2:** Schematic of epithelial junctions structure (adapted from X. Tu 2017)

from the nucleus to the cell membrane and form a complex network in the cytoplasm. Gap junctions are clumps of channels that form aqueous communication tunnels between cells. They allow water-soluble molecules to move from one cell to another through direct contact, also known as intercellular communication.

### 1.2.3 Description of 2D epithelial sections

Looking at a planar cross-section of epithelial tissue, for example, the apical surface (Fig.1.3), the epithelial cells are arranged in a polygonal pattern, each cell boundary having a polygon-like shape. The junction is seen as a segment (red line) that connects two adjacent cells. The vertex (green point) is the point shared by three connected junctions (3-way vertices). It should be noted that the vertices can also be the meeting point of four junctions (4-way vertices).

## 1.3 Model system

A model organism is a species that is used to study specific biological processes, with the hope of gaining insight into similar processes in other organisms. In the last decades, some of the model organisms, such as the mouse, the fruit fly, in particular the *Drosophila*

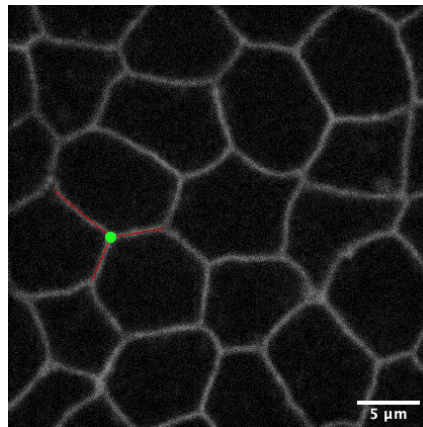


**Figure 1.3:** 2D Description of epithelial of *Drosophila* embryo

*melanogaster*, and the nematode *Caenorhabditis elegans*, became more widely used than others. This section will introduce two model systems: *Drosophila* and *quail*, which were used in my thesis.

### 1.3.1 *Drosophila*

The *Drosophila* is an outstanding model organism for developmental biology. The small size and short life cycle (10-12 days from egg to adult fly) provide an interesting asset for research. Additionally, *Drosophila* has a relatively small genome size (220.6 Mbp), completely sequenced in 2000 (Adams et al., 2000). Genetic analysis has emerged as an important approach biologists use to study developmental mechanisms. Genetic mosaicism can be easily generated in the *Drosophila* (Blair, 2003). Genetic mosaicism techniques are those that induce genetic changes in a subset of cells or tissues in an individual organism (Blair, 2003). Then finally, transgenic lines can be easily created by expressing foreign genes with the *Drosophila*; for example, the green fluorescent protein (GFP) gene can be fused with a target gene as a vital marker/reporter to visualize dynamic changes in the expression of a target gene (Yeh et al., 1995).

In the initial stages of *Drosophila* development, a single diploid nucleus undergoes several DNA replications cycles in mitosis to form daughter nuclei. This structure, where multiple nuclei share a common cytoplasm, is called a syncytium. By the end of the

syncytium stage, there are about 6000 nuclei located around the periphery of the embryo. The following stage is cellularisation, where all of the nuclei become enveloped by a plasma membrane. Immediately after cellularisation, gastrulation starts. During the *Drosophila* embryonic stage, many morphogenetic events such as the mesoderm invagination or germband extension are served as a model system in numerous studies. Nevertheless even at the larva or adult stage, some tissues continue to be followed by different research because of their unique shape and structure, for example, the retina. This tissue will be discussed in greater detail along with few others in the following sections.

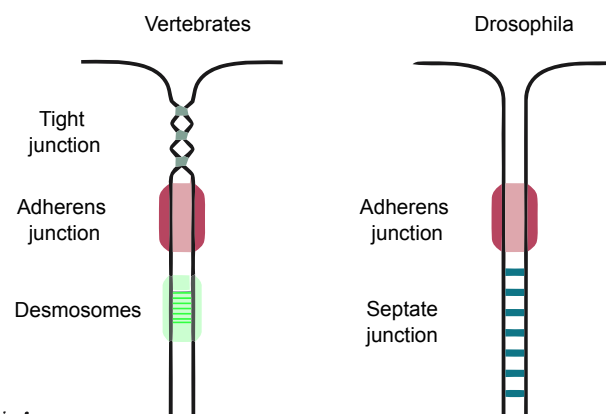


**Figure 1.4:** Intercellular junctions in vertebrates and *Drosophila*, adapted from (Tepass 2003).

Unlike the epithelial tissue structure mentioned in the previous section, the *Drosophila* epithelial tissue has a septate junction in place of desmosomes (Fig.1.4). They are believed to provide structural strength as well as a barrier to solute diffusion through the intercellular space. They are thought to be similar to (vertebrate) tight junctions; however, tight and septate junctions vary in many respects. Components of conserved signaling pathways that localize to adherens junctions are known *Drosophila* homologs of tight junction components (Matter & Balda 2003).

### 1.3.2 Quail

Japanese quails are medium-sized birds that belong to the Phasianidae family. They are migratory game birds. Japanese quail have been domesticated for a few decades. They are the most common quail species used for egg production. The Japanese quails have also been used widely as a model species in avian development and other researches (Morris et al., 2019).

The early quail embryo develops as a flat, highly proliferative epithelial disk that can be easily live-imaged for a long period of time. Quail gastrulation involves large-scale cellular movements taking place within the single-cell embryo. The endodermal and mesodermal derivatives internalize through the primitive streak, a temporary structure at the midline of the early embryo. This primitive streak forms from an initially crescent-shaped region at the margin between the embryo proper and extra-embryonic tissue, which converges towards and extends along the midline. At the same time, myosin-driven oriented cell intercalation is known to underlie convergence-extension of the prospective primitive streak (Rozbicki, E. et al., 2015). Concomitant with the formation of the primitive streak, a large-scale rotational tissue-wide flow is observed.

## 1.4 Tissue mechanics

Animal morphogenesis relies on a variety of morphogenetic deformations, such as invagination and elongation. These deformations are often induced by cellular events such as cell shape changes (Condic et al., 1991), cell rearrangements (Lecuit & Lenne, 2007), patterned cell divisions (Baena-López et al., 2005), and patterned apoptosis (Suzanne & Steller, 2013). This chapter will begin by discussing the various types of morphogenetic movements. The cellular events that result in those movements will then be explained. Next, the molecular mechanisms underlying these events will be introduced. To better understand these morphogenetic movements, the tissues in which these movements take place will be detailed, including the *Drosophila* retina, germband, and mesoderm. These



are the tissues that were used in this thesis.

### 1.4.1 Morphogenetic movements in epithelia

A large number of complex structures emerge from the deformation of epithelial sheets. These movements include invagination or folding, as well as in-plane deformation, such as spreading or elongation. These tissue deformations that occur during morphogenesis are accomplished by a few basic processes that, when combined in various ways, produce an enormous diversity of complex structures.

### 1.4.2 Invaginations and folds

Epithelial invagination is a fundamental morphogenetic process that generates many parts of a developing organism (Fig.1.5). The invagination drives processes ranging from the body axis formation (Davidson et al., 1995) to primordia formation (Hilfer et al., 1989). The first and most important invagination process in most animals is the one setting up gastrulation. The primitive streak is an invagination that determines the site of gastrulation and initiates germ layer formation. Invagination that occurs along a line is a furrow (Fig.1.5). In *Drosophila*, the ventral furrow marks the start of gastrulation. Ventral cells make an indentation in the ventral part of the early epithelium (ventral furrow), which then invaginates towards the embryo's interior to begin the development of mesodermal structures. The mesoderm progenitor cells located at the ventral-most side of the embryo in a narrow band of cells elongate along the anterior-posterior embryonic axis. Notably, the formation of tissue furrows is not only directed inwards but can also be directed outwards (named evagination).

It is important to note that during morphogenesis, another process, folding, plays a significant role in the formation of various organs. Unlike invagination and evagination, which are preceded by an increase in cell height, folds can appear in epithelia without any associated changes in cell height. Folds have a tendency to form uniform convolutions,

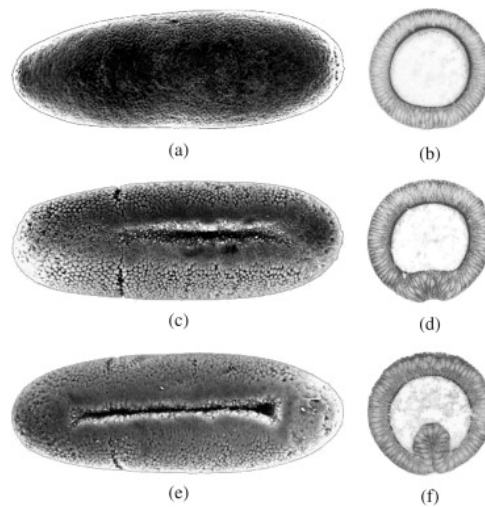


**Figure 1.5: The ventral furrow formation** Images on the left show ventral views (Grumbling et al., 2006) and those on the right a 2D cross-section (Muñoz et al., 2007).

such as brain convolutions.

### 1.4.3 Changes in dimensions of an epithelial sheet

A uniform surface area change of an epithelial layer leads to a change in sheet size without any shape change. An epithelial surface change is also directly caused by a change in the planar surface of component cells. In vertebrates or zebrafish, at the onset of gastrulation, the blastoderm starts spreading over the spherical yolk. This spreading is named epiboly which is one of the predominant gastrulation movements shared by many vertebrates. Epiboly leads to tissue expansion, often accompanied by flattening. The spreading of an epithelial sheet is more common than contraction during development.

A non-uniform change of the surface area will cause a global tissue shape change, such as an elongation. The elongation of a tissue is a common morphogenesis process that leads to changes in the length/width ratio of an epithelium. *Drosophila* germband extension is a well-studied example of body axis elongation. The germband of the *Drosophila* embryo, a stripe of ectodermal cells on the ventrolateral side of the embryo (Fig1.7), extends into the embryo's segmented trunk, almost doubling in length along the anterior-posterior axis

while remaining relatively narrow along the dorsal-ventral axis (Fig.1.7).

These examples of epithelial morphogenesis deformation illustrate several important points. Tissue morphogenesis involves changes not only in the plane but also in space, referring to the overall shape of the cells. The overall deformation appears to be the result of a single cell's shape changes or movement. This implies that it is critical to investigate mechanics at the level of the individual cells to understand the morphogenetic movements.

#### 1.4.4 Cellular activities contribute to morphogenesis

During development, cells undergo a number of biomolecular processes that modify their components. The changes in cellular components cause changes in the physical properties, resulting in changes in cell shape. A cell population can coordinate its shape changes, by changing individual cell shapes or changing cell neighbors. Additionally epithelia cells, like any other cells in living organisms, undergo cell division and cell death. This may cause cell to tissue-level deformation.

##### 1.4.4.1 Cell Shape Changes

Coordinated changes in cell shapes across a tissue will result in tissue deformation. In epithelia, only a few types of cell shape changes are observed. For example, uniform cell flattening or columnarization causes the sheet to expand or contract in an isotropic manner. Cells can also expand (or contract) along the planar axis; this type of cell shape change affects the apical or basal surface of the cell and causes the sheet to bend into three-dimensional structures. Apical constrictions, for example, are linked to invagination (Polyakov et al., 2014), while basal constrictions are linked to evagination (Lomakin et al., 2015).

Single-cell shape changes, independent of their neighbors, lead to a variety of morphogenetic processes, such as the movement of single primordial germ cells toward the gonad (Blaser et al., 2006). However, in most morphogenetic events, cell shape changes are coordinated amongst hundreds of neighboring cells and drive extension, invagination, and

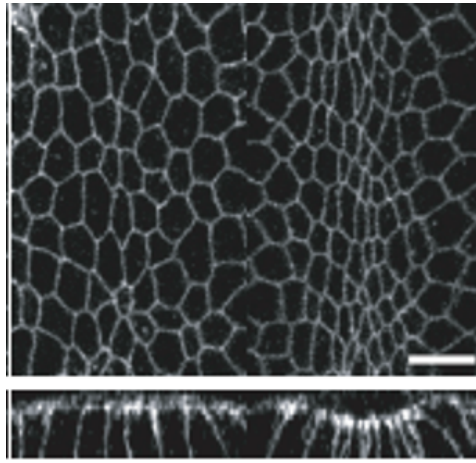


**Figure 1.6:** Images showing the early and late stages of mesoderm invagination. below, the midline in cross section. adapted from (Martin et al., 2009)

other movements of tissues. Early research has suggested that tissue invagination is mediated by a sequence of coordinated cell shape changes (Leptin & Grunewald, 1990). The ventral furrow formation in *Drosophila* is driven by the coordinated apical constriction of mesoderm cells (Fig.1.6).

#### 1.4.4.2 Cell rearrangement

Changes in cell position result from either cell migration or cellular rearrangements, such as cell intercalation or convergent extension. The convergent extension is a common process in gastrulation and entails the narrowing of the forming embryonic axis along its mediolateral axis and concomitant elongation along its anterior-posterior axis (Keller et al., 2000). The convergent extension has been linked to cells experiencing mediolateral cell intercalation in amphibians. In theory, mediolateral cell intercalations may trigger convergent extension(Keller et al., 2000).

To enable cells to intercalate between one another, the adherens junctions that maintain the epithelial tissue's integrity must be dynamically remodeled. This process of cell neighbor exchanges is known as T1 transition. T1 transition is a three-step process that we define below for the *Drosophila* germband (Fig.1.7). In the type 1 configuration , two cells make direct contact along the anterior-posterior axis, whereas two dorsal-ventral

cells do not. The cell boundary between the two anterior-posterior neighbors is then selectively shrunk, resulting in an obligatory intermediate type 2 junction in which the four cells share a vertex. When the type 2 junction is resolved, a new type 3 junction forms perpendicular to the original type 1 configuration. The two dorsal-ventral cells became neighbors during this process (Bertet et al., 2004). When multiple clusters of cells intercalate in the dorsal-ventral axis via junctional neighbor exchanges, the result is an anterior-posterior germband extension (Bertet et al., 2004; Zallen & Wieschaus, 2004). Cell intercalation has been observed in a variety of organisms, including the dorsal extension in *C. elegans* (Walck-Shannon & Hardin, 2014), the extension of the neuroepithelium in chick and mouse (Nishimura et al., 2012), and the extension of the mesoderm in Zebrafish (Yin et al., 2008).

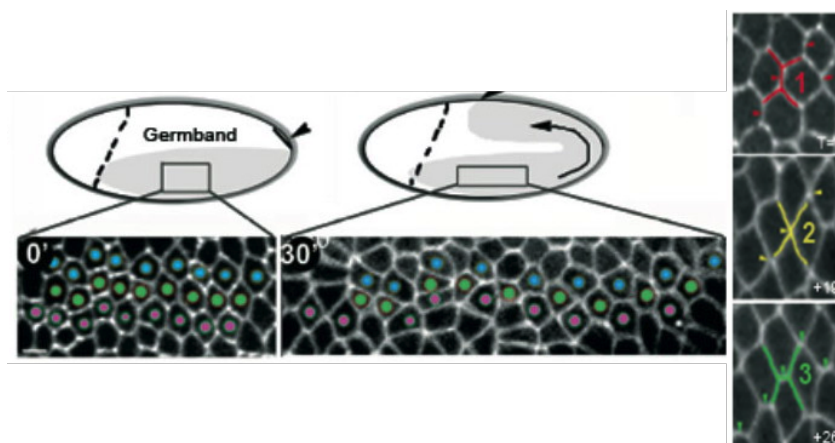


**Figure 1.7: T1 transition in the germband.** Left: Schematic of the germband extension. Two images show the rectangle portion of tissue during the extension (with color-labeled cells). Right: Cell contacts in the type 1 configuration (red line) progress towards the type 2 (yellow line) and to the type 3 configuration (green line), adapted from (Bertet et al., 2004)

#### 1.4.4.3 Cell division and apoptosis

Cell division is an important mechanism for morphogenesis. Apart from its purpose of increasing cell numbers, cell division plays other roles in tissue morphogenesis. The cell division was found to affect cell rearrangements during limb ectoderm development (Lau

et al., 2015). In chick, the epithelial rearrangements were found to be mediated by cell divisions and underlie the spatial patterning of gastrulation movements (Firmino et al., 2016). These observations demonstrate that cell division appears to be tied to the various cellular rearrangements in different epithelia and emphasizes the importance of cellular division for morphogenesis.

Apoptosis is one kind of programmed cell death that leads to characteristic cell changes and death. These changes include cell shrinkage, chromatin condensation, DNA fragmentation (Suzanne & Steller, 2013). Programmed cell death is a critical mechanism that occurs throughout growth to eliminate dead cells. In a number of morphogenetic events, apoptosis plays a crucial role. Apoptosis can shape organs by the elimination of cells without tissue remodeling. Apoptotic cells normally induce the development in their neighbors of a ring of actomyosin networks, leading to their extrusion (Suzanne & Steller, 2013). During *Drosophila* dorsal closure, apoptosis plays a central role in modulating the tensile force of the closing tissue (Hayes & Solon, 2017).

## 1.5 The mechanical ingredients in the cells

Tissue morphogenesis requires precise control over the shape of individual cells. Mechanical properties, which describe cell geometry based on intracellular and intercellular forces, determine cell shape (Lecuit & Lenne, 2007). Mechanical properties at the cell surface are determined by the interaction of two factors: cortical tension and intercellular adhesion (Lecuit & Lenne, 2007). These mechanical forces are generated by a group of specific molecules.

### 1.5.1 Actin and myosin (tension & contraction)

Continuous molecular interactions within cells convert chemical energy into mechanical energy, resulting in physical forces that form tissue and organisms. One of the most important forces is the contractile force. Underneath the inner leaflet of the cell mem-

brane, there is a specialized layer of cytoplasmic proteins, actin filaments, and Myosin-II (Myo-II) molecular motors that form a network of crosslinked filaments responsible for the contractile force generation (Vale & Milligan, 2000). The actin-myosin (actomyosin) network, also called the cell cortex, is attached to the cell membrane via membrane-anchoring proteins, and it plays a central role in the control of cells shape (Fehon et al., 2010).

Actin proteins are the monomeric subunits that form the most important cytoskeletal microfilaments. Actin exists as a free monomer known as G-actin (globular) or as part of a linear polymer microfilament known as F-actin (filamentous actin). The filament is asymmetric, having distinguishable ends: a plus end (the growing end) and a minus end (the nucleation end) (Pollard et al., 2000). At the plus end, the free monomer polymerizes to the filament, while at the minus end, the filament depolymerizes into actin monomers. Treadmilling is the term used to describe this process. The treadmilling causes a part of the filament to appear to "move."

Myosins are composed of a long tail and two globular heads. The head is one of the functional domains, which includes actin- and ATP-binding sites and is responsible for force generation. The binding sites on the tail domain specify the precise behaviors of a particular myosin. Myo-II is one of the most common types of myosin. Myo-II binds into the filaments as a motor protein. Actomyosin is contractile as myosin is able to pull on actin filaments. This property gives rise to contractile fibers that form the basis of force generation at the sub-cellular level. The actomyosin interaction can be described in different steps (Juanes-García et al., 2018):

1. The myosin head lacks a bound ATP, and it is attached to the actin filament.
2. When ATP binds to the myosin head domain, its affinity for actin reduces, resulting in the release of the myosin head. As ATP attaches to myosin, it twists the head in a new location. Following that, ATP is dephosphorylated and bound to myosin. ATP is first hydrolyzed, leaving myosin with phosphate and ADP (Fig.1.8).
3. The myosin head makes just a weak contact with the actin filament, and myosin

undergoes a minor conformational change that facilitates phosphate release.

4. The release of phosphate strengthens the interaction between myosin and actin, thus initiating the 'power stroke.' The power stroke is the primary mechanism by which myosin motor proteins generate force. As the myosin protein reverts to its original conformation, forces are generated on the actin filament (Fig.1.8).
5. Myosin reverts to its initial conformation, releasing ADP, but the myosin head stays closely attached to the filament in a new location, allowing the filaments to slide.

Myo-II individual motors bundle together into multi-headed mini thick filament that crosslink actin filaments and contract the filamentous network.

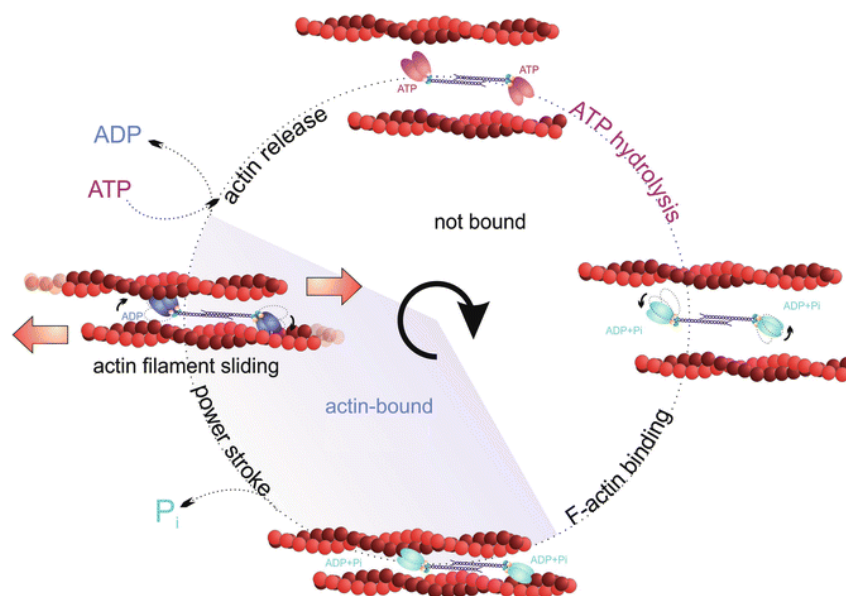


**Figure 1.8:** Schematic model for myosin-dependent actin sliding cycle. (Juanes-García et al., 2018)

### Pulsatile actomyosin trigger apical constriction

As explained in the previous section, apical constriction facilitates epithelial sheet bending and invagination during morphogenesis. However, the molecular mechanism underlying the process has not been mentioned. In fact, the apical constriction of invaginating mesodermal cells is triggered by the formation of Myo-II spots and fibers at their apical cortex (Martin et al., 2010). These apical Myo-II structures are dynamic, repeatedly



increase in intensity, and move toward the center of the cell apex, resulting in pulsatile actomyosin flows. Pulsatile flows translate into periodic apical constrictions of mesodermal cells due to the inward movement of the apical cell-cell junctions to which the actomyosin network is coupled (Martin et al., 2009; Roh-Johnson et al., 2012).

### Actomyosin control cell intercalation

Mediolateral intercalation of cells is possibly the primary force-generating mechanism underlying convergent extension (Walck-Shannon & Hardin, 2014). Myo-II is required for the formation of a cortical actin network in mesoderm cells undergoing mediolateral cell intercalation during *Xenopus* gastrulation. (Rolo A 2009). Interestingly, this cortical actin network is polarised along the mediolateral axis and undergoes pulsed contractions oriented parallel to this axis. When Myo-II activity is impaired, the cortical actin network is disrupted, cells fail to exhibit normal protrusive activity, and convergent extension movements are reduced. This suggests that oriented actomyosin-mediated contractions of the cortical actin network drive mediolateral cell intercalation.

These two examples of actomyosin-induced tissue deformations demonstrate that actomyosin contraction induces coordinated cell-level changes hence contributes to tissue-level changes. Besides that, as mentioned previously, the actomyosin ring formed in apoptotic cells is necessary for cell extrusion. Actomyosin networks can shape the organization of contractile forces, but the overall tissue architecture and other structural proteins can also influence the organization.

## 1.5.2 Adhesion molecules (adhesion)

At the heart of adherens junctions are calcium-dependent transmembrane glycoprotein, cadherins; Cadherins mediate intercellular adhesion. The main epithelial cadherin is E-cadherin. E-cadherins bind epithelial cells to their neighbors through homophilic interactions via the extracellular domain (Boller et al., 1985). In the cytoplasmic domain, the E-cadherin binds directly to actin filament through the *beta*- and p120-catenins complex (Fig.1.9). In the cadherin family, there are other cadherins, such as N-cadherin. The

N-cadherin has a similar structure as the E-cadherin.

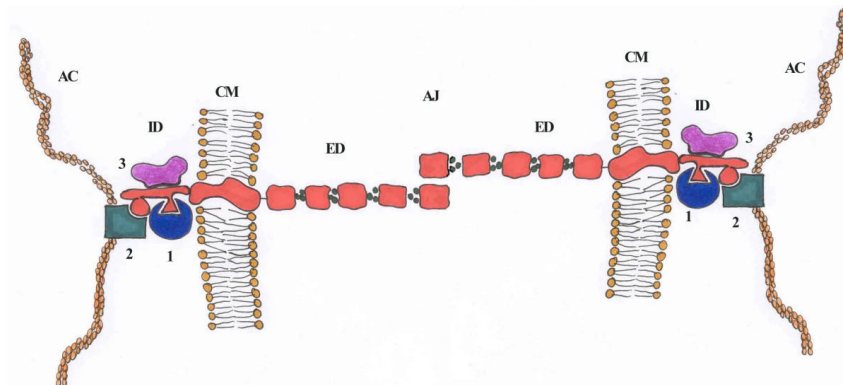


**Figure 1.9:** A homodimer of E-cadherin is seen on the cytoplasmic membranes of adjacent cells. CM– cytoplasmic membrane; AJ – adherens junction; ED – extracellular domain; ID – intracellular domain; AC – actin cytoskeleton; 1-beta-catenin; 2-alpha-catenin; 3-p120 catenin. (Pećina-Šlaus, 2003)

Cadherin activity is regulated in different ways, including the level of cadherin gene expression and the form of cadherin expressed, which influences the specificity of cell interaction and plays a role in the specification of the embryo and determination of the fate of the cell. Posttranscriptional mechanisms controlling cadherin adhesion also include control of cadherin expression and organization at the cell surface and changes in cadherin relationship with catenins.

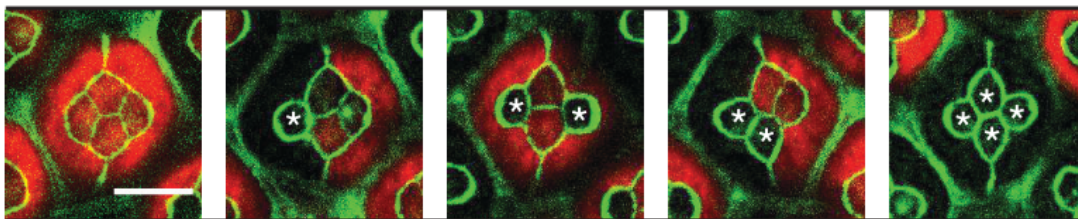


**Figure 1.10:** Patterns of *Drosophila* eye with the distributions of cadherins and Myo-II in wildtype and NcadM19 mosaic ommatidia. Each image represents one of the mosaic ommatidium (Ecad::GFP (green) and Ncad::mKate2 (red)). NcadM19 cone cells are marked by white asterisks. (E. H. Y. Chan et al., 2017)

The main function of the adherens junction is to connect epithelial cells and maintain their polarized architecture. The adhesion complex plays a huge role in shaping the cell.

*Drosophila* ommatidia are an excellent model for demonstrating how adhesion can control cell shape. Each ommatidium represents a single eye-facet, which is composed of twenty cells. Each of these cells adopts a stereotyped shape according to its position and identity. A group of four related cells (cone cells) makes adherens junction contact with each other and with two large pigment cells, which wrap around the cone-cell group (Fig.1.10 left). This structure is then embedded in a hexagonal matrix formed by the secondary pigment cells and tertiary pigment cells. The *Drosophila* retina consists of 5000 such units.

As previously reported, the striking resemblance between cone cell aggregation and that of a soap bubble indicates that cone cells aggregate themselves in a similar manner to that of soap bubbles (Fig.1.11). The cadherin drives greater contact between cells by differential adhesion mechanism. N-cadherin is expressed within cone cell junctions, and E-cadherin is expressed along all junctions. This suggests the spatially patterned distribution of N- and E- cadherin play a critical role in cone cell pattern formation of the ommatidia. The misexpression of cadherins leads to patterning defects; the differential distribution of cadherin molecules causes spatial patterning of epithelial cells (Fig.1.10). This loss of N-cadherin affects junctional Myo-II levels suggesting a contribution of Myo-II contractility in shaping cone cell patterns (E. H. Chan et al., 2017).

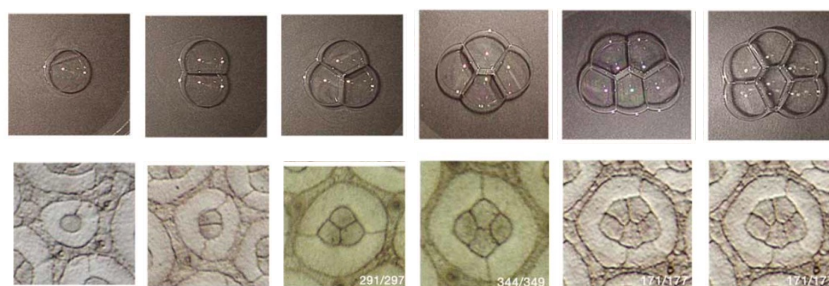


**Figure 1.11: Adhesion and cell packing patterns.** top pannel: stable soap bubble aggregates. Bottom pannel: Ommatidia of Rough eye (Roi) mutants. Inside the panels are the indicated numbers of Roi+ groups with that particular configuration compared with the total number in each group. (Hayashi & Carthew, 2004)

Cadherins play an important role in the dynamic regulation of adhesive contacts that are associated with other morphogenetic processes. During the germband extension in

the *Drosophila*, the planar polarised endocytosis of E-cadherin is required to downregulate adhesion at dorsal-ventral oriented junctions (Levayer & Lecuit, 2012). When endocytosis is blocked, intercalation fails almost entirely, leading to a drastic reduction in germband extension. Therefore, increased contractility and decreased adhesion act in concert to permit junction shrinkage. Cadherins have been shown to be involved in a variety of other processes, including tissue separation and cellular migration (Gumbiner, 2005).

### 1.5.3 Cell surface tension as a result of cortical tension and cell-cell adhesion

Surface tension is used to characterize cell aggregates or tissues that exhibit liquid-like behavior (Steinberg, 1996). Surface tension in liquids is directly related to the attraction between the constituent elements. To divide an inanimate liquid body into two parts, cohesive forces between molecules must be overcome, and two new surfaces with surface-free energy density must be created (surface tension). Unlike liquids, the cell surface and interior (plasma membrane) do not form a homogeneous liquid material, so the plasma membrane tension can be higher than the liquid because of the underlying and inside proteins' activities. In addition to the plasma membrane tension, the cortical tension generated by the cortical actomyosin has been proved to be a key factor for the cell surface tension (Tinevez et al., 2009). Along with membrane tension, cortical tension leads to an effective cell surface tension (Fischer-Friedrich et al., 2014). However, the contribution of membrane tension to effective cell surface tension is often negligible (Fischer-Friedrich et al., 2014). Thus, cortical tension is the primary contributor to the cell surface tension. For the sake of simplicity, we will refer to the tension as the cell surface tension in this thesis.

Except for cortex actomyosin, the cell-cell adhesion can influence cell surface tension (E. H. Y. Chan et al., 2017; Krens et al., 2017; Maître et al., 2012). Considered as an analog to surface tension between immiscible fluids; adhesion forces are thought to

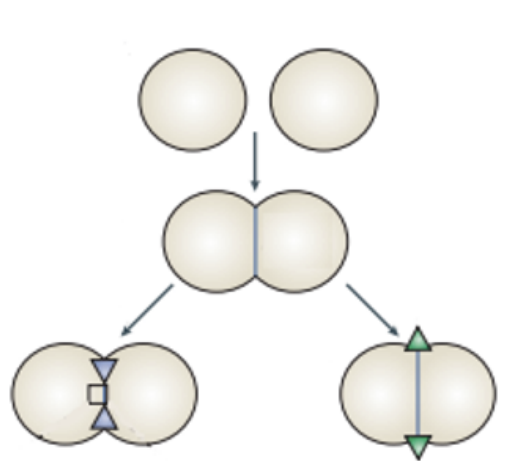


**Figure 1.12:** Intercellular surface tension results from the opposite effects of cortical tension and adhesion. The green arrow indicates that cadherin's influence tends to lengthen the contact, whereas the blue arrow indicates that actomyosin's effect tends to shorten the contact. (Lecuit & Lenne, 2007)

act parallel to the cell membrane and seek to increase the contact area of two adhering cells (Lecuit & Lenne, 2007). The actomyosin generated tensile force decreases the contact area (Fig.1.12). Similarly, in epithelia with actomyosin bundles at adherens junctions, the length of cell boundaries is reduced by a high degree of cell-cell adhesion and increased by high bundle contractility (Farhadifar et al., 2007).

#### 1.5.4 Intercellular pressure

The actomyosin contractility and flows of water across the plasma membrane generate intercellular pressure. Actomyosin contractility is thought to contribute to intercellular pressure by compressing or squeezing the cytoplasm against the plasma membrane and cell cortex (Petrie et al., 2014). The total pressure exerted by the cytoplasm against the plasma membrane is determined by water flux as a result of local ion concentration. (Chengappa et al., 2018). Intercellular pressure can modify cell shape and behavior (Chengappa et al., 2018). The intercellular pressure is an important regulator of cell dynamics, such as cell division and migration (Petrie et al., 2014).

### 1.5.5 The interplay between mechanics and biochemistry (proteins)

Mechanical forces generate cell and tissue movements. The spatial and temporal regulation of gene expression and protein activity regulate tissue mechanics, as well as their response to these forces. Mechanical cues have been found to have a profound impact on gene expression and protein activity, all of which are involved in cell fate determination (Ingber, 2006; Orr et al., 2006). Thus, the shape of the embryo and the organism's phenotype are the direct consequences of these biomechanical processes and are governed by the physical rules of mechanics.

Mechanical cues are sensed at the cell membrane through a large number of cellular components. The mechanical information gets transduced from the cell membrane to the cell interior and transmitted to the nucleus. For example, the integrin transmits stress from the ECM to the actin cytoskeleton (Albert, 2002). Cells can convert mechanical inputs such as stretch, stress, compression, and shear forces into chemical signals through intracellular molecular signaling cascades that result in altered transcriptional outputs (Sinha et al., 2011). In *Drosophila* ventral furrow formation or midgut invagination, elevated levels of mechanical stress can induce Twist expression and activate Myo-II (Farge, 2003; Pouille et al., 2009).

## 1.6 Mechanical approaches

Understanding morphogenesis requires elucidating the physical mechanisms that generate tissue structure. In recent years, significant technical advances, both experimental and computational, have enabled quantitative descriptions of the cellular dynamics, tissue deformations, and mechanical forces with unprecedented temporal and spatial resolution. The application of physical approaches to the biological problem of morphogenesis has revealed answers to the dynamic and basic questions concerning the formation and conser-

vation of tissue structure and function, which are essential to development. This section will review some of the most significant advances in mechanical force measurement. Second, we will discuss a few computational models that are frequently used in tissue and cell mechanical research.

### 1.6.1 Mechanical measurements

The mechanical balance of physical forces acting on the cell surface determines the shape of cells and tissues. Cellular mechanics is generally defined as a set of physical properties that can be extracted from measurements. Various techniques have been developed during the last decades to measure the mechanical properties of the tissue in VIVO or in VITRO. The techniques range from mechanical-based direct measurement to molecular sensing, light-based manipulation, and even theoretical methods. The numerous methods available for mechanical measurements have been emphasized in different reviews (Roca-Cusachs et al., 2017; Sugimura et al., 2016).

#### Contact manipulation

The most straightforward method of force measurement is to perturb the system directly. Micropipette aspiration is a frequently used method to pull on the sample. As indicated by the name, it aspirates the sample using a micropipette under the control of a micro-manipulator. The shape of the sample component inserted into the pipette entrance at equilibrium is defined by the balance of its surface tension and aspiration pressure (Tinevez et al., 2009). With the Laplace law (Eq 3.1), the sample surface tension can then be inferred from the applied aspiration pressure  $\Delta P$  and the radii of the sample inside  $R_c$  and outside  $R_p$  the pipette (Fig.2.5). This approach determines how the biomechanical properties of single cells or tissues control the form and response of cells to mechanical stimuli. There are other direct contact force probing methods, such as AFM, which can apply  $pN$  to  $nN$  forces to the sample as an indenter. This  $pN$  indenter has successfully been used to measure the surface tension of zebrafish embryos. (Krieg et al., 2008).

#### Liquid droplet

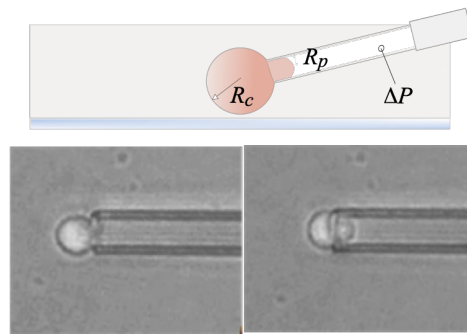


**Figure 1.13: Micropipette aspiration** Schematic of the micropipette aspiration, the images of an experiment (González-Bermúdez et al., 2019).

The liquid droplet has been used to measure tissue stress *in vivo* and *in vitro*. Although the stress carried by the droplet is usually determined by its deformation, the viscoelastic properties of the droplet, as well as its initial size and shape, must be known in order to calculate the stress. In addition, the mechanical properties of the droplet must be stable over time. As a result, synthetic probes are commonly used in this technique. This method was first demonstrated using microinjected adhesion receptor-coated oil droplets with known surface tension (Campàs et al., 2014). The anisotropy of the local stresses in the tissue can be assessed by reconstructing the droplet form using normal imaging techniques (Fig.1.14). The use of oil-droplets in combination with ferrofluids allows not only for the quantification of cell-generated forces but also for the application of controlled forces (Serwane et al., 2017). The ferrofluid oil droplet was used in zebrafish embryos to measure the endogenous mechanical stresses along the anteroposterior axis (Mongera et al., 2018).

### **FRET**

FRET is the acronym of the Förster Resonance Energy Transfer. The FRET is the phenomenon by which an excited donor transfers energy to an acceptor through a non-radiative process. So a FRET tension sensor module consists of two fluorophores: a donor and an acceptor (Miyawaki, 2011). The energy transfer efficiency is dependent on  $1/R_0$ ,



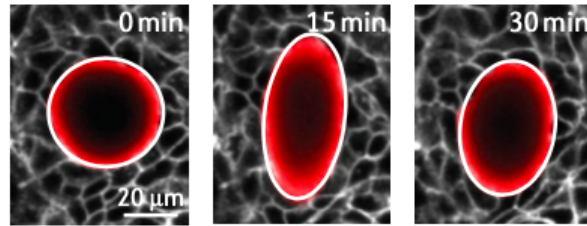


**Figure 1.14:** Application of a liquid drop as force transducers inserted into a tissue, before (0 min; left), 15 min (center), and 30 min (right) after deformation. (Mongera et al. 2018).

where  $R_0$  is the distance between the two fluorophores, so the efficiency decreases sharply with the distance. Between donor and acceptor, a spring of known stiffness is genetically inserted, such as a given polypeptide sequence (Fig.1.15). The FRET efficiency decreases when a pulling force acts on the module. The output is in the form of intensity images (Fig.1.15 ). The FRET probes forces from one to several  $pN$  (Miyawaki, 2011).

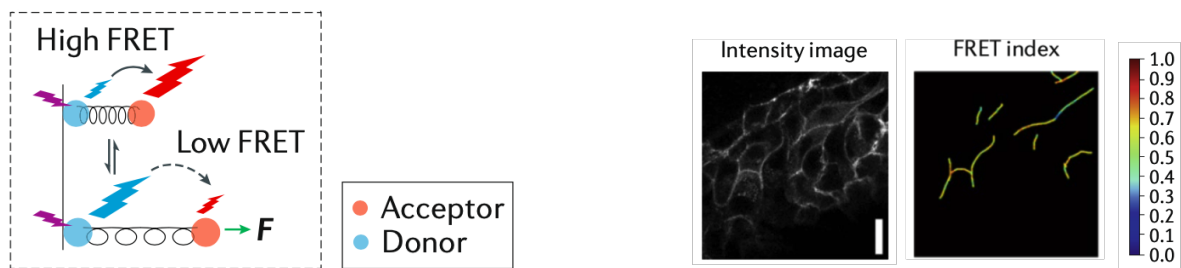


**Figure 1.15:** Left: sketch of a spring connecting one donor and one receptor. Right: Junctional tension reported by FRET sensors in an epithelial monolayer in 2D. (Narayanan et al., 2020)

### Laser manipulation

Cell-cell contacts are maintained in epithelia through adherens junctions, which can be thought of as one-dimensional structures. Tension at adherens junctions is a line tension in this case. We have two techniques for measuring this tension that includes perturbing the cell-cell junction with light: optical tweezers and laser ablation; the latter may also be used at tissue scales to estimate stress. Both techniques are applicable inside living samples due to the penetration of light.

Optical tweezers use a highly focused laser beam to exert small forces to manipulate nanometer-size dielectric particles. The focused beam contains a very strong electric field gradient which creates a gradient force (Fig.1.16) that pulls the particle along the optical axis ( $z$ ) and in the transverse plane ( $x, y$ ), towards the highest intensity region, which is the beam focus (dashed line in the middle panel Fig.1.16). Due to momentum conservation: photons absorbed or scattered by the tiny dielectric particle give the dielectric particle momentum scattering force (Fig.1.16). The scattering force pushes the particle away from the beam focus in the direction of incident light. The gradient force must dominate the scattering force to make an effective optical trap. Optical tweezers can manipulate injected particles within cells (Svoboda & Block, 1994). It should be noted that optical tweezers can achieve a non-invasive manipulation in living tissues by directly trapping subcellular structures such as the nucleus or the membrane (Bambardekar et al., 2015).

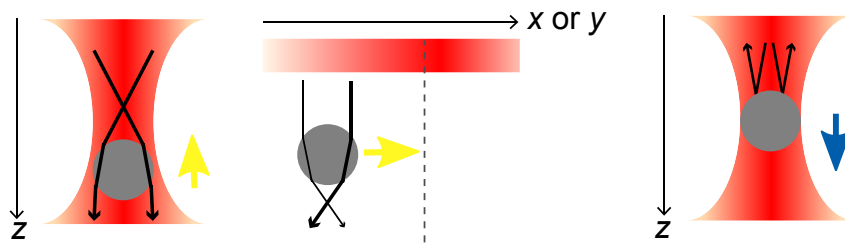


**Figure 1.16:** The gradient force (Yellow arrows) and scattering force (Blue arrows). The black arrows indicate the scattering and refraction of light. Adapted from (Sugimura et al., 2016)

Laser ablation is a method using a tightly focused pulsed laser to disturb biological structures. This method has been used to make cuts at the subcellular (Ma et al., 2009), cellular (Farhadifar et al., 2007), or tissue level (I. Bonnet et al., 2012; Etournay et al., 2015). Laser ablation generally causes the expansion of the targeted structure, whether it is a junction or a region of tissue (Fig.1.17). This indicates that prior to ablation, the ablation region and its surroundings were under tension in the opposite direction of expansion. An ablation followed by shrinkage, on the other hand, would indicate tissue compression. Ablated structures usually undergo a damped elastic recoil. The initial speed of the recoil provides a local estimate of the tension-to-viscosity ratio. The

technical details of this method will be covered in the following section (see Method).

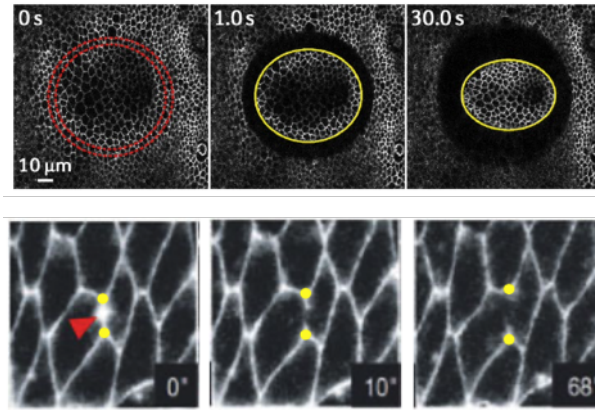


**Figure 1.17:** Top: Circular laser cut on a *Drosophila* embryo showing a differential tension along two axis (I. Bonnet et al., 2012). Bottom: Point laser cut on a single junction of *Drosophila* embryo (Rauzi et al., 2008)

The techniques presented above are local and in addition are mostly invasive, meaning they can cause tissue damage. Given that the tissue is mechanically responsive, mechanical stimuli may alter the original properties of the tissue itself, emphasizing the need to develop less invasive methods for measuring cell mechanical properties. Numerous attempts have been made since then to develop non-invasive methods for measuring the forces in biological tissue. One non-invasive technique is a image-based one that involves inferring force from the geometry of the cell contacts of the tissue. This method will be discussed in more detail in Chapter 3.

## 1.7 Physical models and simulations

From the biomolecular level to the tissue level, we have developed a more quantitative view of tissue morphogenesis, thanks to advanced imaging and genetic technologies. Following such developments, mathematical and physical modeling established a framework for validating quantitative observations and providing effective quantitative prediction.

Based on energy concepts from physics, a tissue state can be defined as the sum of all the energy of all the cells. Mathematical models can simulate tissues by representing bio-

logical cells as distinct entities and incorporating force generated at the cellular level. The main advantage of these mathematical models is the ease with which cell level processes like cell division, intracellular processes, and single-cell variability within a cell population can be integrated. Lattice-based models, off-lattice, and hybrid discrete-continuum models are the three major types of agent-based models for tissue simulation. I describe below lattice based-models and vertex models.

The lattice-based model has been used more to study collective cell behavior. The cellular potts model (CPM) was first proposed for the simulation of cell sorting as a modification of a large- $Q$  Potts model (Graner & Glazier, 1992). CPM was then widely used in the study of morphogenesis (Marée et al., 2007). Cells are described in CPM as deformable objects with a defined volume that can adhere to one another and to the medium in which they live. The formalism can be extended to include cell behaviors such as cell migration, growth and division, and cell signaling. Although the model was designed to describe biological cells, it may also be used to model specific components of a cell or even regions of fluid (Sanyal & Glazier, 2006).

Vertex models are a class of models that treat cells as discrete objects that are approximated by two-dimensional polygons representing cellular junctions and in which each vertex moves in response to forces produced by growth, junctional tension, and pressure inside each cell. The origins of these models can be traced back to the early study of soap bubbles (Marder, 1987), foams (Okuzono & Kawasaki, 1995), or grain boundaries (Kawakami et al., 1989); surface tension and pressure drive dynamics in any of these processes. The method was first applied to cultured epithelial cells in monolayers as the first time it was used (Honda & Eguchi, 1980). Following that, vertex models were used to investigate various cellular processes occurring within epithelia, such as cell motility (Bi et al., 2016), adhesion (Nagai & Honda, 2009), mitosis (Hufnagel et al., 2007), and delamination (Marinari et al., 2012). They are more difficult to implement and also more costly to run. As cells move past one another during a simulation, regular updates of the polygonal junction connections are necessary.

# Chapter 2

## Method

This chapter will present the experiments that have been carried out and analyzed, including experiments on the *Drosophila notum*, mesoderm, and germband. Live imaging and laser ablation were both conducted on those different tissues. All will be covered here in this chapter, from sample preparation to laser ablation protocol to image processing.

### 2.1 Sample preparation

#### Pupa preparation (Notum)

The pupa preparation follows the protocol described in (Shivakumar & Lenne, 2016). The fly was collected at 21 hours APF (after puparium formation). The puparium case should be removed from the pupa with forceps without damaging the pupa. Following that, the dissected pupae should be mounted on a slide. A piece of gum tape should be stuck to a slide, and silicone grease glue should be applied to the tape's four corners to support the coverslip. The ventral side of the pupae is then attached to the tape. Before mounting the coverslip, a tiny drop of oil (e.g., Voltalef oil) should be placed on a coverslip. The coverslip can be positioned precisely so that the oil droplet is exactly above the target tissue. Finally, gently press the coverslip against the adhesive silicone grease, ensuring that the droplet touches the tissue without damaging the pupa.

### Embryo preparation (mesoderm and germband experiments)

The embryo was collected at the proper time (two hours after egg laying for mesoderm and three hours for germband). The chorion must first be removed. The chorion can be removed by first rocking the embryos for 50 seconds in 50% chlorine, washing them with water, and pilling the chorion with a needle. Place the embryo on an agar plate with the interest area facing up. Add a tiny drop of glue on a coverslip and place it on top of the embryo, gently pressing the coverslip to ensure that the embryo stick to the coverslip. A drop of halocarbon oil is finally applied to the embryo. The embryo will then be directly placed under the microscopy with the coverslip. For more details, see (David et al., 2012)

## 2.2 The strain used for experiments

-For the experiments in the *Drosophila notum*, Ecad:GFP/Sqh:MCherry flies were used.

-For the experiments in the *Drosophila ommatidia*, E-CAD:GFP; N-CAD:mkate2 flies were used (E. H. Chan et al., 2017). Mosaic experiments were also described in a previous paper (E. H. Chan et al., 2017).

-For the experiments in the *Drosophila germband*, a ; E-cad::GFPKI fly line was used as wild type, embryos from a ; tor4, E-cad::GFPKI were used as Torso  $-/-$  and dsRNAs against even-skipped injected in embryos form ; E-cad::GFPKI flies as previously described (Bertet et al., 2004; Collinet et al., 2015) to obtain eve loss-of-function embryos.

-For the mesoderm and germband experiments in 3D, Myo-II:GFP/Gap43:MCherry (Tetley et al., 2016) flies were used.

-For quail embryo stainings, quail embryos were fixed in ice cold 4% formaldehyde/PBS for at least 1h, permeabilized in PBS/0.1% Triton X-100 (PBT 0.1%) before a blocking step in PBT 0.1%/2% BSA (from Roche)/10% FBS (from Gibco). Primary antibodies used in this study are mouse anti-ZO1 (Invitrogen ZO1-1A12), rabbit anti-pMyosin light chain 2 (Cell Signaling Technology CST-3671S and CST-3674S), mouse anti-Catenin (BD Transduction Laboratories™, clone 14) and rabbit anti-h/mCaspase3 (RD Systems

AF835). Secondary antibodies coupled to AlexaFluor 488, 555, or 647 were obtained from Invitrogen and used at 1:200 dilutions. Embryos were then mounted with DAPI-containing Fluoromount-GTM (eBioscience) between slide and coverslip. The detailed protocol and quail strain see (Saadaoui et al., 2018)

## 2.3 Laser ablation

Ever since the laser was discovered, people have used them to alter the physical state of materials. However, continuous lasers tend to overheat samples, which becomes even more important when the sample is biological. In comparison, the pulsed laser seems to be a viable alternative. The duration of the pulse characterizes the pulsed laser. The femtosecond laser is the one with a duration of a femtosecond order pulse ( $10^{-15}$  seconds). The femtosecond pulsed laser is well-known for some important advantages over conventional lasers. First, the ultrashort pulse duration enables femtosecond scale measurements with extremely high temporal resolution. Second, the focused ultrashort pulses may produce extremely high energy intensity. These characteristics allow accurate subcellular ablation.

### 2.3.1 The setup of laser ablation

The laser ablation setup (Fig.2.1) was described and evaluated in-depth for the first time (Rauzi et al., 2008), and it has since been updated and applied to additional applications (E. H. Chan et al., 2017; Palavalli et al., 2021). The laser is a Yb::YAG solid-state laser (T-Pulse, Amplitude systems, Pessac, FRANCE) with 1W average power, 1030 nm wavelength with spectral width 7nm, a repetition rate of 50 MHz, and pulse duration of 160 femtoseconds(fs). High-speed mirror galvanometers are employed to move the laser beams and produce different shapes of cuts. A commercial spinning disc is coupled to an inverted microscope with a high numerical aperture and a high magnification IR corrected objective lens. The inverted microscopes are suitable for laser ablation setups because

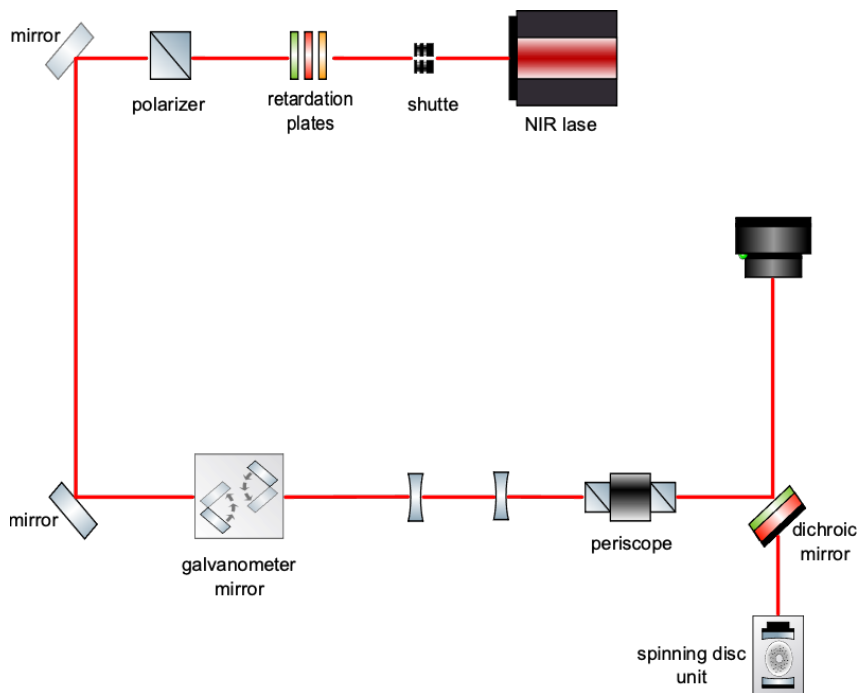


**Figure 2.1:** The setup of laser ablation

they can have accessible space below the back aperture of the objective.

### 2.3.2 Laser and material interaction

The near-infrared (NIR) femtosecond laser operates by focusing an ultrashort, high repetition rate laser light into a high numerical aperture microscope objective, resulting in extremely high peak intensities that drive the multiphoton absorption process.

Multiphoton excitation is a non-linear phenomenon that enables molecules to be excited by photons of lower energies (longer wavelengths) than those associated with typical quantum energy levels. The phenomenon may be thought of as the electric field becoming strong enough to perturb the electrons enough to enter a higher state through a series of "virtual" states (Kaiser & Garrett, 1961). The absorption of  $n$ -photons is proportional to the  $n$ th-power of the required light intensity. The laser pulse's peak power is selected so that adequate photon intensity is located only in the central portion of the Gaussian-shaped ultrafast laser pulse's temporal profile. As a result, the photon interaction is confined inside the limited volume of the centered laser spot.



In addition to the key parameters (energy intensity and pulse duration), several other important parameters influence the laser-material interaction, such as the polarization, the laser light wavelength, the pulse repetition rate, the duration of the irradiation, and the numerical aperture of the focusing lens. The parameters of our laser will be provided in the next section.

### 2.3.3 Laser ablation protocol

The infrared laser is controlled by galvanometer mirrors; thus, laser calibration is needed before each series of experiments. It entails determining the proper voltage to feed the galvanometer mirrors to achieve the desired laser-cut form, such as a circle, line, or point cut.

-Notum: The single junctions' ablations were performed on the notum (21h APF). The laser used was almost full power of the laser, and 350mW at the back focal plane of the objective. The duration of the ablation laser was 0.25s. The ablation movies were taken in the apical plane, indicated by tagged E-cadherin, with an exposure time of 100ms. Live images of notum without ablation were taken with the same conditions and imaging parameters.

-Mesoderm: The laser parameters are the same as those used for the notum, except that the laser power was 260mW instead of 350mW. The ablations were used to change the cells' apical area. A stack was acquired with a Z-step of  $1\mu m$  as the reference stack. After that, the ablation was carried out by identifying the target cell (or junction). Once the ablation was completed, movies of stacks were acquired.

Movies of stacks consisting of 35-40 slices (for a depth of 35-40 $\mu m$ ) were also acquired in the early mesoderm without ablations.

-Retina: experiments were conducted by Shivakumar P.C. (E. H. Y. Chan et al., 2017)

-Germband: line cut experiments were from (Collinet et al., 2015). Junction cut experiments for the 3D analysis were performed by myself. It's the same procedure as on the mesoderm.

## 2.4 Image analysis

The majority of the experiments in this thesis used laser scanning microscopes to generate images and movies. Thus, image processing is a critical step in the quantitative analysis of the experiences. This section describes the different image processing pipelines that have been deployed.

### 2.4.1 Static analysis

Image Segmentation is a technique for partitioning a digital image into segments (sets of pixels) for digital image processing and computer vision. The goal is to simplify the representation of an image into something more representative and easier to analyze. Segmentation of images is usually used in images to locate objects and boundaries (lines, curves, etc.). More precisely, image segmentation is the process of assigning a label to each pixel in an image such that pixels with similar characteristics share the same label. In our case, the cell junctions must be segmented into binarized segments in order to extract the geometric information present in the tissue. To segment the images, I first used TissueAnalyzer (Aigouy et al., 2016), a FIJI plugin. This plugin employs the watershed method to convert the grayscale image to a topographic map that visually separates adjacent drainage basins using different brightness values to represent the height of each pixel. The peaks of the ridges would have the highest value. With the segmented image, we can obtain the positions of all vertices and additional information such as the intensity, length, orientation of junctions, etc. (Fig.2.2). Additionally, information about the cells is given in a separate datasheet, which includes the index of junctions surrounding each cell, as well as cell position, perimeter, area, and intensity. This geometry information was then passed to force inference or used to extract cell and junction features such as cell area, junction intensity. It is important to be aware that the accuracy of image segmentation is particularly important, especially for the Laplace method (section 4.5), which relies heavily on the accuracy of the image segmentation, while the Bayesian method is more

likely to be unaffected by the noise introduced by image segmentation.

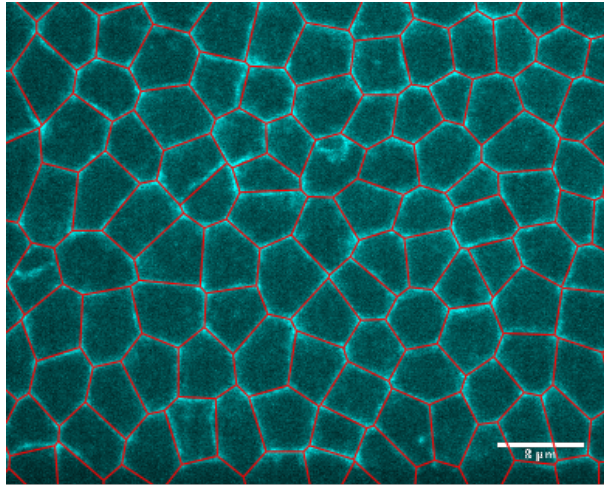


**Figure 2.2:** An example with segmented junctions

TissueAnalyzer enables segmentation to be reasonably fast and semi-automated while also allowing for manual correction of auto-segmentation. Automated segmentation is never flawless, necessitating manual adjustments by the operator. Clearly, the degree to which automatic segmentation succeeds is dependent on the quality of the input images. Segmentation becomes a time-consuming process for large stacks of video, which is why I turned to deep learning for truly automated segmentation (see next section).

### 2.4.2 Dynamic analysis

In general, we attempt to quantify the dynamics of tissue displacement following ablation using ablation experiments. Indeed, the junction recoils after ablation, much like a cut rubber band recoils. The recoil velocity post-ablation is often used as a proxy for junction tension (I. Bonnet et al., 2012; E. H. Y. Chan et al., 2017; Ma et al., 2009; Rauzi et al., 2008). We used different strategies to estimate the recoil velocity for various experiments. Notum:

To measure the recoil velocity in the notum, I used kymographs along lines parallel to the ablated junctions to automatically track vertices' movement.

The obtained kymographs have two lines that represent the vertices' movements

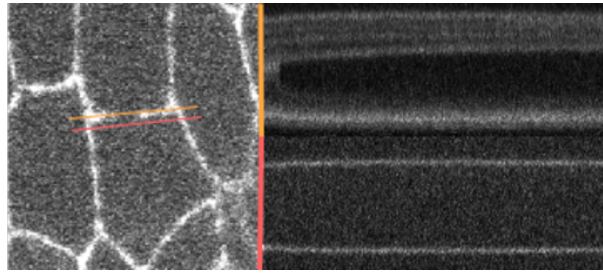


**Figure 2.3:** The kymograph obtained along the junction (red line) and next to the junction.

(Fig.2.3. Kymographs were then oversampled and treated with a Gaussian filter to avoid pixelation effects in vertex detection. As shown in Fig.2.3, a kymograph taken along the junction (orange line Fig.2.3) produces two thick lines, making it impossible to track the vertices' positions. Vertices positions were determined at each time point with a Gaussian fit (along the red line in Fig.2.4) of the intensity. Then the mean of the Gaussian fit will give the position of the vertex. Despite these efforts, the data can still be quite noisy.

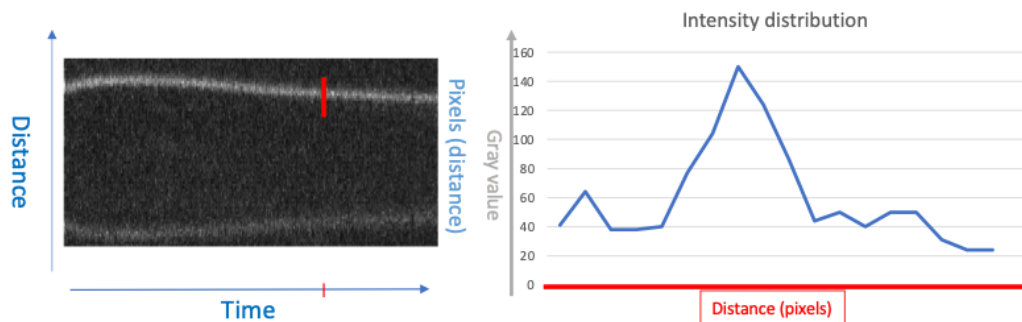


**Figure 2.4:** The intensity profile of the kymograph

Besides, we needed to fit each single opening curve separately, without the possibility to average over several junctions, as we wanted to make single-junction comparisons with force inference. This implies fitting the initial recoil velocity on rather noisy opening curves. Thus, to determine the initial velocity, we performed a linear fit of the first 5 seconds of opening. The fitting time was determined empirically. Too short fitting times are very much affected by noise, and too long fitting times yield poor estimates as the opening is rather exponential or bi-exponential than linear. Note that we used linear fits of the

onset of relaxation rather than exponential or bi-exponential fits of the whole relaxation process for a practical reason. Only fitting the first few points focuses error minimization on the onset of relaxation, whereas fitting the whole relaxation with exponentials might overall give a better fit, but possibly at the expense of the onset of opening, as it is only a small subset of the relaxation curve. Note that exponential fits with a larger weight for the first few points could also have been used.

Retina:

In the *Drosophila* retina, automated detection with kymographs could not be used due to smaller cells, edge curvatures, and higher signal loss following ablations. Hence, we used a manual tracking approach of the vertices using FIJI. In this case, opening curves could be averaged over several junctions, which yielded less noisy curves. Hence, we could estimate the opening velocity on a much smaller timescale, looking at the first 250 ms. Note that the gradation observed is still found if we fit curves independently on a longer timescale (as it is done in the notum), then average velocities for each junction type. This strategy was actually the one used in our previous paper (E. H. Y. Chan et al., 2017) and yielded a similar gradation. Velocities determined here are closer to the actual "initial" velocity, as they are measured on a shorter timescale after the cut. The higher values found here suggest that it is indeed the case.

Germband:

In the *Drosophila* germband, the opening velocities were determined by Particle Image Velocimetry (PIV), as several junctions are involved in the opening process. The measurement routine was described in a previous article (Collinet et al., 2015). In short, PIV is computed between a snapshot taken upon ablation and a snapshot taken 2 s after ablation. The velocity field is averaged in a region adjacent to the cut line to obtain a scalar velocity value.

Quail:

In the quail embryo, tissue strain was evaluated based on the deformation of the tissue

2 minutes after the cut from a PIV analysis of the resulting time-lapse movies. Note that the initial opening velocity could not be measured since relaxation occurred on a time scale comparable to the time taken to make the cuts (see (Saadaoui et al., 2018) for details). This prevented a quantitative analysis of initial recoil velocities vs. inferred stress.

Area and shape changes were the primary analysis in the 3D study of the apical-basal coupling. To determine the area or shape changes of each cell in three dimensions, all the images from apical to basal for all the frames must be segmented. Segmentation for a big movie of stacks required a tremendous amount of time, so I turned to an open-source software EPySeg which uses deep learning to segment membrane-stained epithelial tissues automatically and very efficiently (Aigouy et al., 2020). The author included different net structures available, such as Unet, LinkNet (Chaurasia & Culurciello, 2017) architecture with a VGG16 encoder (Jaderberg et al., 2015). The software provided two pre-trained models, which worked well on my images of the apical planes. The most basal planes could not be segmented well with those pre-trained models. I trained my model with 60 images for a round of 150 epochs using the VGG16. The model was used for segmenting the 3D data of the mesoderm and germband. The segmented images are then transferred to a custom geometry extractor function, which extracts geometry information such as cell area, junction length, and vertices positions from the segmented epithelial tissue image. Geometry data is stored in a separate .sql database file. The geometry extractor can be used by force inference as well, which means that the cells, junctions, and vertices are all ordered identically. This enables the direct comparison between the force inference results and geometry (section 5.3). Additionally, a customized tracking algorithm was implemented based on the area overlaps and minimum displacement of cells within sequences of images using a Kuhn–Munkres algorithm (Kuhn, 1955). This algorithm can also be used to track the output of force inference directly. The analysis pipeline is depicted in Fig.2.5. It is worth noting that tracking cells in time and space is highly dependent on the reference cell. The reference cell is the cell located at the given

t and z. The cell was always tracked in z-order for time t and reverse z-order for time t+1. The cell area was measured using the appropriate pixel size during the geometry extraction step. To facilitate tracking, the calculated area is labeled with cell, slice, and frame indexes. The volume value was computed as part of the cell tracking process.

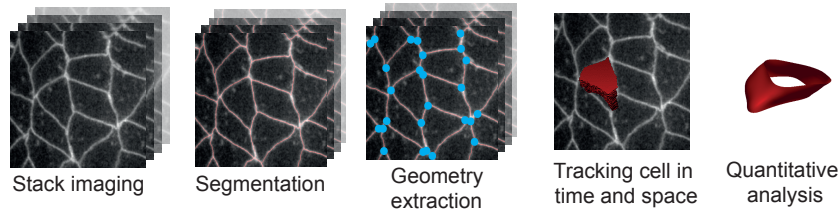


**Figure 2.5:** Pipeline of the 3D analysis.

## 2.5 Simulation of ablation

Estimation of the recoil velocity after ablation appears to be critical in single-junction ablation experiments. However, this recoil velocity became hard to estimate in some instances, especially when the angle  $\theta$  (Fig.2.6) is small. Vertices with a flatten angle typically have a low degree of freedom, implying that their displacement is small. This displacement could be so small that no apparent recoil is measurable. As a result, we wondered if any tension had been underestimated, given that one of the vertices movement was not measurable. To further substantiate this hypothesis, we created a toy model that simulates the ablation process. Note that these results were not used for our analyses and are given here as a side note rather than as a method for this work. This model is composed of five connected springs that serve as a model of connected junctions. By adjusting the original spring parameters, we can define the network's initial configuration, the angle  $\theta$ . The central spring is removed to simulate the laser ablation procedure on the central junction. The rest of the network will relax after the central spring is removed, much as the ablated junction will recoil. If they have the same tension, both vertices recoil

at the same speed. But the displacement is smaller when the angle is high. Hence the bias due to the fit on the estimation of the initial recoil speed depends on the angle (Fig.2.6A ). As a result, it might be worthwhile to re-adjust the estimated recoil velocity to take the opening angles into account. Additionally, these simulations also illustrated that the time window used for the fit also affects the estimate of the recoil velocity (Fig.2.6C ). This is also true with real tissues (see Fig.A.1).

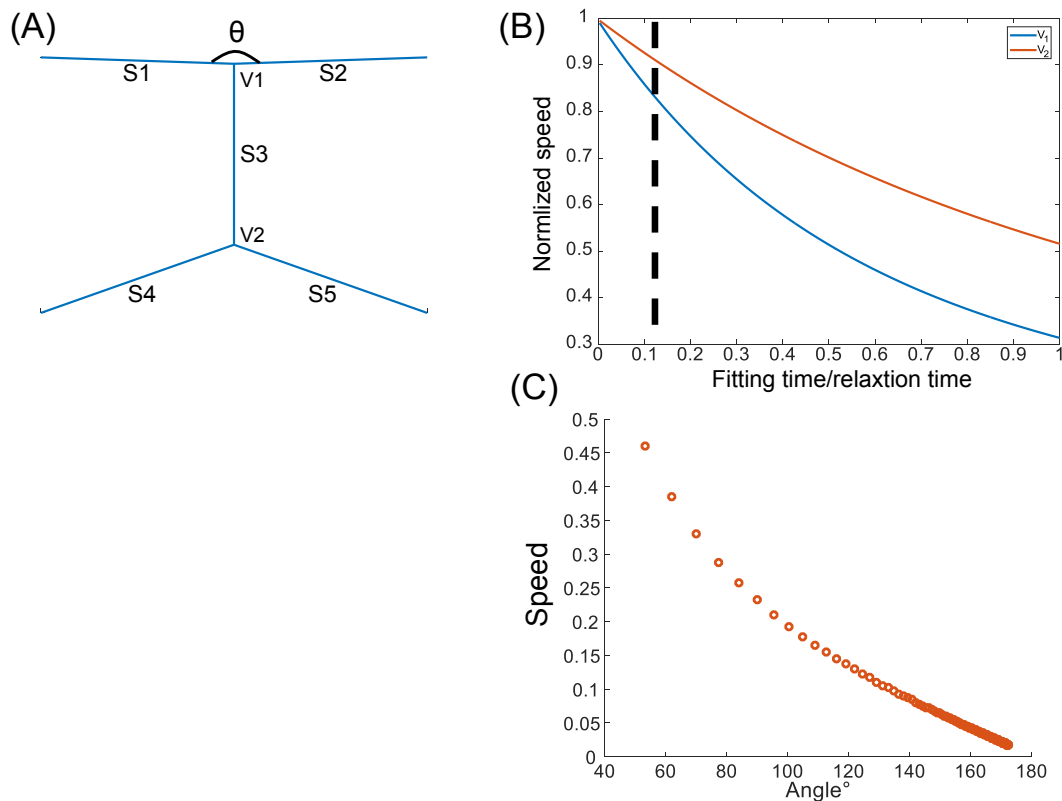


**Figure 2.6:** (A) Schematic of the simple model with five connected springs. (B) Recoil speed of two vertices using different fitting times for the speed. (C) Speed of V1 with different angles.



# Chapter 3

## Force Inference

### 3.1 General and historical information about inference

As discussed in the first chapter, the cell surface tension drives cell movements and arrangements. The actomyosin-generated cortical tension tends to shorten the cell junctions in which they act. In contrast, the force generated by adhesion complexes tends to elongate cell junctions and reduce tension. The intracellular pressure generated by cytoplasm and frictional response to deformation counteracts the tension to maintain the size of a cell. Due to the low Reynolds number within the cell, the inertia is largely negligible (Purcell, 1977). Additionally, if cell and tissue movements are slow enough, viscous forces become negligible in comparison to all other forces that define the physics of the biological system. Based on those hypotheses, only two primary forces can adequately explain the mechanics of cells and tissues: junctional tension and cell pressure. Junctional tension is assumed to be the same along the junction. Similarly, the cellular pressure may be believed to be constant inside any given cell. These assumptions are the basics of the method of force inference. With these assumptions, the forces between tensions and pressures should be balanced at each vertex. For instance, if the tensions at the three junctions are equal, their angles will all be  $120^\circ$ . Furthermore, if the tensions at the three junctions are different, the angles will be different as well (Fig. 3.1). If we assign a unit tension to

one of the junctions (Fig. 3.1), we can deduce the tensions in the other junctions from the angles we can directly measure. This procedure can be repeated for all vertices to obtain all tensions. Additionally, we can repeat this procedure for the pressures in order to obtain all of the pressures (see next paragraph).

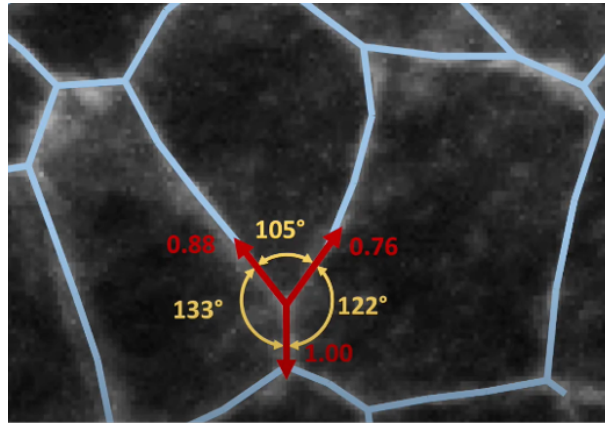


**Figure 3.1:** The tensions can be inferred from the angles formed between the junctions. The red arrows show the tensions acting on the three connected junctions.

With advances in imaging and computation in the 2000s, Brodland and his collaborators revised the principle underlying the inference of forces based on cell shape (Chen & Brodland, 2000; Brodland et al., 2007; Yang & Brodland, 2009). Their work largely inspired subsequent work. Force inference requires writing force balance equations at each vertex. A general difficulty is the indefiniteness introduced by image boundaries, where junctions are connected to one vertex only. The full inverse problem (one tension per junction and one pressure per cell) is generally underdetermined, with fewer equations than unknowns (Ishihara et al. 2013). Numerous strategies can be used to mitigate this underdetermination and generate a set of plausible tensions and pressures, as Roffays and co-workers recently discussed in their review (Roffay et al., 2020).

For example, Chiou and co-workers used force inference to investigate dorsal and ventral formation in *Drosophila*. They assumed that intracellular pressure is constant across the tissue. So that all junctions are straight lines and that the pressure difference between neighboring cells is assumed to be negligible (Chiou et al., 2012). The problem

then becomes overdetermined (more equations than unknowns) and can be solved by computing the pseudo-inverse of the associated matrix (Chiou et al., 2012). They found mechanical anisotropy at the onset of ventral furrow formation of *Drosophila*. As junctions are rarely perfectly straight, suggesting pressure differences between cells, we chose to discard the assumption of homogeneous pressure.

Later, Brodland and co-workers developed a force inference toolkit called "CellFIT," which is available online for users. In this version of force inference, they supplemented the contact angle measurements by measuring the radii of curvature between each pair of adjacent cells. Using the Young-Laplace law provides another set of conditions that lead to an overdetermined problem (Brodland et al., 2014). With the application on different tissue samples, they demonstrated considerable variability in forces within a cell population, with significant differences between populations. This approach can be an ideal solution if junction tangents (for tensions) and curvatures (for pressures) can be accurately measured. The implementation details will be described in the section 3.2.

More advanced statistical methods might be used to calculate both tension and pressure without measuring curvatures (Ishihara & Sugimura, 2012). One can adopt a Bayesian approach and incorporate statistical expectations for the system as a prior, for instance, assuming a Gaussian distribution of tensions. This is a novel framework of inverse problem for estimating cell pressure and junctional tension. The authors used this method to elucidate developmental changes in tensile force patterns in the dorsal thorax of *Drosophila*. This method is a good strategy when curvature measurements are difficult. This method is detailed in Section 3.3 of Bayesian force inference.

The force inference method determines tensions and pressures solely with tissue images, rendering it entirely non-invasive. Additionally, there are no assumptions made regarding the biophysical sources of tensions and pressures in the model. The methods do not depend on the mechanical characteristics of the cell membrane, including whether it is elastic, viscous, influenced by adhesion complexes, or changed by cortical components. In a sense, force inference operates one level up from these important details. It simply

provides the total relative tension acting along any given junction without regard to how it is generated. The method offers estimations of mechanical properties from single-cell to tissue-scale, allowing direct comparison of the inferred forces with the action of adhesion or motor molecules, cell-level dynamics, and tissue-scale morphogenesis. However, force inference is based on the tissue geometry that is extracted from the tissue images. The method is therefore highly dependent on the limitations of the imaging technique. Image resolution will be an important limiting factor, and geometry extraction will be another important factor. Geometry extraction is usually performed by an image processing process called segmentation. The limitation of segmentation is then critical for accurate geometry extraction. These limitations will be discussed in the following chapters.

### 3.2 Laplace force inference

Each cell's junction's curvature is assumed to be a consequence of pressure differences (Young-Laplace law), and tensions along such junctions are presumed to be uniform within each junction. These are the fundamental assumptions of the method, which we named Laplace force inference to differentiate it from another method, Bayesian force inference, which will be discussed later.

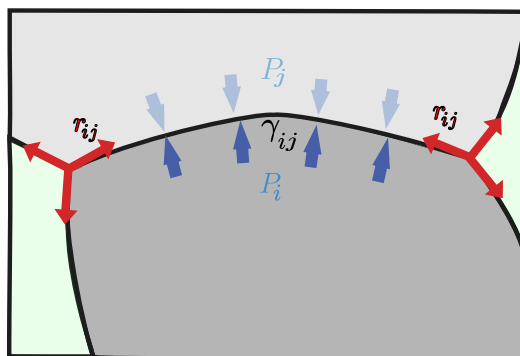


**Figure 3.2:** The cell-cell interface with a curved junction.  $\gamma_{ij}$  is the line tension of the junction,  $\vec{r}_{ij}$  is the unit vector.

As shown in Figure 3.2, the junction between cells  $i$  and  $j$  carries a tension  $\gamma_{ij}$ , and has

an intracellular pressure differential that results from the difference between the intracellular pressures  $p_i$  and  $p_j$  (Fig. 3.2). The relation between the tension and the pressure can be presented with the Laplace law:





$$\Delta p_{ij} = \frac{\gamma_{ij}}{\rho_{ij}} \quad (3.1)$$

Where,  $\rho_{ij}$  is the radius of curvature  $\gamma_{ij}$  is the tension and  $\Delta p_{ij}$  is the difference of pressure between cell i and j. The tension in 2D has the unit of force per unit length ( $N/m$ ).

When the pressure on one side of the cell junction is greater than the pressure on the other, the cell junction is curved. The higher the pressure difference, the more tension there is at the cell junction. There would be no curvature if there were no pressure difference on the junction. A set of equations is that the vector sum of the forces applied to each vertex equals zero (Fig 3.2):

$$\Sigma \gamma_{ij} \vec{r}_{ij} = \vec{0} \quad (3.2)$$

The vector force  $\gamma_{ij}$  of a cell junction tension acting on a vertex must be pulling from the vertex and tangent to the junction as it approaches the vertice.  $\vec{r}_{ij}$  is the unit vector the limiting angle at which the membrane along the junction between cells i and j approaches the vertex (red arrow in Figure 3.2). The system of equations is becoming increasingly overdetermined as more cells are added (Figure 3.3).

	Vertices	Junctions (Unknown Variables)	Equations
	1	3	2
	2	5	4
	6	12	12
	10	19	20

**Figure 3.3:** Geometric information: number of vertices, junctions and equations. The equations system is generally overdetermined.

### 3.3 Bayesian force inference

Rather than writing the force balance in terms of tensions, the force balance would be equal to the sum of the tensions of three joint junctions and the pressure exerted by three adjacent cells (Fig. 3.4). The force balance is expressed as:

$$\alpha\vec{T}_1 + \beta\vec{T}_2 + \gamma\vec{T}_3 + \delta\vec{P}_1 + \varepsilon\vec{P}_2 + \epsilon\vec{P}_3 = \vec{0} \quad (3.3)$$

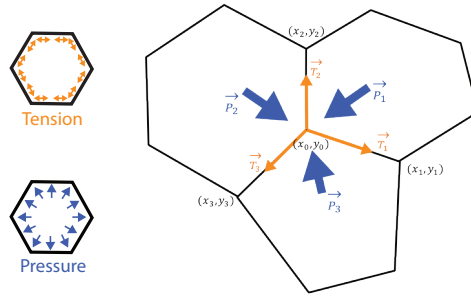


**Figure 3.4:** Schematic of force balance on one vertex, blue arrow: cell pressure, orange arrow: junctional tension.

Where,  $\alpha, \beta, \gamma, \delta, \varepsilon, \epsilon$  are the coefficient constants. This equation can be projected on the  $x$  and  $y$  directions:

$$\begin{aligned} \alpha_x T_1 + \beta_x T_2 + \gamma_x T_3 + \delta_x P_1 + \varepsilon_x P_2 + \epsilon_x P_3 &= 0 \\ \alpha_y T_1 + \beta_y T_2 + \gamma_y T_3 + \delta_y P_1 + \varepsilon_y P_2 + \epsilon_y P_3 &= 0 \end{aligned} \quad (3.4)$$

Here  $(T_1 \dots P_3)$  are the norms of the vectors  $(\vec{T}_1 \dots \vec{P}_3)$ . The equations will be a set of  $2N$  equations;  $N$  is the number of vertices in the image. Tension coefficients are calculated with the coordinates of the two adjacent vertices, for example  $\alpha_x = \frac{x_1 - x_0}{\|x_1 - x_0\|}$ . Since the pressure acts uniformly on the member of the cell (Fig. 3.4), the pressure coefficients are calculated with the coordinates of two neighbor vertices, for example  $\delta_x = \frac{y_2 - y_1}{2}$ .

Consider a tissue with a number of cells  $N$ , the number of cells on the border is  $R$  (Fig. 3.5). If all the junctions are 3-ways, the number of junctions will be  $3v/2$ . Euler's formula indicates that the number of junctions and vertices are  $3N + 2R - 3$  and  $2N + R - 2$ ,

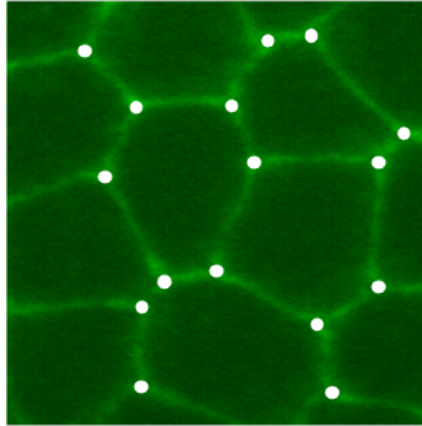


**Figure 3.5:** An example tissue illustrates the indefiniteness

respectively. In most cases, the number of vertices will be less than the number of cells plus the number of junctions. Knowing the 4-way vertex will make the number of vertices even smaller. As shown in the figure (3.5): the total number of unknown variables is 33, which is the sum of the number of cells and junctions. The number of equations will be twice the number of vertices (x and y directions): 32. As a result, we end up with an underdetermined problem in which there are more unknown variables than equations.

To handle this underdetermined problem, one can adopt the framework of Bayesian statistics (Ishihara & Sugimura, 2012). The force balance equations can be written as:

$$Ap = 0 \quad (3.5)$$

$A$  is  $n * m$  matrix in which  $n$  and  $m$  are the numbers of equations and unknown variables, respectively.  $p$  is the vector containing all unknown tensions and pressures that are needed to be solved. As a result of the topological problem just explained,  $n$  is smaller than  $m$ , and thus we have an underdetermined problem. The Bayes's theorem in our case can be written as:

$$P(p | b) \propto P(b | p)\pi_T(p) \quad (3.6)$$

$b$  is an observable quantity (which is 0 here),  $P(p | b)$  gives the posterior distribution, with which unknown values of  $p$  are estimated.  $P(b | p)$  is the likelihood function,  $\pi_T(p)$

is the prio. If we assume that tensions are normally distributed around a positive value  $T_c$  with variance  $\omega^2$ , the prior reads :

$$\pi_T(p; \omega^2) = \frac{1}{(2\pi\omega^2)^{\frac{m'}{2}}} \left[ -\frac{1}{2\omega^2} \sum_{ij} (T_{ij} - T_c)^2 \right] \quad (3.7)$$

$T_{ij}$  is the tension of the junction between cell  $i$  and  $j$ . As a result of unavoidable observation errors and system errors, the errors are assumed to obey a Gaussian distribution with variance  $\sigma^2$ . Then the probability to observe  $b$  under given  $p$  is written as:

$$P(b | p; \sigma^2) = \frac{1}{(2\pi\sigma^2)^{\frac{n}{2}}} \exp \left[ -\frac{1}{2\sigma^2} \|Ap - b\|^2 \right] \quad (3.8)$$

This gives the likelihood function. The most probable estimation for  $p$  is obtained at the maximum values of the posterior distribution. Maximizing the marginal likelihood (Eq 3.7) will provide estimations for  $\omega^2$  and  $\sigma^2$ . For more mathematical details about the bayesian approach, see (Sugimura & Ishihara 2012).

### 3.4 Stress determination

With the pressure for each cell and tension for each junction, a tensor at a larger scale can be evaluated using Batchelor's formula (Batchelor, 1970; Ishihara & Sugimura, 2012):

$$\sigma_{\mu\nu} = \left( - \sum_{i=cells} P_i a_i \delta_{\mu\nu} + \sum_{[ij]=junctions} T_{ij} \frac{l_{ij}^\mu l_{ij}^\nu}{\|l_{ij}\|} \right) / \sum_{i=cells} a_i \quad (3.9)$$

Where  $a_i$  is the area of cell  $i$ ,  $P_i$  is pressure,  $\delta$  is Kronecker's symbol,  $T_{ij}$  is the tension of the junction  $[ij]$  separating cells  $i$  and  $j$ , and  $l_{ij}$  the vector connecting the two vertices of junction  $[ij]$ . Stress can be computed separately for each cell or averaged over subregions of any desired size (here, 8-10 cells in the germband, and few tens of cells in the quail embryo). Red bars show principal directions of  $\sigma$ , and their length is proportional to the corresponding eigenvalues.



## 3.5 Implementations

### 3.5.1 Laplace force inference

The geometry information is extracted with the custom extractor from a segmented image (See method). The next step is to build the force balance matrix. The force balance equation should be written using the tangent of the junction on the vertex (as shown in the previous section Eq. 3.1). To determine the tangents, we performed linear fits of the first pixels of each junction (usually 5% of the total length of the junction). As shown previously, the system is overdetermined. The pseudo inverse can be used to find the solution that minimizes the deviation from perfectly balanced forces. Once the tensions are obtained and curvatures are measured, pressures can be computed using Laplace's law for each pair of adjacent cells (the pressure matrix is overdetermined again). The curvature of each junction is measured using the Taubin circle fitting method (Taubin, 1991). Finally, the obtained tensions and pressures are used to create a color-coded tension and pressure map. As previously stated, tangent and curvature determination is critical, and details of the determination method (tangent fit, curvature determination) can be critical parameters for the result of the inverse problem. This method should therefore be avoided if tangent and curvature determination are difficult.

### 3.5.2 Bayesian force inference

The TissuAnalyzer extracted geometry information was directly used to build the force balance matrix for the Bayesian method. In comparison to the previous case, the matrix should contain both tension and pressure coefficients. The coefficients are calculated with Eq 3.3 using the vertexes positions. Because of the topological constraints, this matrix represents an underdetermined problem.

After filling the matrix  $A$ , the next step is to maximize the likelihood function. To numerically maximize marginal likelihood the procedure is employed following the study

of (Ishihara & Sugimura, 2012).

Solving the force balance system entails inverting a large matrix, which is time- and CPU-consuming. We used the suitesparse library with CUDA acceleration (Davis, 2018). After inverting the matrix, we obtain all the tension and pressure. We may compare the tension and pressure distributions to the prior. The tension and pressure map are presented with a specific colormap.

### 3.6 Validation on synthetic tissues

Force inference provides relative tension estimates (and so do ablation experiments), as they are determined up to a multiplicative constant. Inferred pressures are determined up to an additive constant (hydrostatic pressure). A common convention is to scale tensions so that the average tension is 1, and to fix the reference average pressure to 0. Before applying force inference to biological tissues, we first used data generated in silico, a standard procedure to validate proper implementation (Brodland et al., 2014; Chiou et al., 2012; Ishihara & Sugimura, 2012). We generated synthetic data using Surface Evolver (Brakke, 1992), a software that uses energy minimization to drive a system governed by custom line/surface energies to equilibrium. Briefly, known tensions and pressures are assigned to a regular cell array, which is then driven to equilibrium. The synthetic tissue data was generated using Surface Evolver v2.7. Surface Evolver evolves the given surface towards its minimal energy configuration by a gradient descent method. In our case we used a classical energy function of the form (Nagai, T. & Honda, H. A 2001; Ouchi, N. B., Glazier, J. A., Rieu 2003):

$$E = \sum_{[ij]=\text{junctions}} \gamma_{ij} l_{ij} + \frac{1}{2} \sum_{i=\text{cells}} k_p (p_i - p_i^0)^2 + \frac{1}{2} \sum_{i=\text{cells}} k_a (a_i - a_i^0)^2 \quad (3.10)$$

where  $p_i$  and  $a_i$  are the perimeter and area of cell  $i$ , and  $p_i^0$  and  $a_i^0$  its target perimeter and target area.  $k_p$  and  $k_a$  are the strengths associated to the perimeter and area constraints,

respectively.  $\gamma_{ij}$  is the line tension in junction [ij], and  $l_{ij}$  its length. The pressure in cell  $i$  (“known” pressure) is then given by  $P_i = -k_a (a_i - a_i^0)$ , and the total tension of junction [ij] (“known” tension) is given by

$$T_{ij} = \gamma_{ij} + k_p (p_i - p_i^0) + k_p (p_j - p_j^0) \quad (3.11)$$

The final tissue is given by the parameter:  $-k_a$ ,  $\gamma_{ij}$  and  $k_p$ .

In the tissue simulation (Fig. 3.6B), the target area is set to 0.87 and  $k_a$  is set to 2. For the sake of simplicity, the target perimeters are all set to 0.  $k_p$  is set to 0.15. Line tensions  $\gamma_{ij}$  are randomly assigned from a Gaussian distribution (mean=1, std=1/6) prior to equilibration.

The generated synthetic tissue allows direct comparison of inferred tensions and pressures to known tensions and pressures. Bayesian inference performs very well, as shown by comparisons between the true versus inferred tension and pressure maps (Fig.3.6A–C). The correlation is excellent for both tension and pressure, with a Pearson’s correlation coefficient above 0.9 (Fig.3.6D,E), as expected for synthetic data (Ishihara & Sugimura, 2012).

We used a similar validation approach to validate our Laplace inference code. This time we used simulations of groups of cells mimicking *Drosophila* ommatidia, the only experimental system that we analyze with Laplace inference (see below). Again, we find an excellent agreement between simulations and force inference, as shown by the tension and pressure maps (Fig. 3.7 A–D). Although the system only has 6 cells and 13 junctions, the correlation remains excellent for both tensions and pressures (Fig. 3.7C.D). In this thesis, we preferentially used Bayesian inference for tissues with a large number of cells and small curvatures, that is, the *Drosophila* notum and germband, and the quail embryo. Indeed, we noticed that Laplace inference is prone to error propagation when the system size increases (see section 4.5). Briefly, this is due to the difficulty to properly determine junction tangents at vertices. Measuring tangents and curvatures requires fitting segmented,

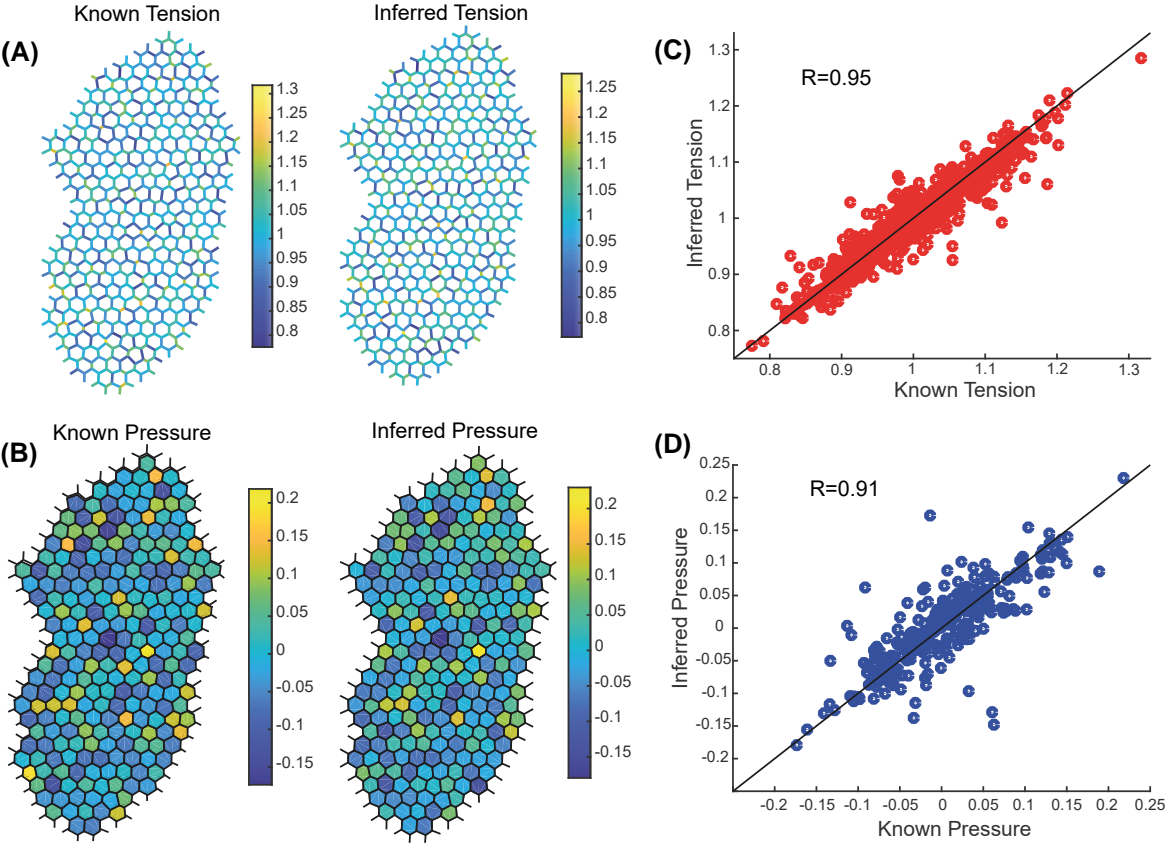


**Figure 3.6: Validation of Bayesian force inference on synthetic data.** (A) Known (left) vs. inferred (right) tension map in a tissue simulated with Surface Evolver (246 cells, 873 junctions). (B) Known (left) vs. inferred (right) pressure map. (C) Inferred tensions vs. known tensions. (D) Inferred pressures vs. known pressures.

pixelated junctions. This procedure can introduce errors that propagate to neighboring vertices and junctions when the inverse problem is solved (Section 4.5). This effect is substantial in the tissues mentioned above, as curvatures are usually tiny and thus hard to determine. Besides, junctions often appear as a very open S upon segmentation. This is a typical source of dramatic projection errors upon tangent determination. In contrast, Laplace inference is very well suited for the ommatidia of the *Drosophila* retina. Indeed, ommatidia are stereotyped units composed of only 6 cells with highly stereotyped shapes and very high curvatures, which allow averaging and therefore much easier and reliable measurements of tangents and curvatures.

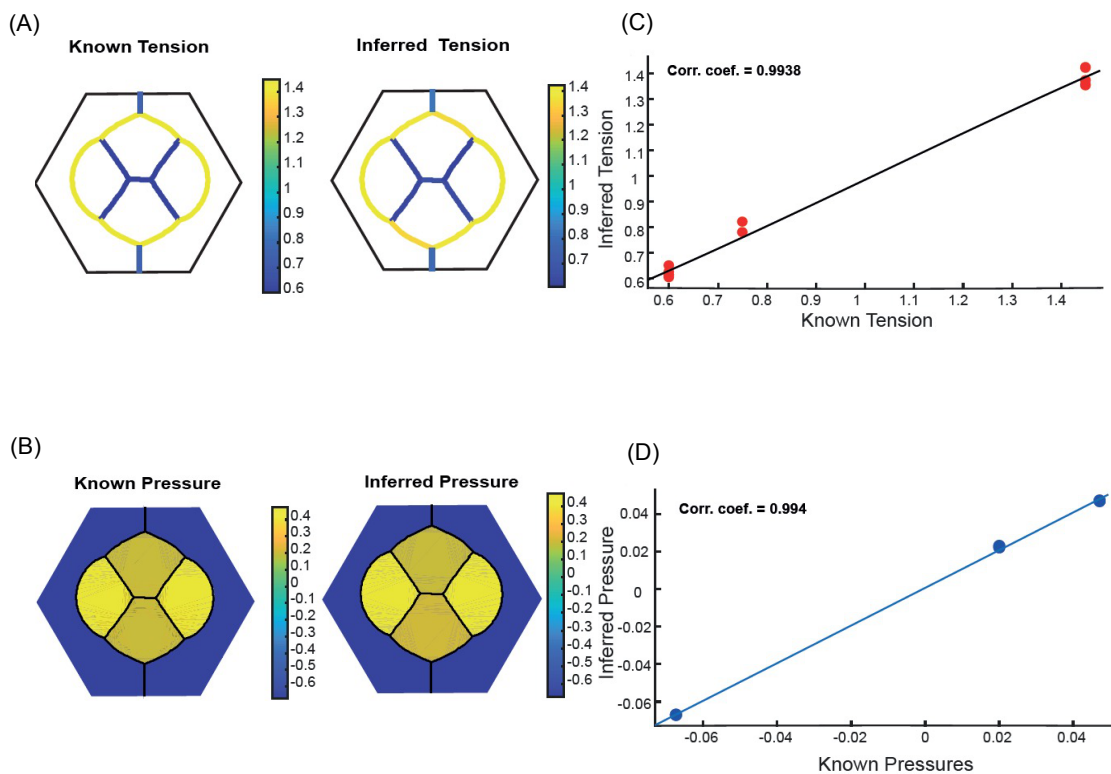


**Figure 3.7: Validation of Laplace force inference on synthetic data.** (A) Known (left) vs inferred (right) tension map in an ommatidium simulated with Surface Evolver. (B) Known (left) vs inferred (right) pressure map. (C) Inferred tensions vs. known tensions. (D) Inferred pressures vs. known pressures.

## Chapter 4

# Force inference cross-validation with various tissues

The purpose of this chapter is to explain the results of our published paper (Kong et al., 2019), which consists of a systematic, detailed cross-validation of force inference in different conditions and at different scales. We carried out our analysis at various spatial scales in four distinct epithelia from two different animals, the fruit fly and the quail. We first study single-junction tension on the *Drosophila* notum, showing that force inference correlates fairly well with the recoil velocity of vertices following junctional laser cuts. We next turn to the *Drosophila* retinal ommatidia and show that force inference adequately predicts tension patterns in these stereotyped groups of cells, in both wild type and mutant conditions. Finally, we show that force inference can predict complex tissue-scale stress patterns with unprecedented precision in the wild type and mutant *Drosophila* germband and the quail early embryo. Altogether, our cross-validation study on different tissues demonstrates that force inference can be confidently used in 2D to assess the mechanical state of a variety of epithelial tissues. As accuracy increases with the level of coarse-graining, we believe it is particularly well suited to determine complex stress patterns at the tissue scale during morphogenesis.

## 4.1 Single junction tensions in the *Drosophila* notum

The most straightforward experimental verification of force inference accuracy directly compares tensions inferred in single junctions to measurements obtained from single junction laser ablation, which is the most common experimental technique to evaluate junction tensions. In laser ablation experiments, a tightly focused laser disrupts the molecular structures that support tension in a targeted junction. Upon release, tension is only balanced by fluid friction so that the opening velocity following ablation is proportional to tension (M. Rauzi & Lenne, 2015). Providing that friction is the same among cuts, ablation thus provides relative estimates of tension. To compare force inference to laser ablation in single junctions, we used a rather regularly organized epithelium, the pupal notum of *Drosophila*, around 21h after pupa formation (Fig. 4.1A). Tension variations at this stage are not expected to be particularly oriented, as revealed by annular laser cuts (I. Bonnet et al., 2012). Hence they are essentially random fluctuations that cause the system to slightly deviate from a regular hexagonal array. Because force inference provides relative estimates, it is always delicate to compare tensions estimated from separate images. We thus hypothesized that the average tension was always the same in all of our images (normalized to 1). To moderate the influence of this assumption, for each field of view where force inference was performed, we did several (3 to 5) laser cuts, sufficiently spaced so as not to influence each other (Fig. 4.1A 4.1B A.2). Force inference was computed in an image taken prior to the laser cuts. We compared the inferred tensions to the initial recoil velocities of the cut junctions, measured by fitting the onset of the opening (Fig. 4.1C). We found a fairly good correlation coefficient of about 0.6 between opening velocities and inferred tensions (Fig. 4.1D). The discrepancy can arise from numerous sources: the intrinsic hypotheses of force inference, but also the errors made on velocity measurements, and the assumptions that tension is solely balanced by pure fluid friction and that fluid friction is homogeneous in the tissue. The correlation found despite these limiting factors suggests that both methods can provide reliable results. Of note, the ratios between the

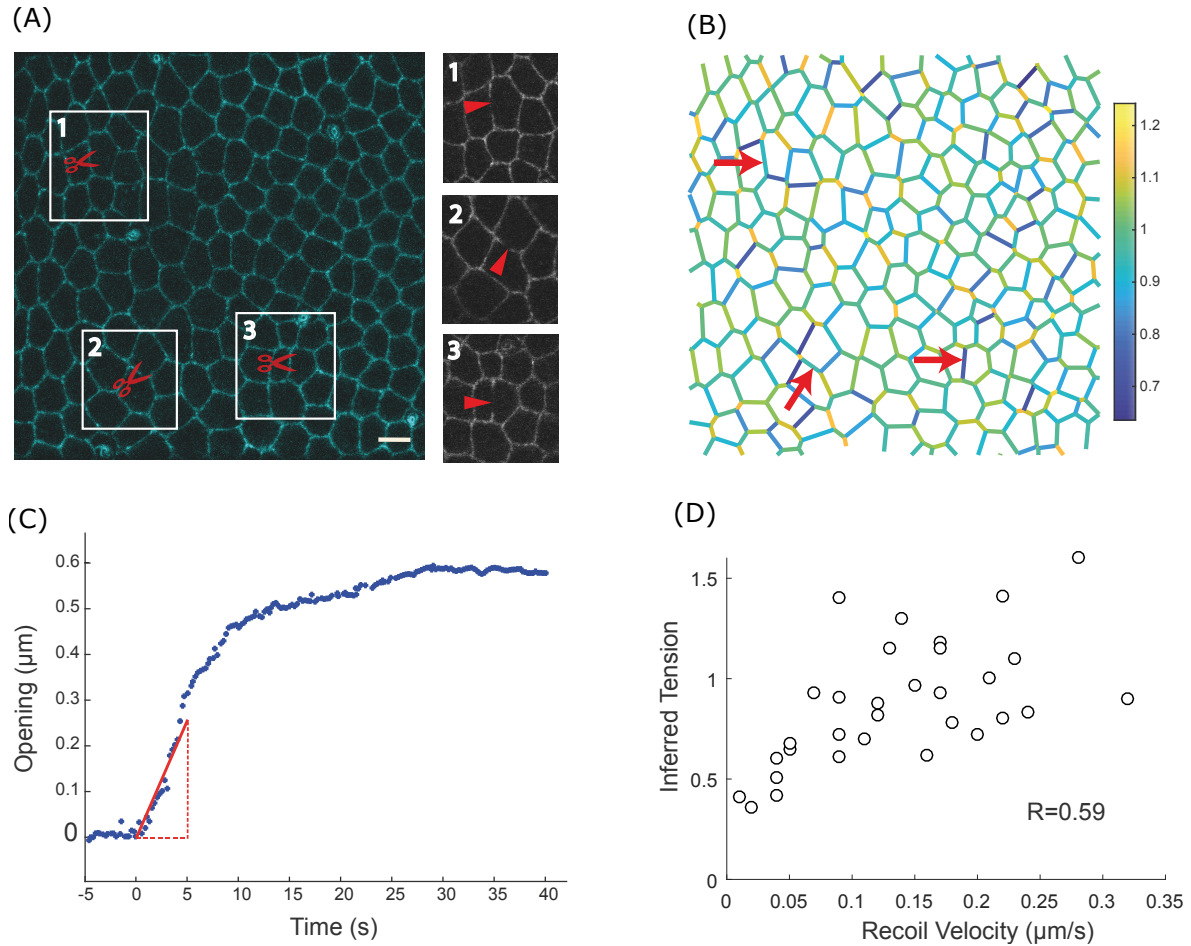


**Figure 4.1: Force inference at the single junction scale in the *Drosophila notum*.** (A) Subregion of the *Drosophila notum* 21 h after pupa formation. Scissors show ablation spots where recoil velocities will be measured. Insets show post-ablation snapshots of the considered junctions. Scale bar:  $5 \mu m$ . (B) Inferred tension map of the tissue region in (A) before the ablations. Red arrows indicate the location of ablations, where inferred tensions are extracted and compared to experimental recoil velocities. (C) Opening dynamics and initial recoil velocity. The red line shows a linear fit of the first 5 seconds, which is used to determine the initial recoil velocity. (D) Inferred tension vs. opening velocity ( $N = 31$  laser cuts from 10 pupae). Pearson's correlation coefficient is 0.59. Spearman's correlation coefficient is 0.63.



recoil velocities are not the same as the ratios between inferred tensions. This is not the case in simulations, which suggests that the error might arise from laser ablation experiments. Besides experimental noise, this might result from systematic nonlinear friction effects (friction force not simply proportional to velocity, so that the recoil velocity is not simply proportional to tension). In addition, since recoil velocities are estimated from a linear fit at the onset of the opening, an error is clearly made by approximating relaxation by a linear fit. The error made actually depends on the relaxation timescale and thus on tension, which could also be a systematic source of error.

## 4.2 Tension patterns in wild type and mutant *Drosophila* ommatidia

Stereotyped patterns of differential tension between subgroups of cells can drive the robust geometric organization of multicellular structures. We wanted to assess whether force inference could detect such patterns of tensions. To achieve this, we turned to the retina of *Drosophila*, composed of highly stereotyped groups of cells called ommatidia (Fig.4.2A). Previous studies showed that cone cell shapes and arrangement in ommatidia are determined by stereotyped differential tensions (Hayashi & Carthew, 2004) (E. H. Chan et al., 2017; Käfer et al., 2007). These tensions were shown to be determined by the amounts of Myo-II and E- and N-cadherins recruited at the considered junctions (E. H. Chan et al., 2017). These amounts were in turn shown to be determined by the "identity" of junctions, that is, by the types of cadherins expressed in the two contacting cells (E. H. Chan et al., 2017). Based on these previous results, we categorized junctions according to the cadherins expressed in the contacting cells. EN|EN junctions correspond to homotypic junctions separating two cells that both express E- and N-Cadherin. E|E junctions correspond to homotypic junctions separating two cells that both express E-Cadherin only. EN|E junctions correspond to heterotypic junctions separating a cell expressing E-Cadherin only from a cell expressing both E and N-Cadherin. These three types of

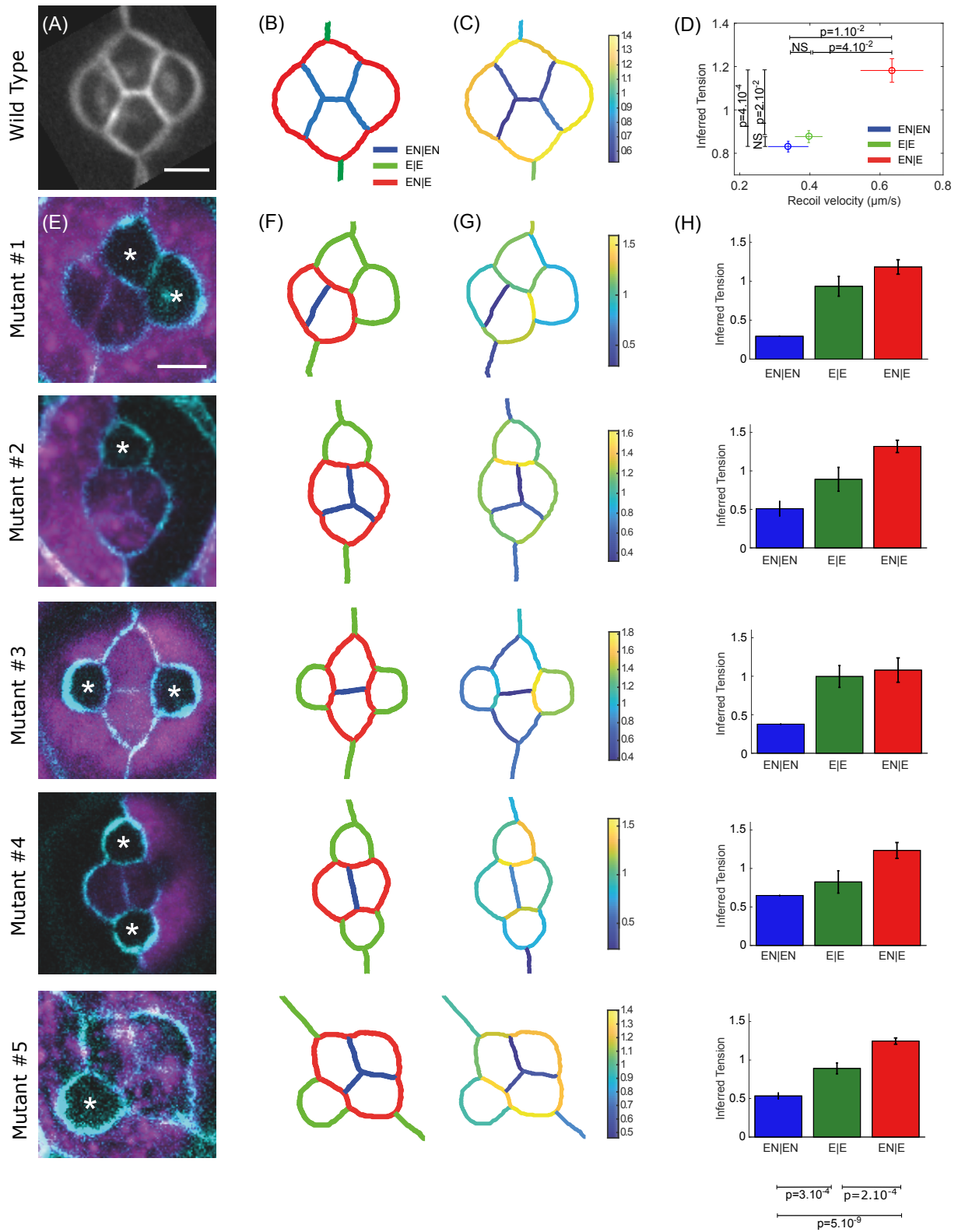


Figure 4.2: Force inference in the *Drosophila* retina. (A) The four cone cells of

a WT ommatidium. The image results from an average over  $N = 51$  ommatidia. Scale bar:  $5\mu m$ . (B) Segmented version of (A), and nomenclature of the junction types: EN|EN junctions in blue, E|E in green, and EN|E in red. (C) Map of inferred tensions. (D) Mean inferred tension vs. mean recoil velocity for each junction type (EN|EN:  $N = 19$ , E|E:  $N = 16$ , EN|E:  $N = 22$ ). (E) Five different mutant configurations generated from the mosaic experiments. WT cells are in purple. Starred cells do not express N-Cad. This only affects cone cells, as surrounding cells do not express N-Cad. Scale bar:  $5\mu m$ . (F) Pattern of junction types for each configuration. (G) Map of inferred tension in a single ommatidium for each configuration. (H) Average inferred tension for each junction type in each configuration (statistical tests at the bottom pull the five mutant configurations together).

junctions coexist in a wild type ommatidium (Fig.4.2B). We computed the averaged opening dynamics following laser cuts for each type of junctions, and extracted the corresponding initial recoil velocity (Fig.A.3). As previously demonstrated (E. H. Chan et al., 2017), this revealed a gradation of tensions according to junction type. Homotypic EN|EN junctions have the lowest tensions, E|E junctions have intermediate tensions, and heterotypic EN|E junctions have the highest tensions (Fig. 4.2D). Note that tensions are directly related to the amounts of Myo-II present at these junctions (E. H. Chan et al., 2017). To perform force inference in this system, we averaged the geometry of  $N = 51$  ommatidia, and segmented the resulting image (Fig.4.2C). As stated earlier, high and stereotyped curvatures in this system make it possible to properly measure the tangents and radii of curvature required for Laplace inference. We found that Laplace inference accurately predicts the pattern of tensions and its gradation among the three types of junctions (Fig.4.2D). Note that the cell pressures can also be computed. As expected from the Young-Laplace law, the pressure is higher in cone cells than in the surrounding cells (Fig.A.4A). We then turned to the analysis of mosaic experiments in which a fraction of cells do not express N-Cadherin (E. H. Chan et al., 2017).

Since the mutation affects random cells in the tissue, such experiments generate a variety of configurations, in which one or more cone cells are affected by the mutation (Fig.4.2). Interestingly, this modifies the pattern of junction types in the ommatidia since junction type is determined by which cadherins are expressed by the contacting cells (Fig.4.2F). To test whether force inference could still detect tension gradation in these modified conditions, we applied force inference to 5 different configurations of ommatidia (Fig.4.2G). Note that, due to the stochastic generation of these configurations, inference is performed on a single ommatidium for each configuration, whereas an average over many ommatidia was used for the wild type condition. Strikingly, the gradation of tensions identified in the wild type condition is systematically detected by force inference in the various mutant configurations (Fig.4.2H). This suggests that tensions are indeed determined by the combination of cadherins expressed by adjacent cells, through adhesion strength but also Myo-II level (E. H. Chan et al., 2017). Inference results are also consistent with laser cuts averaged over all mutant configurations for each junction type (Fig. A.4B). Overall, the results obtained in the retina suggest that force inference can robustly detect tension patterns in stereotyped units of a few cells. This led us to investigate the ability of this technique to detect stress patterns at the scale of the tissue, relevant to many morphogenetic processes.

### 4.3 Stress pattern in the avian embryo

Force inference, by coarse graining tensions and pressures at the appropriate scale, can be used to build a map of the stress tensor (Batchelor, 1970; S. Ishihara & Sugimura, 2012). Very promising results were obtained using this approach to determine the complex stress pattern of the entire *Drosophila notum* (Guirao et al., 2015). However comparison to experimental stress measurements was only performed at a very coarse level, looking at the overall anisotropy of the whole field of view, by binning tensions and pressures on the whole sample (S. Ishihara et al., 2013).

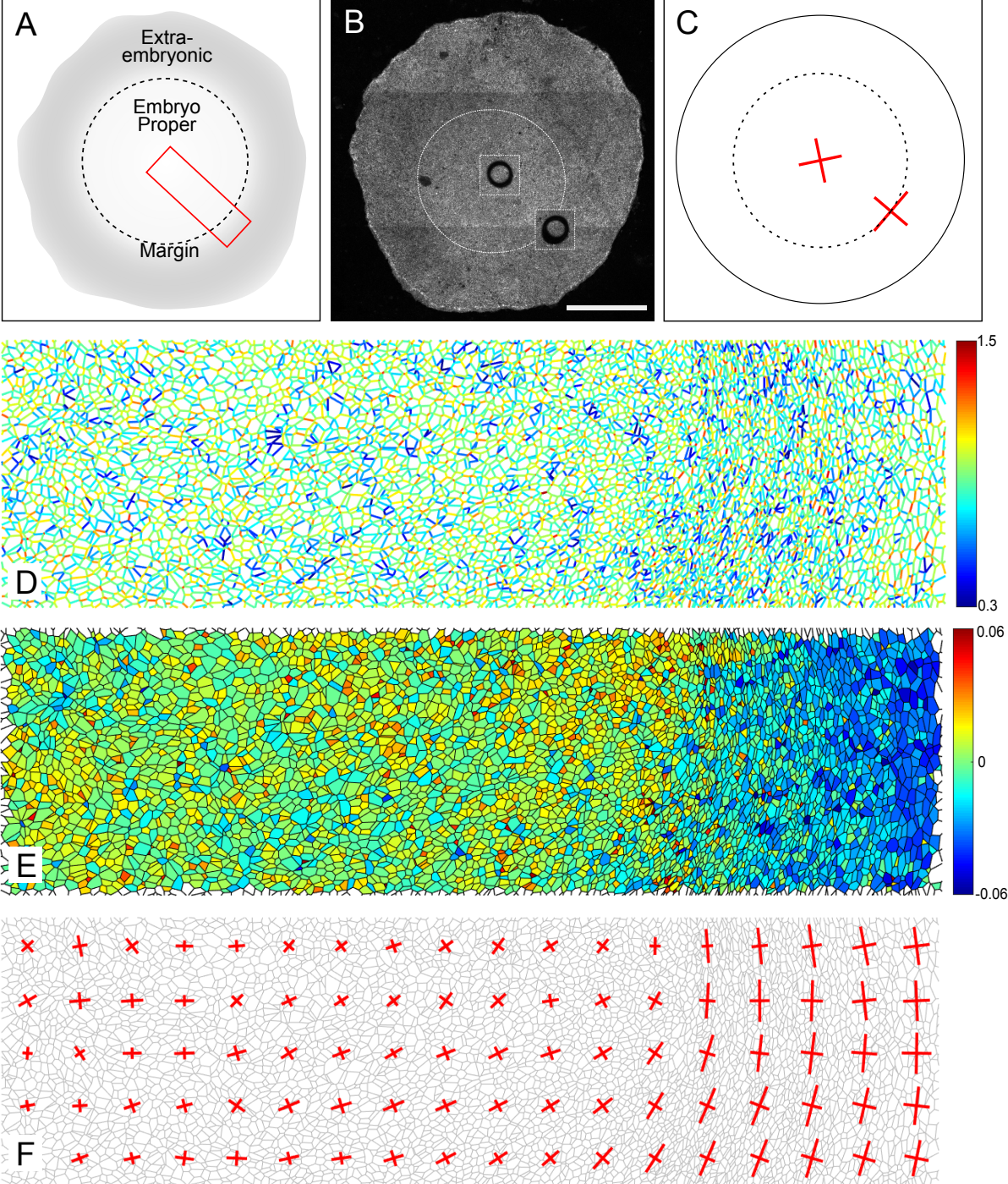


Figure 4.3: Tissue-scale force inference in the quail embryo. (A) Schematics of the

embryonic and extra-embryonic territories. The red box shows the radial region analyzed with force inference. (B) Typical regions used for ablations in the embryonic region and in the posterior margin region. Images 2 minutes after a cut are superimposed on the original image. Scale bar: 1 mm (C) Strain measured in the embryonic and margin regions 2 minutes after the cut ( $N = 7$  from 4 embryos). Red crosses show the principal directions and amplitudes of tissue strain measured 2 minutes after the cuts. (D) Map of inferred tensions. (E) Map of inferred pressures. (F) Map of inferred stress. Red crosses show the principal directions and amplitudes of the stress tensor.

To investigate the ability of force inference to detect complex stress patterns at large scales, we first turned to the gastrulating avian embryo, using the quail as a model system (Fig.4.3A). Although *Drosophila* is the most common model animal to study epithelial mechanics and epithelial morphogenesis, there is no reason that force inference general principles should not apply to other animals. At this early stage, the quail primitive ectoderm is essentially flat with about 105 cells. Previous studies carried out in chicken and quail during gastrulation have shown the presence of tangential Myosin cables at the margin between the embryo proper and the extra-embryonic territory, driving convergent extension of the presumptive primitive streak (Rozbicki et al., 2015; Saadaoui et al., 2018). To test our force inference in this system, we used circular laser cuts and segmentation of fixed samples stained for ZO-1 (Fig.4.3B), which labels the apical membrane, as described in (Saadaoui et al., 2018). As previously reported, the deformation following laser cuts is isotropic within the embryo proper, suggesting isotropic stress, but anisotropic at the margin. The principal direction of stress at the margin is orthoradial, that is, tangential to the margin itself (Fig.4.3C). Due to the very large number of cells in the whole embryo, we restricted force inference to a region spanning radially from the center of the embryo to the posterior margin (red box, Fig. 4.3A). We did not detect obvious patterns of junctional tension amplitude (Fig.4.3D). We then computed a coarse-grained stress tensor, obtained by binning the results of force inference over square subregions of few tens of cells (see

methods). We then plotted its principal directions and amplitudes in each subregion, which recapitulates the anisotropy gradient revealed by circular ablations (Fig.4.3F). In the embryonic territory, we find no stress anisotropy. As we get closer to the margin, stress gradually becomes anisotropic and oriented along the orthoradial direction, consistent with the outcome of circular laser cuts. Interestingly, we also observe a pressure gradient across the tissue, with higher pressures in the embryonic territory (Fig. 4.3E), which might be indicative of differences of mechanical state between the embryonic and extraembryonic territories. This last analysis confirms the ability of force inference to detect stress patterns at the scale of thousands of cells, and shows that the approach is relevant to animals other than *Drosophila*. However, due to the very large size of the system and to experimental limitations preventing from directly measuring recoil velocities (see methods), our analysis remains essentially qualitative. This prompted us to perform another set of experiments in a system amenable to more precise quantifications.

#### 4.4 Stress pattern in the wild type and mutant *Drosophila* germband

To that end, we turned to a mechanically well-characterized tissue, the embryonic germband of *Drosophila*, that is known to display stress polarity induced by Myo-II polarity, but also a stress gradient along the antero-posterior (AP) axis, due to the movement of the posterior midgut pulling on the tissue (Collinet et al., 2015; Lye et al., 2015). In the wild type germband, the polarized recruitment of Myo-II at dorso-ventral (DV) junctions is known to polarize stress and induce polarized cell intercalation. In addition, the posterior midgut, which undergoes rotation and invagination, has been shown to pull on the germband along the AP axis, inducing an additional gradient of stress along this axis (Fig.4.4A, left panel). This is illustrated by the opening velocities measured following large AP- or DV-oriented line cuts performed in the anterior, middle and posterior regions of the germband (Fig.4.4B, left panel). In the anterior region, away from the and

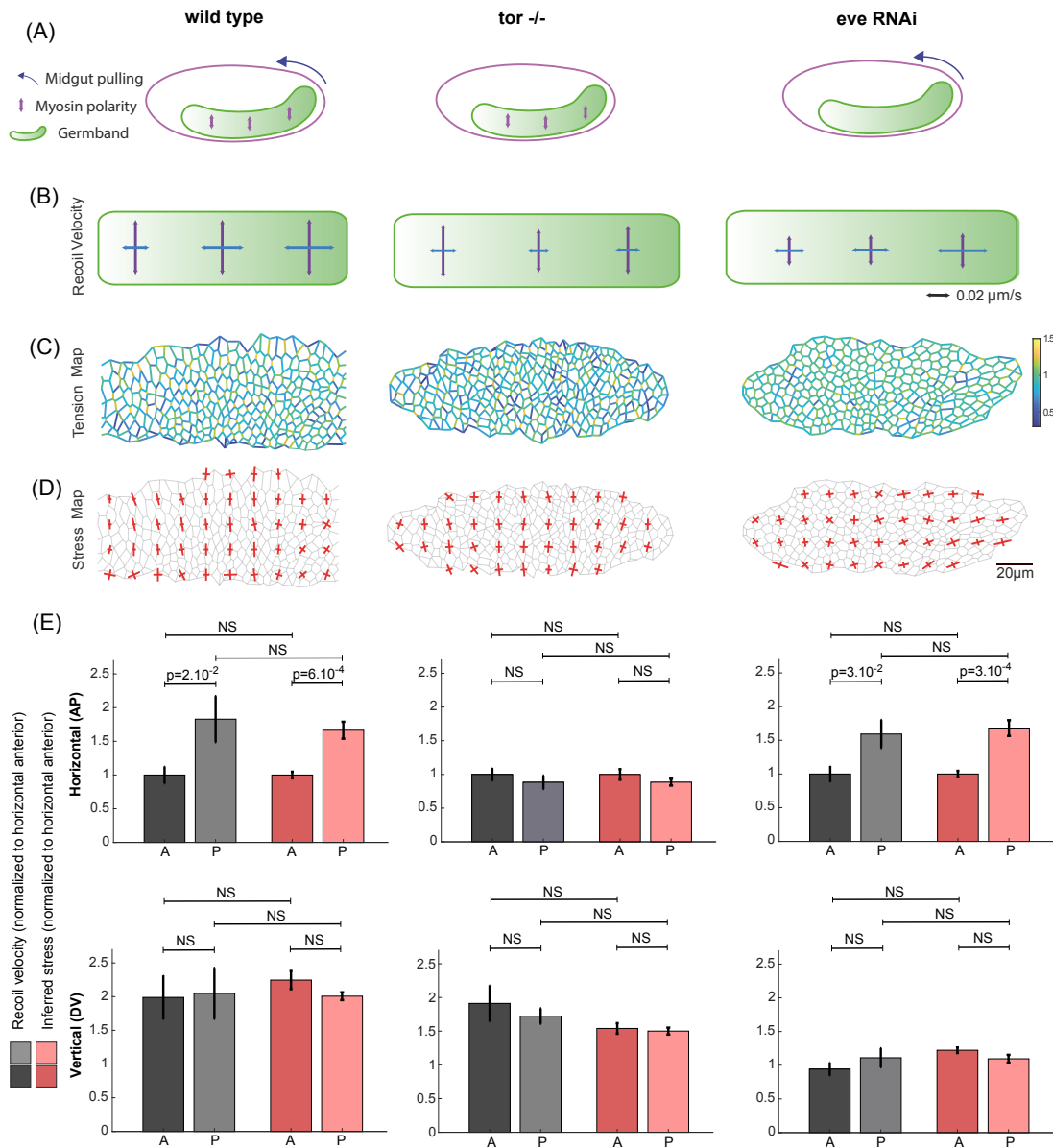


**Figure 4.4: Tissue scale force inference in the *Drosophila* germband.** (A) Scheme of stress sources in the germband. In the WT condition (left), Myo-II polarity generates stress along the DV axis, and posterior midgut invagination pulls on the germband from its posterior side. In the *Tor*<sup>-/-</sup> condition (middle), posterior midgut invagination is abolished, and Myo-II polarity is preserved. In the *Eve* RNAi condition (right), posterior midgut invagination is preserved, and Myo-II polarity is abolished. (B) Recoil velocities measured with PIV for each condition in the anterior, middle and posterior regions of the germband. Vertical arrows correspond to opening velocities along the DV axis (cuts along the AP axis), and horizontal arrows correspond to opening velocities along the AP axis (cuts along the DV axis). Each arrow results from an average over  $N = 7$  to  $N = 34$  experiments. (C) Map of inferred tension, in a representative germband for each condition. (D) Map of inferred stress. Red crosses show the principal directions



amplitudes of the stress tensor. (E) Bar plots of normalized recoil velocity and inferred stress in the horizontal direction (top row) and in the vertical direction (bottom row) for each condition. A stands for anterior, P for posterior. Anterior (resp. posterior) inferred stress is computed as an average over the three most anterior (resp. posterior) columns of (D).

posterior midgut, stress is dominated by Myo-II polarity and is strongly polarized along the DV axis. In the middle region, getting closer to the pulling posterior midgut, stress along the AP axis increases, but remains smaller than stress along the DV axis. In the posterior region, stress along the AP axis becomes even larger due to the proximity to the posterior midgut, and stress along the AP and DV axes become comparable, so that stress polarity is lost. We performed force inference on the germband during this process. First, the tension map shows that tensions are indeed higher along the DV axis than along the AP axis (Fig.4.4C, left panel), as abundantly reported in literature (Bambardekar et al., 2015; Kale et al., 2018; Rauzi et al., 2008). To obtain a better representation of polarity, we computed the stress tensor, binning over square subregions of typically 8–10 cells. We then plotted its principal directions and amplitudes in each subregion (Fig.4.4D, left panel). The results are fully consistent with the laser cut experiments. In the anterior region, stress is largely polarized along the DV axis. Getting closer to the posterior, stress along the AP axis gradually increases, so that in the posterior region, DV polarity is strongly reduced. To further quantify the stress gradients, stress polarity, and the agreement between laser cuts and stress inference, we averaged inferred AP and DV stress in the anterior and posterior regions, and directly compared them to the measured AP and DV recoil velocities in these regions (Fig. 4E, left panels). We find an excellent quantitative agreement between inference and laser cuts. Note that this is also exemplified by a plot of stress anisotropy along the AP axis (Fig.A.5). To further test force inference ability to detect stress patterns, we used mutant conditions in which posterior midgut invagination (Torso  $-/-$ ) or Myo-II polarity (Eve RNAi) are selectively impaired. In the

absence of posterior midgut invagination, posterior pulling forces are abolished (Fig.4.4A, middle panel), and the stress pattern is mostly determined by Myo-II polarity, with an important DV stress polarity from anterior to posterior (Fig.4.4B, middle panel). This is fully recapitulated by the force inference approach (Fig.4.4C–E middle panels). In contrast, in the absence of Myo-II polarization, the stress pattern is mostly determined by the posterior forces (Fig.4.4A, right panel). Laser cuts show that stress along the DV axis is reduced across all the tissue, while the gradual increase of stress along the AP axis from anterior to posterior is maintained (Fig.4.4B, right panel). The stress pattern is again fully recapitulated by the force inference approach (Fig.4.4C–E right panels). Altogether, the analyses of normal and impaired germband extension show that force inference can precisely recapitulate complex stress patterns across a dynamic epithelium undergoing morphogenetic movements. Force inference is also much faster than laser ablations, and the spatial resolution of the estimated stress is much higher.

## 4.5 Comments on Laplace force inference

As stated earlier, Laplace force inference is ideal if tangents and curvatures can be determined accurately. Unfortunately, most of the time this is not the case. Indeed, in tissues such as the notum, the germband, the quail embryo or any other similarly organized monolayer, curvatures are small. This can make tangent and curvature measurements tough because of edge pixelation. Even more so, imaging and/or segmentation limitations can result in edges in the shape of a very open S (Fig.4.5A), which not only makes tangents and curvatures difficult to assess but can also generate non-compatible angles for the two tangents at both extremities of an edge. Consequently, this inference method is very sensitive to tangent determination through fits of the edges first pixels, and to the number of pixels chosen for the fit. Using too few or too many fit pixels dramatically affects the result of Laplace force inference (Fig.4.5B). We also find that determining tangents with circle fits of the whole edge (instead of linear fits of the first few pixels) yields poor

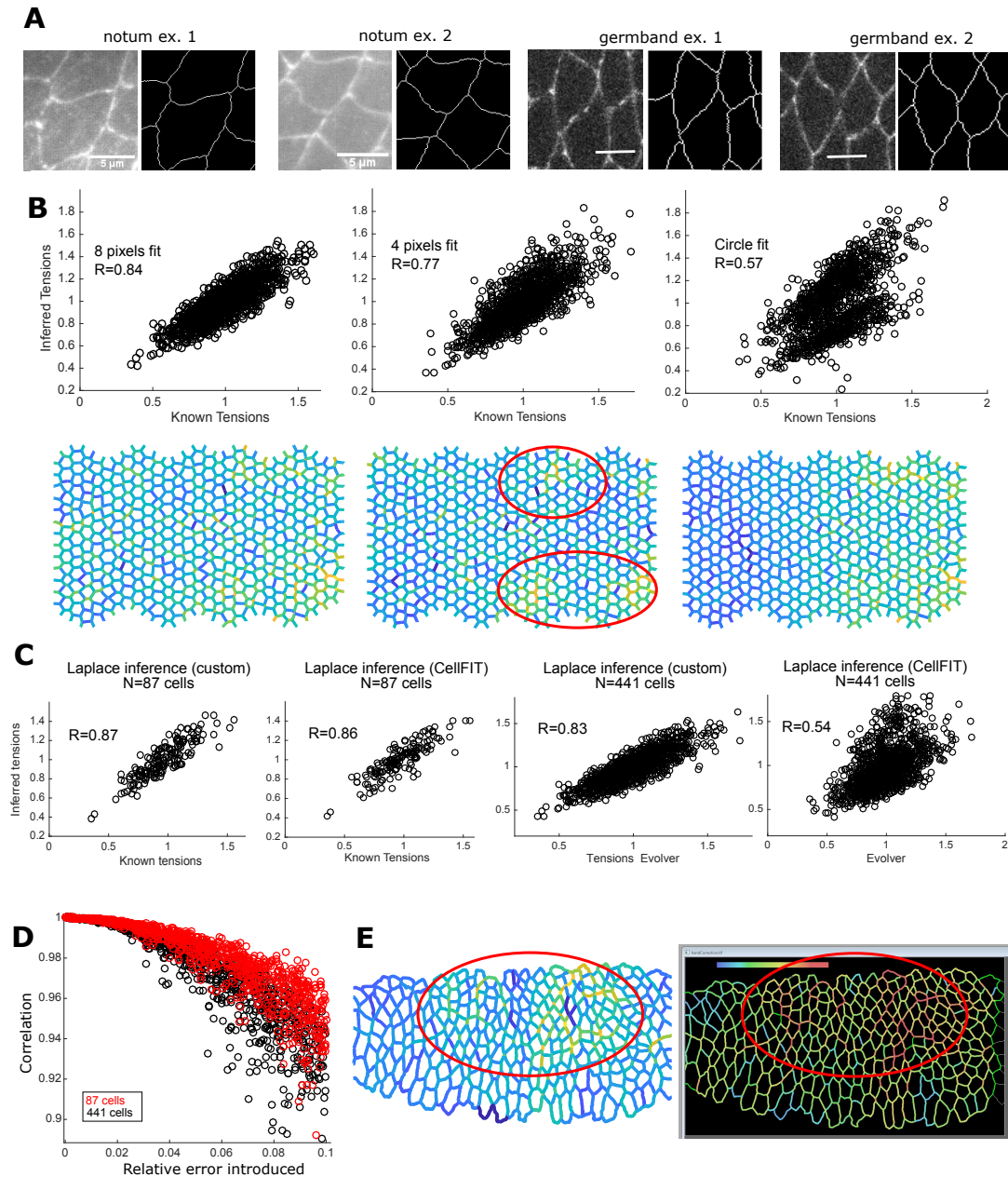


**Figure 4.5:** (A) Examples of edges with the shape of an open S. (B) Correlation plots ( $R$ =Pearson’s coefficient) and inference maps obtained with our Laplace inference implementation with 8 pixels (left), 4 pixels (middle), or circle fit (right) determination of the tangent. Red circles show the regions where errors arise. (C) Correlations obtained with Laplace inference (custom or CellFIT) for 2 tissue sizes. (D) Correlation between inference with and without introduced errors vs. relative error amplitude. Introduced errors affect only one element of the matrix in each iteration. (E) Example of error propagation in the germband of *Drosophila*, with our implementation (left) and CellFIT (right). High tension values emerge in the same regions.

results. Errors made on tangents propagate to neighboring edges when the matrix is inverted, which can lead to artefactual gradients in the inferred tension maps (Fig.4.5B). A consequence of error propagation is that larger systems are prone to more error (Fig.4.5C). This is true for our code, but even more so for CellFIT (Brodland et al., 2014). Note that we kept the resolution constant when we changed the system size (50 px/edge). To further investigate error propagation, we introduced errors in a given simulation's inference matrix. First, we computed the matrix of a simulated tissue. We introduced a random error (up to 10%) on a single non-zero projection coefficient randomly chosen in the matrix.

We then solved the inverse problem, and computed the correlation between the inferred tensions with and without error introduction. Repeating this operation hundreds of times shows that introduction of an error on projection angles rapidly affects the overall result, even more so when the system has more cells (Fig.4.5D). Finally, we provide as examples of error propagation the tension maps provided by our code and by CellFIT for a wild-type *Drosophila* germband (Fig.4.5E). Clearly, these maps have artefactual tension gradients, that are not present when we use Bayesian inference. In contrast, Laplace inference is very well suited for ommatidia, as they have high curvatures and only few cells.

## 4.6 Stress tensor based on cell shapes only

Last, we questioned whether cell shape anisotropy alone was a good indicator of stress anisotropy predicted by force inference at the tissue scale. Interestingly, an approximate stress tensor can be computed without solving the inverse problem, if one assumes that all tensions and pressures are homogeneous. This yields an approximation that is solely based on the contribution of cell shape anisotropies detected by segmentation. Indeed, junction orientations contribute to the stress tensor, with tensions being prefactors (see Batchelor's formula in the methods). Thus, the anisotropy of junction orientation, regardless of tensions, contributes to the anisotropy of stress. Similarly, gradients of junction

length will contribute to gradients of stress magnitude. This simplified analysis actually provides a good approximation of the stress obtained by force inference at the tissue scale, suggesting that junction orientation statistics largely contributes to determining the stress tensor. In the *Drosophila* germband, the error is negligible in most subregions (Fig.A.6), even though junction tensions themselves are anisotropic (Fig. 4.4C). In the quail embryo, this approximation still yields good results, although the error is more important, especially close to the margin (Fig.A.7). Besides this deviation from the result obtained with force inference, an obvious drawback of this simplified approach is that it cannot detect junction tension polarity or cell pressure gradients. However, an important advantage is that it does not require to implement force inference, but only segmentation and elementary computation. It is also much faster than force inference, especially in large systems where solving the inverse problem becomes computationally demanding. Finally, the results obtained with this approach suggest that even segmentation might not be mandatory, if the cell shape anisotropies can be properly detected from appropriate spectral analysis of the tissue image. This strategy was recently used to determine stress using Fourier transforms (Durande et al., 2018). Our results suggest that it is certainly an interesting option, especially for tissues with a very large number of cells, or tissues in which segmentation is challenging due to imaging difficulties.

## 4.7 Limitation and discussion

Advantages of force inference include that it is fully non-invasive, much easier to perform than perturbative experimental measurements, and does not require assumptions on the origin of forces involved or on the tissue rheology. However, it also comes with several assumptions. First and foremost, that tissue mechanics is essentially driven by in plane tensions and pressures. Second, that tensions are positive, and constant along cell junctions. Third, that tensions equilibrate at each vertex, in other words that the magnitude of the net force at vertices (and thus of the friction force opposing movement) should

be small compared to individual junctional tensions. This assumption is experimentally verified in various epithelial tissues, the velocity of cells and vertices during development being much smaller than the recoil velocity upon junction ablation. However, it is important to say that tissues in which junctions are not tensed (wiggly junctions), tissues that significantly deviate from a 2D plane, or very dynamic tissues, should be considered more carefully. Whether force inference could confidently be used under these assumptions in classic epithelial monolayers was still unclear. Here, we conducted a thorough cross-validation in various epithelial tissues chosen from two animals, at different developmental stages, and with different geometries and dynamics. Our results demonstrate that force inference can be reliably used to analyze the mechanical state of various epithelia, from a few cells to thousands of cells. We showed that force inference allows fairly good estimates of tension at single junctions. By providing a large set of measurements from single images, force inference can therefore be an asset to search for correlations between tension and protein distribution with good statistics (Kale et al., 2018). However, we demonstrated that averaging over groups of junctions of interest, or coarse-graining tension and pressure into a binned stress tensor, significantly improved the reliability of the pattern detected. This is especially striking at the tissue scale. For the germband, a dynamic, morphogenetic tissue with a complex stress pattern, the advantages of using inference were obvious compared to laser cuts, which can be painfully long to perform as they require averaging over many animals. Inference over a single, well-segmented germband not only recapitulated the ablation findings but also allowed a more precise characterization of the stress pattern. Moreover, results obtained in the quail show that such tissue-scale analyses are robust in animals other than *Drosophila*. Taken together, our analyses of the *Drosophila* germband and of the quail embryo show that force inference is particularly well suited to determine stress patterns at the tissue scale during morphogenetic events, as previously done by Guirao and co-workers (Guirao et al., 2015). Considering that cell movements are likely to induce friction, this suggests that it remains small enough that the hypothesis of equilibrium at vertices remains valid. Force inference could also be an

asset to study stress propagation and tissue rheology during morphogenesis, as tissue- or even animal-scale stress patterns and tissue flows can be established by active forces generated locally (Dicko et al., 2017).

# Chapter 5

## Apico-basal coupling

The mechanical description of epithelial tissues is essentially 2D, while these tissues are 3D, and some morphogenetic movements such as invagination are inherently 3D and cannot be described in 2D only.

Several previous studies have investigated the ventral furrow formation process in *Drosophila* (M. A. Gelbart et al., 2012; Polyakov et al., 2014). During the ventral furrow formation, there is a first phase of elongation in which the ventral mesodermal cells undergo apical constriction and elongate along the apico-basal axis. Later, in a second phase of shortening, the elongated mesodermal cells shorten back to their original length, fully constrict their apices and invaginate internally. The apical constriction is caused by the pulsed contraction of a medio-apical actomyosin network. Previous studies have mostly focused on the entire invagination process, and here, we decided to focus on the individual pulse events rather than on the whole process. The relationship between mechanical contraction or expansion of one plane and shifts in other planes (mostly in the basal plane) is still unclear. This coupling is investigated here by 3D imaging of cells in the *Drosophila* embryo's mesoderm and germband during normal contraction/expansion events or after regulated apical ablations. While it has been demonstrated in many studies that the basal or latero-basal surface plays a key role in a variety of tissue folding processes, such as endoderm invagination in ascidians (Sherrard et al 2010), it remains



unknown whether apico-basal coupling also plays a role in these processes. Note that other mechanisms powered by actomyosin contractility have also been shown to mediate epithelial folding. During the *Drosophila* leg morphogenesis, apoptotic cells exert, through an apico-basal myosin cable, a pulling force on the apical surface of the epithelium, producing an increase in tissue tension and apical stabilization of myosin in the surrounding tissue (Monier et al., 2015). Apico-basal myosin also generates apico-basal forces when cells undergo an epithelial-mesenchymal transition. This force is an important driver of tissue folding (Gracia et al., 2019).

## 5.1 Cell volume conserved by basal changes

During mesoderm invagination, the cells contract their apical surfaces in synchrony with actomyosin pulses. The overall pulsed contraction process in the mesoderm lasts about 15 minutes. The myosin pulses are characterized in a large body of literature as a sequence of rest, assembly, and disassembly of the actomyosin network, which lasts approximately one minute (Coravos et al., 2017; Martin, 2020).

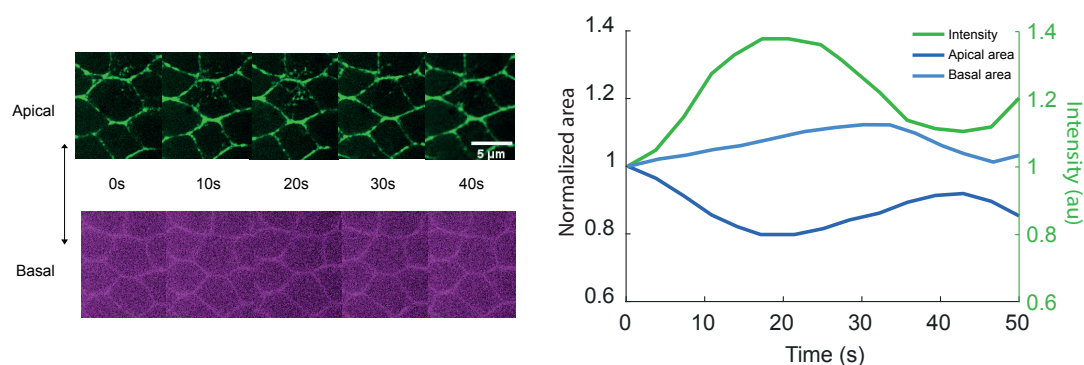


**Figure 5.1:** Left: Time-lapse of a pulsed cell. Apical surface: myosin is labeled with GFP (Top). Basal surface: Gap43 is labeled by mCherry (Bottom). Right: The plot of apical and basal area variations. In green is the apical myosin intensity variation, dark and light blue represent the apical and basal area variation, respectively.

As shown in Fig.5.1, the apical side contracts in response to the myosin pulse. When the intensity of apical myosin increases, the apical area contracts, resulting in a reduction

of area. On the other hand, the basal side (shown with Gap43 labeled with mCherry) expands. Apical and basal variations seem to be anticorrelated. The area variation is defined as the relative area variation  $(A_t + 1 - A_t)/A_t$ . To establish the relationship between basal and apical variations, we tracked the apical and basal area variations of 72 pulsed cells in 9 tissues. The area variations of pulsed cells in the basal and apical planes were measured between 30 seconds. Given that a single pulse, as shown in Fig.5.1, lasts approximately 60 seconds, the maximum area variations arise within 30 seconds. We found both positive and negative variations; positive variation indicates a cell expansion, while negative variation indicates a cell contraction. We observed contractions and expansions on both surfaces, as a cell contracts first and then expands throughout a single cycle. As shown in the Fig.5.2, the correlation coefficient indicates that these two variables are anticorrelated. Additionally, we found that the absolute apical variations always seem to be greater than the basal ones.

We found that cell volume is conserved on the minute time scale by looking at the tissue from basal to apical during the pulses. The volume is reasonably well conserved but show a slight decrease (approximately 8%). It should be noted that the volume is extrapolated using the areas of the slices. The slight decrease in volume can be explained by the fact that apical variations exceed basal variations. The few basal slices can be missed due to imaging difficulties (typically for  $1 - 3\mu m$ ). This lack of knowledge on the most basal surfaces can introduce additional errors in volume estimation. Another explanation for this volume change might be the change in cell length, as discussed in (section 6.2.1).

## 5.2 Ablation induce apical and basal variations

To further test the hypothesis that apical and basal variations are anticorrelated, we used laser ablation to trigger apical variations mechanically and observe the basal variation following the ablation. When the apical cell junction is ablated, the cell expands in the

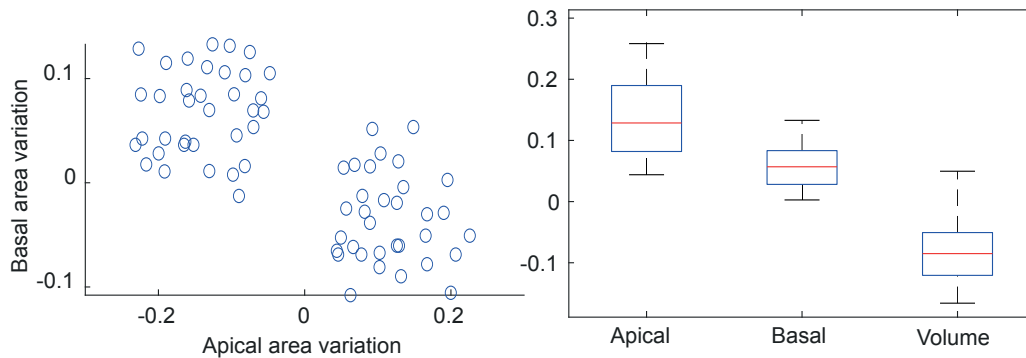


**Figure 5.2:** The apical (basal) variation ratio is the maximum ratio of the first (last) four slices' values. The Pearson correlation coefficient  $R=-0.76$ . Right: The apical and basal variation ratios are the absolute ones. The box plot red line represents the median values. The apical and basal variations are plotted with the absolute values.

apical plane, thus increasing its area. A 3D reconstruction (Fig5.3) of a cell before and after ablation illustrates that the basal contracts after ablation while the apical expands.

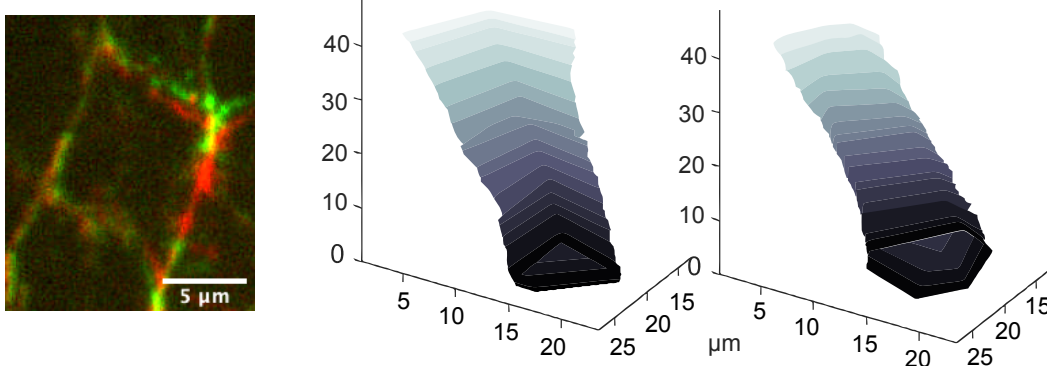


**Figure 5.3:** Ablation of a cell junction in the germband (right) The red channel is before the ablation, while the green channel is post-ablation. The image shows Myo-II labeled with mCherry. On the left panel, an example of the reconstrued cells before and after ablation.

The experiments were conducted on the mesoderm and the germband. The area variations were measured between the pre- and post-ablation. The time interval between two images corresponds to the time required for ablation, usually 30 seconds. Even if the correlation between apical and basal variations is not as significant as that previously observed with pulsing cells, with  $R=-0.55$ , it is reasonable to conclude that the ablation-

induced apical area change results in basal change. Once again, the absolute variation in the apical surface is greater than the variation in the basal surface. Surprisingly, we observed a slight increase in the cell's volume here.

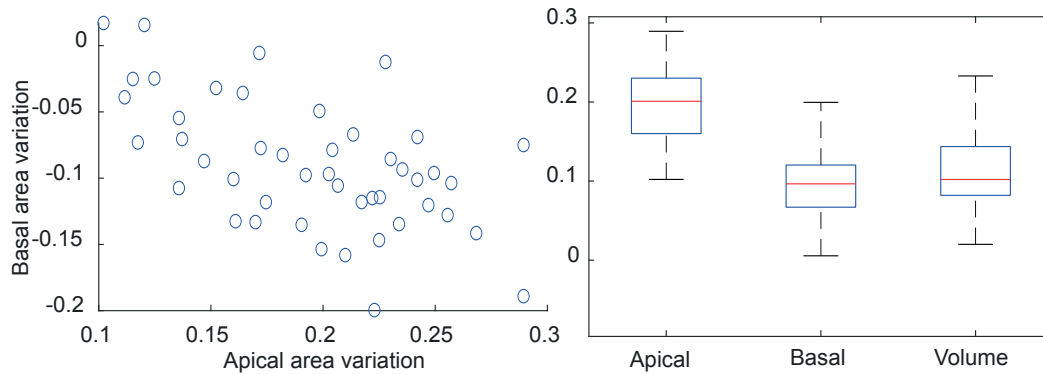


**Figure 5.4:** Left: the scatter plot of basal and apical variation ratio. The ratio is the relative variations between two time points of 30 seconds. Each point represents one experiment for a total of 46 experiments (29 on 15 germbands and 17 on five mesoderms). Right: The boxplot of apical variations and basal variations (absolute values) and volume variations.

We noticed that the ablation induced apical variations in the targeted cells but also in the surrounding cells. These variations occur either directly as a result of ablation or by the cell itself. We performed the same area variation analysis on those cells. The average area variation in the apical surfaces of these cells is smaller than that of ablated cells. The correlation between apical and basal variations is reduced compared to that for ablated cells ( $R=-0.21$ ). It should be noted that the cells do not all exhibit significant apical area variations. For example, 100 of the 231 non-ablated cells have apical variations of less than 10%. These cells are like to introduce noise in the correlation analyse between apical and basal variations. The correlation appears to be stronger for cells with larger deformation. In non-ablated cells, the absolute apical variation has a range of values comparable to the absolute basal variation.

Instead of ablating the cell junction, we can isolate a cell by ablating all the surrounding cells, resulting in a contraction of the apical area. These ablations experiments often induce an apical area variation relatively small. However, the anticorrelation between the

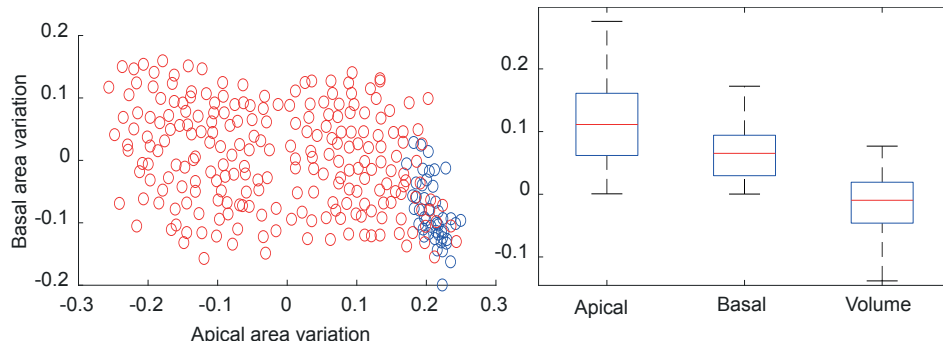


**Figure 5.5:** Left: The scatter plot of apical variations and basal variations. The blue circles represent the ablated cells, and the red circles represent non-ablated cells. Left: The boxplot of apical, basal, and volume variations for non-ablated cells. Basal variations are the absolute values.

apical and basal area variation persists for those isolated cells (Fig.A.8).

Apico-basal coupling seems to occur on both mesoderm and germband tissues, and also when cells' apical side are mechanically expanded by ablation. The correlation is stronger for pulsing and ablated cells than for the other cells (those that have not been ablated or are not pulsing). However, if we only look at cells with an apical variation greater than 10%, we find that 52% of them have an opposite basal variation. However, if we look at cells with an apical variation greater than 15%, we find that 72% of them have the opposite basal variation.

### 5.3 Quantifying cell area variation with force inference

While analyzing area variations, I noticed a correlation between area variations and cell shape, which points to a relationship between cell mechanics and cell shape. Therefore I used force inference and geometric measurements to determine and look for the correlation between several parameters, including circularity, mean tension, and anisotropy.

The circularity is defined as  $(4 * Area * \pi) / (Perimeter^2)$ . The mean tension is equal to the average tension of all junctions in that cell. As stated in chapter 3, force inference provides relative results of tension. Thus, one can only compare the tension to the area variations separately for each tissue. Correlations between circularity, mean tension, area

variations, and anisotropy were conducted on mesoderm and germband tissues (other examples see supplementary). The mean correlation values for all the 36 plots (tissue) were then computed. The mean tension appears to be higher in the circular cells. The cells with a higher mean tension (higher circularity) tend to contract rather than expand; this holds true for both the apical and basal surfaces. This suggests that the area variation is related to the intrinsic properties of the cells. Additionally, I found out that the more circular cells have a higher mean tension, but smaller area variations. The strong correlation between circularity and anisotropy indicates that circularity is indeed a good indicator of anisotropy; this is consistent with the earlier finding of the relation between cell anisotropy and tissue state (Wang et al., 2020). The tensions consistent with myosin distributions can explain the cell shape changes (Sherrard et al 2010).

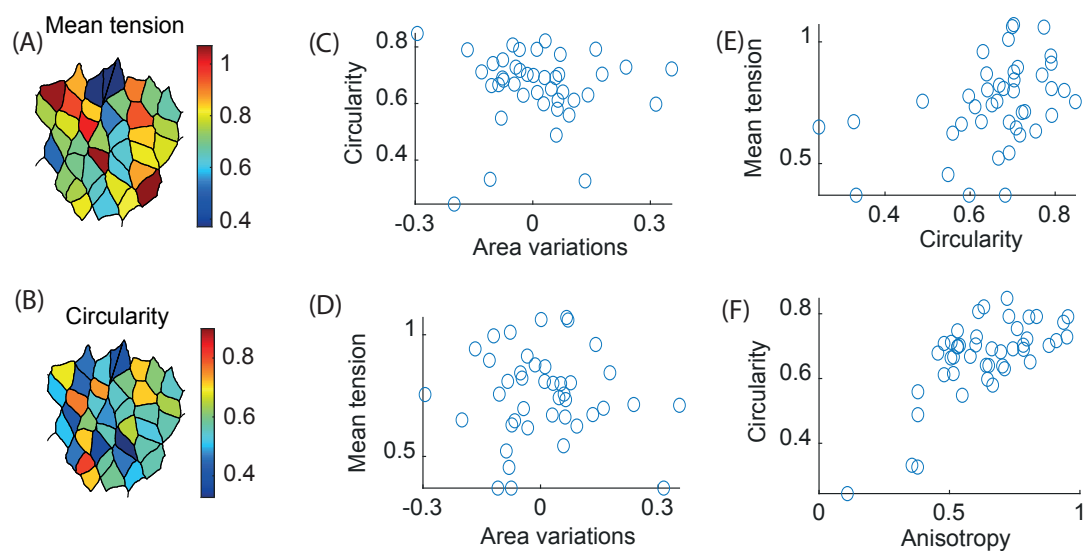


**Figure 5.6:** A. The color code indicates the circularity of each cell in this illustration of a portion of germband tissue. B. The colormap of the mean tension of the tissue, the color code shows the mean tension of all junctions for each cell. C. The scatter plot between apical area variations and circularity  $R=-0.41$ . D. Plot for area variation and mean tension  $R=-0.23$ . E. Mean tension versus circularity  $R=0.54$ . F. Anisotropy versus circularity  $R=0.78$ .

## 5.4 Propagation of the contraction

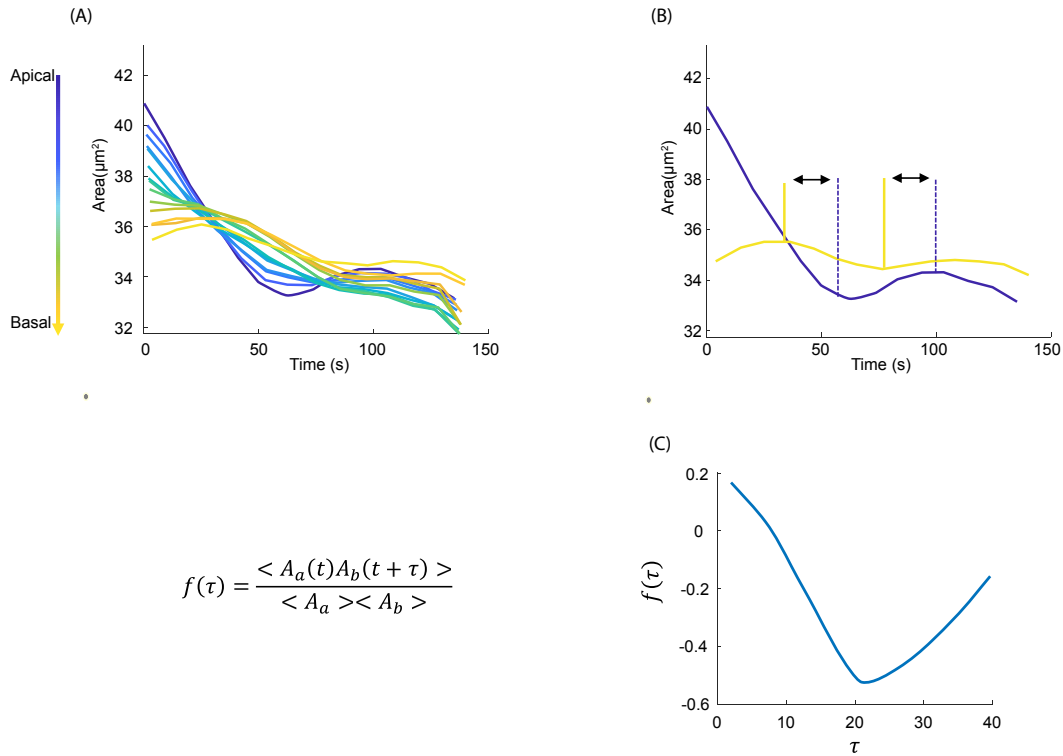


**Figure 5.7:** (A) Cell area plot over time and in space, each color represents a plane. (B) Extracted the apical and basal plane, the dash line and line indicates the local maximum or minimum. (C) The cross correlation plot calculated with the formula beside by changing  $\tau$ .

We have shown that basal variations compensate apical variations, thereby preserving cell volume on the minute scale. By closely tracking a pulsed cell in space and time, as shown in Fig.5.4, one will note that the area variation curves vary smoothly from apical to basal. This observation seems to support the idea that the apical and basal variations are coupled. However, According to Fig.5.7B, there is a delay between when the area of the apical side reaches the local minimum and when the area of the basal side reaches the local maximum. This delay can be quantified using cross-correlation function shown in (Fig.5.7). The apical and basal area variations are found to be in phase with a lag

of  $20 \pm 4s$  (with 95% confidence interval). The lag was computed as an average of 16 cells from 2 tissue (see other examples FigA.10). Since the apical and basal variations are anticorrelated, we can claim that basal variations are a consequence of apical variations, implying that they are mechanically coupled. Thus, one could argue that the delay between apical and basal variations represents the time required for apical variations to propagate.

## 5.5 Discussion

We found that changes in apical and basal area are anti-correlated during natural pulsation of cells or when cells are perturbed by laser ablation. By analysing changes in area in different planes we identified a delay between contraction/expansion in apical/basal surfaces. Given that the apical basal length of the cell is approximately  $40\mu m$ , the propagation speed is  $2\mu m/s$ . The observed speed is significantly slower than the speed of planar propagation observed when cell junctions are deflected using optical tweezers in the germband of *Drosophila* embryo (Bambardekar et al., 2015). To further confirm this propagation hypothesis, or in other words, to measure it, the ablation experiments of (section 5.2) might be an appropriate one. However, due to technical limitations, the use of ablation for this purpose can be challenging; this is discussed in detail in (section 6.2.3).



# Chapter 6

## Perspective and discussion

### 6.1 Force inference for the future?

Although force inference has now been extensively studied, numerous technical details can still be improved, and, many of which have already been highlighted by a few of those working in the field—for example, the choice of the appropriate method to use depending on the characteristics of the tissue, or even extension to 3D force inference.

#### 6.1.1 Which method to choose

We investigated force inference using two different approaches in this thesis: Laplace and Bayesian. We demonstrated that it is a powerful tool for describing tissue mechanical states at various scales. Both strategies, though, have their advantages and disadvantages. Applying one method to a situation that requires the application of the other method would result in incorrect outcomes (See annex). Roffay’s recent review discussed various methods for inferring force and proposed a flowchart depicting the various steps involved in selecting the most appropriate method for inferring force. (Fig.6.1). As suggested in our article (Kong 2019), it may be more appropriate to use the Laplace method (which they called Curved junction inference) when the general junction curvatures are properly measurable, a condition that is actually not easily met. In addition, our results suggest

that Laplace force inference propagates errors when the system becomes larger. Hence it is suited for small groups of cells rather than for large tissues with hundreds or thousands of cells. In this latter scenario, bayesian inference should be preferred.

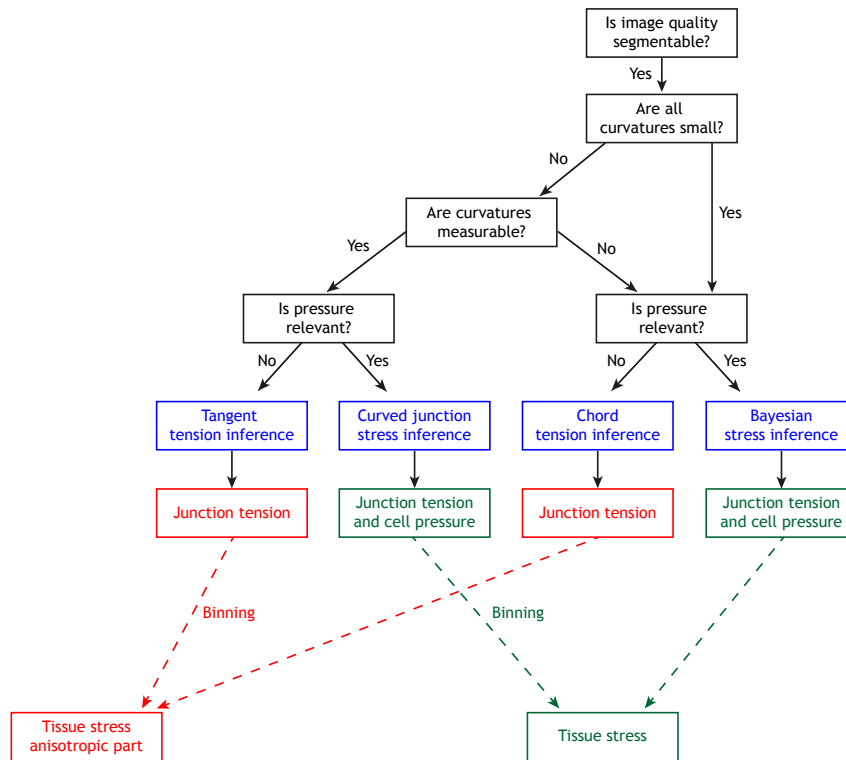


**Figure 6.1:** The flowchart for force inference decision proposed by Roffay and co-workers (C. Roffay., et al 2021)

This decision-making process can be improved to be more quantitative to increase its robustness. This may be accomplished by making a rigorous comparison of the two methods. One can simulate synthetic tissues with average curvature gradually increased, and then apply both methods to those generated tissues. Same as (Fig.3.6 3.7), correlation coefficients can be calculated between known tension (pressure) and inferred tension (pressure) for both methods. We should expect an increase in correlation as the curvature increases for Laplace inference. Then we can define a critical correlation value, at which one method should be preferred over the other.

Notably, our study made no note of the tangent tension and chord tension inferences shown in (Fig.6.1). However, they are similar to the Laplace implementation. They

are essentially the equations system that contains the tension component. Tangent force inference is identical to Laplace force inference in terms of the equations written. It's mostly the Laplace inference without the pressure part (note that tension can be computed alone in the Laplace inference). The chord tension inference is slightly different in terms of equations written; moreover, it also uses the force balance of three tensions at the vertices; the distinction is that it approximates actual junctions as straight lines between vertices. Both methods, tangent tension inference and chord tension inference yield knowledge only about the junction tension. We excluded them from the study due to a lack of information on the pressure and to noticeable curvatures in most epithelial tissues. However, if we are just interested in the tension in tissues with very low junction curvature, these methods (in particular the tangent inference) would be a rational option that often saves on computation power.

### 6.1.2 Dynamic force inference

During my study, one of the most frequent requests made by potential users of force inference was to track forces' evolution. As previously stated, force inference is currently useful for tracking stress gradients and the tissue level stress pattern. But as the method yields relative results, there is no reference pressure or tension to compare results at different time points.

To tackle this issue, Vasan and co-workers proposed a new approach, 'dynamic local intercellular tension estimation' (DLITE). In contrast to previous methods, DLITE makes an initial guess for the current time point using the tension pressure from the previous time point. Thus, DLITE may improve performance over time series. This informs the method and slightly improves its robustness against noise. However, this method is still a static method where each inversion is performed on a single image. For the first frame, the global minimum solutions were calculated using a global optimization technique called basin-hopping.

In general, temporal dynamics of cell shape or force changes can also be incorporated;

in the presence of net drag, the equation describing the equilibrium of forces becomes  $Ap = \Gamma\nu$ , where  $\nu$  is a vector of the velocity and  $\Gamma$  is a  $n * n$  dimensional representation of drag coefficients. The Bayesian formulation can be applied immediately to the adapted inverse problem by substituting  $\Gamma$  for  $b$  in Eq3.5. The right form of  $\Gamma$  in epithelial tissue has yet to be identified for unknown reasons. It has been widely accepted that the equation takes the form of  $\Gamma_{ij} = \delta_{ij}\gamma$  where  $\gamma > 0$  (Rauzi et al., 2008; Eiraku et al., 2011).

Another method that can be tested is a technique called video force microscopy (VFM), which was developed to generate dynamic force maps from live movies (Brodland et al., 2010). This approach is unique in that it considers forces to be decomposed into active and passive components. The forces that drive the system to equilibrium are produced by the passive components of cells (cytoplasm). Finite element methods can be used to calculate the forces (black arrows in Fig.6.2B) that are required, based on their viscosity and other material properties, to make them deform (Fig.6.2 from A to B). Active forces produced by the contraction of the cortical actomyosin network, cell membrane tension, cell adhesion forces, and stress fibers are thought to drive the passive components to deform. The force balance equation will then be written between the active and passive forces; the equation is equivalent to Eq 3.1, except that the force  $b$  is not equal to zero but to the passive force calculated with finite elements. As with force inference, tension and pressure can be calculated by inverting the matrix using weighted least squares techniques. At each time point, the tension pressure coefficients matrix should be rewritten to account for the current geometry. Furthermore, the system's passive force should be recalculated to ensure that it provides the forces necessary to allow the tissue to deform in order to achieve the geometry of the next time point.

This method can be useful to analyze morphogenetic movements where cells are driven out of mechanical equilibrium, preferably when images cover the entire tissue, including its boundaries; images covering only a small region of a larger epithelium are more difficult to analyze (Hutson et al., 2013). However, this method has been shown to have a high sensitivity to noise, including that produced by image segmentation (Brodland et al.,

2014).

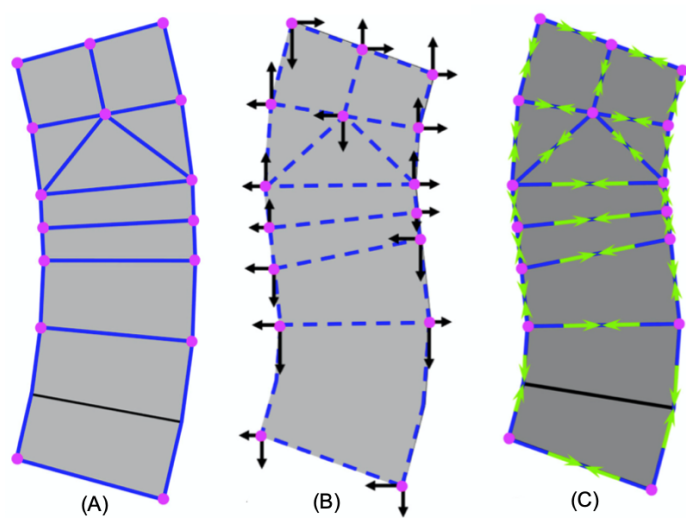


**Figure 6.2:** (A) A polygonal partitioning of the epithelium at time  $t$ . (B) At time  $t + \Delta t$ , the tissue adopted a new geometry. The forces (black arrows) were applied to deform the tissue making the changes from A to B. These forces are computed using a finite element method. (C) VFM calculates the junction tension (green arrows) and intracellular pressures that must work together to produce the forces seen in B. Adapted from (Brodland et al., 2010)

Whichever approach is desired for dynamic analysis, the following technical aspects should be considered. The time interval between consecutive time points must be adjusted accordingly. A time interval that is too long can result in the loss of temporal information regarding changes in cell structure. Simultaneously, a too-short time interval results in an inaccurate velocity estimation owing to the increased sensitivity to image processing errors. Additionally, detecting and tracking in large series of images requires a sophisticated algorithm. Furthermore, caution should be exercised during the T1 transition. Due to the quasi-static assumption, both Laplace and Bayesian methods are not appropriate for analyzing laser ablation recoil or other rapid motions where viscous forces may be significant. Note that for tissues that deform at morphogenetic time scales, our results suggest that the quasi-static approximation remains valid. Indeed, we obtained good results in the germband, a rapidly deforming tissue. However, a relative comparison of tension, pressure, or stress amplitudes at different time points is not possible without

additional assumptions or calibration measurements at each time step (laser ablation, for instance).

### 6.1.3 The correlation with junctional molecules intensity

Ishihara and colleagues show a positive correlation between the density of myosin and the inferred tension on the wing pupa disc of *Drosophila*. We attempted to compare the inferred tension with the intensity of Myo-II and E-cadherin in the form of  $aI_{myosin} - bI_{cadherin}$ , because actomyosin tends to shorten the junction and thus positively contribute to tension, while E-cadherin tends to lengthen the junction and thus negatively contributes to the tension. Surprisingly, we observed no anti-correlation between the intensity of E-cadherin and the inferred tension. We did find, however, a correlation between myosin intensity and inferred tension. This study has not been thoroughly examined. A more rigorous study is needed. To advance this study further, one may include additional molecules such as actin and other adhesion molecules. One should be excessively careful to have homogeneous illumination of the analyzed sample, which was a major concern when we tried to perform our analyses.

### 6.1.4 3D force inference

Although the applicability of 2D force inference has increased dramatically over the last decade, we expect a substantial rise in the usage of 3D force inference in the coming years, given that tissues considered as 2D are essentially 3D objects. The inference of force in 3D has already been proposed and even applied, as shown by one of the first applications on murine embryos (Veldhuis., et al 2017).

In a 3D tissue, a junction is a line where three cells meet, as opposed to a line where two cells meet in a 2D tissue (Fig.6.3). This precision of the junction determination in 3D will be determined by the resolution in Z; as we can see in (Fig.6.3) if we have three triplets (green) along the junction, we can then fit a spline to obtain the junction

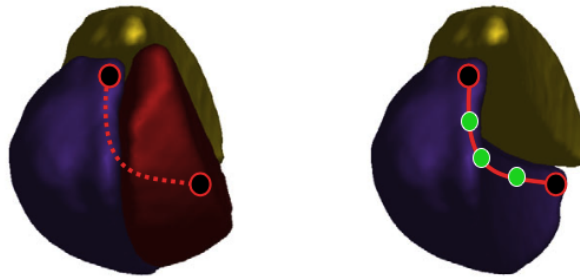


**Figure 6.3:** Three cells (left panel) share three junctions, their common junction (dotted line) and their two end vertices (open circles). To better visualize the junction, one segmented cell (red) is removed (middle panel). To measure junction angles, the image is rotated (right panel) and visualizes the 2D section perpendicular to the junction; both vertices are approximately projected on top of each other, the green dot represents triplets of the junction in the imaging plane. Adapted from (C. Roffay., et al 2021).

arc. A junction equilibrium is expressed by Eqn 1 written in any plane perpendicularly intersecting this junction (Fig.6.4). Under the hypothesis that all points along the junction are in mechanical equilibrium, the angles used in Eq3.1 can be measured at any of these points or better by averaging several measurements along the same junction.

With the advance in technology to better quantify cell curvatures in 3D, force inference could become readily accessible in a large range of tissues. The increase of images means an increase in segmentation and more data manipulation. Even though a novel method for segmenting images and inferring force simultaneously has been proposed (Noll 2020), segmentation can be difficult if the image quality is poor. Furthermore, segmenting all the cell contours in 3D will be extremely difficult. Hence, spline fits (Fig.6.4) are important for 3D force inference, which may introduce a large number of errors.

Cross validations of 3D force inference with experiments remain sparse and may require the use of force sensors such as liquid droplets for cell-level measurements (Campàs et al., 2014) and deformable gel beads for absolute measurements of tissue stress (Dolega et al., 2017; Mohagheghian et al., 2018; Lee et al., 2019; Träber et al., 2019). The comparison of 3D force inference with membrane tension sensors (Colom et al., 2018; Li et al., 2018) can open up new avenues for research into the contribution of the cell membrane to cell

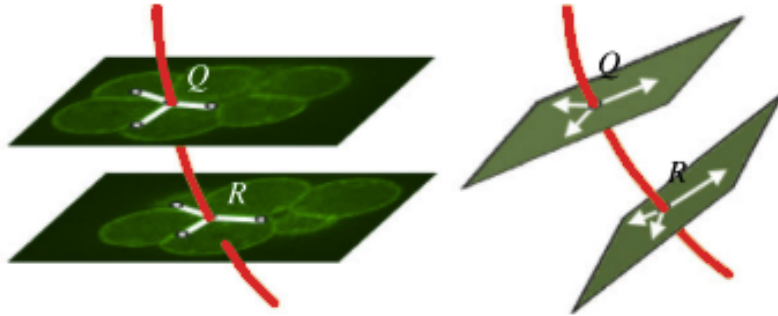


**Figure 6.4:** To convert the in-plane angles defined by these graphic triplets to true dihedral angles, splines (shown as orange curves) were constructed through sets of grouped triplets. Adapted from (Veldhuis., et al 2017)).

junction tensions.

Finally, segmentation-free methods such as those based on Fourier transform (Durande et al., 2019) could easily be extended to three dimensions to extract coarse-grained cell shape anisotropy and hence 3D tissue stress information (see our analysis of the stress tensor based on cell shapes only, section 4.6).

## 6.2 Apical basal coupling

### 6.2.1 The height changes

Without conclusively establishing that the height does not change, it is difficult to make definitive conclusions on the apical-basal coupling. According to the lengthening rate discovered during mesoderm invagination, the change in height at the minute scale must be less significant than the changes on the apical or basal side (M. Gelbart., et al 2012). Therefore, by incorporating the length analysis, we would gain a deeper understanding of volume conservation. The cause of the small volume change in both pulsed mesoderm cells and ablated cells could be identified. Additionally, we would determine whether the apical basal coupling is linked to cell lengthening. To overcome the issue of low basal intensity, a microscope other than a confocal might be required, for example, a two-photon



microscope.

### 6.2.2 Molecular contribution to the coupling

To have a better understanding of the apical-basal coupling, the molecular elements of the system must be considered. We already know the apical constriction is caused by pulsed myosin (Martin et al., 2009). Basal Myo-II inhibition is also necessary to complete the invagination (Krueger et al., 2018). Apart from apical constriction, no active force is needed to initiate the invagination phase (Krueger et al., 2018). Additionally, it is worthwhile to analyze the fold of myosin changes on both sides to determine whether any relations exist, whether apical-basal myosin variations resemble apical-basal area changes, and whether they precede or follow them. Indeed, it has been shown that a local decrease in basal tension leads to the formation of two neighboring folds in the imaginal discs of the developing *Drosophila* wings (Sui et al., 2018). The curling of the MDCK cell monolayer is due to an enrichment of myosin in the basal domain, resulting in the formation of a curvature where the apical and basal surfaces vary differently. All of these show how critical basal myosin may be. Additionally, mutants such as Twist and Snail can be used to test further the propagation. In contrast to wild-type, ventral cells, in which myosin was concentrated on the apical cortex twist and snail mutants accumulated myosin predominantly at cell junctions (Martin et al., 2009).

### 6.2.3 To measure the propagation

We discovered that the apical and basal changes are delayed by 20s in pulsed cells; this delay could be due to the mechanical effect of the apical changes. To further validate this theory, we may use ablation to test this propagation hypothesis. If we induce apical area changes with ablation in the apical and then follow up with the changes in the basal, we would expect to find that the basal initially does not change, but after a period of time, it starts to contract in response to apical changes. However, our ablation device as

it is does not allow simultaneous imaging and ablation. The ablation procedure usually requires about 30 seconds. As a consequence, there is a 30-second delay between the first and second stacks (Fig.6.5). Within 30 seconds, we can see that the basal side has already begun to contract after the apical ablation (Fig.6.5). To capture the basal delay, the time resolution of the ablation experiments needs to be improved. This will require technical improvements, such as reconfiguring the setup to allow simultaneously imaging and laser ablation.

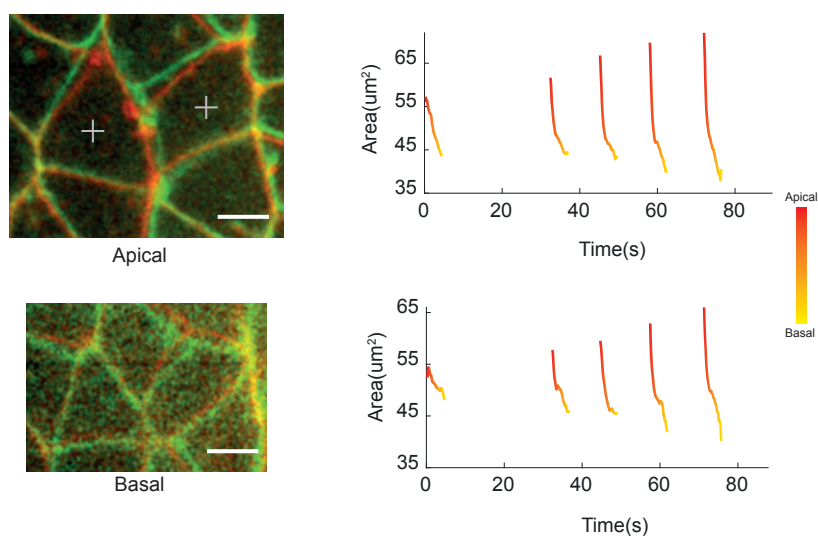


**Figure 6.5:** Laser ablation induces apical expansion and basal contraction. Left panel: images of Gap43:mCherry. The red channel represents prior ablation, and the green channel represents post-ablation. Right panel: Area plot of both cells. The color code indicates the Z position; red indicates the apical position, and yellow indicates the basal position. Scale-bar:  $5\mu m$

# Appendix A

## Appendix figures

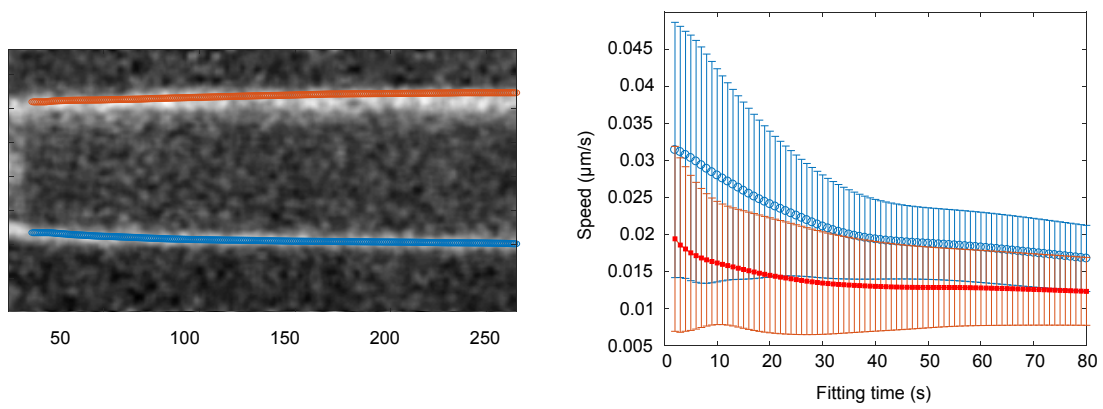
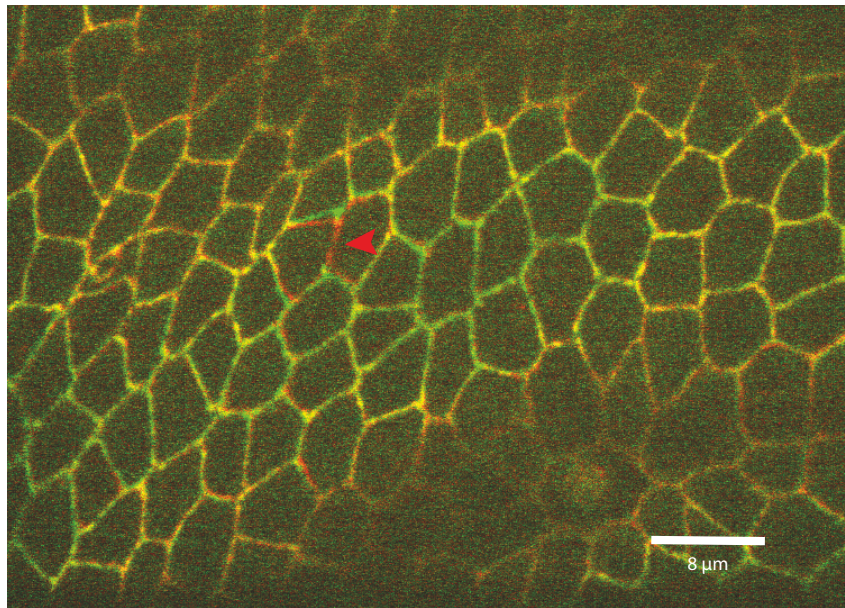


**Figure A.1: Recoil speed estimation depends on fitting time** On the left is an illustration of kymograph tracking. Right: the estimated speed plotted against various fitting time intervals.



Pre-ablation

Post-ablation

**Figure A.2: Impact of point ablation on surrounding tissue geometry** Overlay of the tissue geometry prior (red) and after (green) cutting a single junction (marked by an arrowhead). The displacement in the surrounding cells decays rapidly, and is hardly noticeable above a one-cell distance.

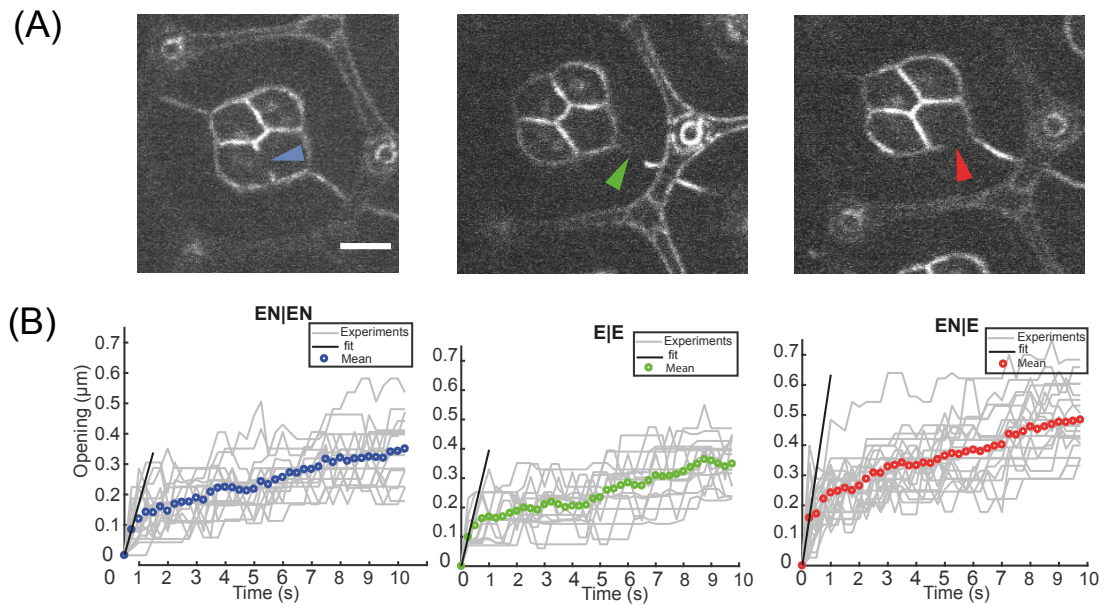


**Figure A.3: Ablations in the ommatidia** Ablations in the ommatidia Time (s)  
 Time (s) (A) Snapshots of ablation experiments performed for each type of junction. Scale-bar:  $5\mu m$  (B) Averaged opening dynamics for each type of junction (EN|EN: N=19, E|E: N=16, EN|E: N=22). Individual opening curves are shown in light gray.

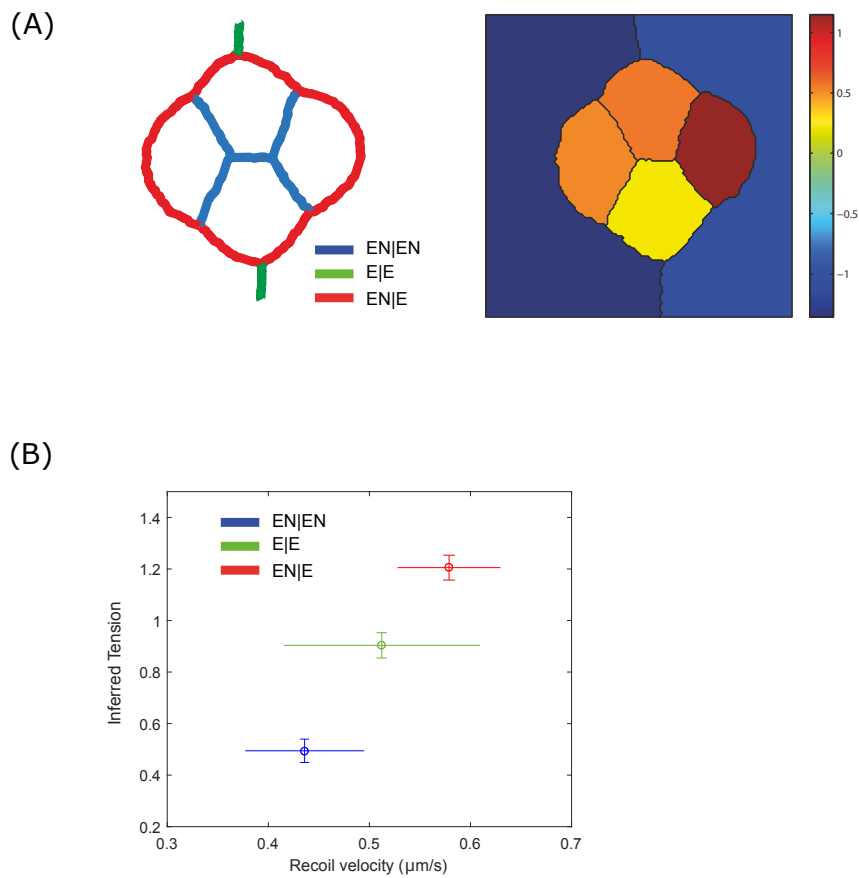


**Figure A.4:** (A) Left: Junction types. Right: Pressure map obtained using Laplace force inference in the averaged WT ommatidium. (B) Inferred tensions vs. recoil velocity averaged over all 5 mutant configurations ( $N=5$ ).

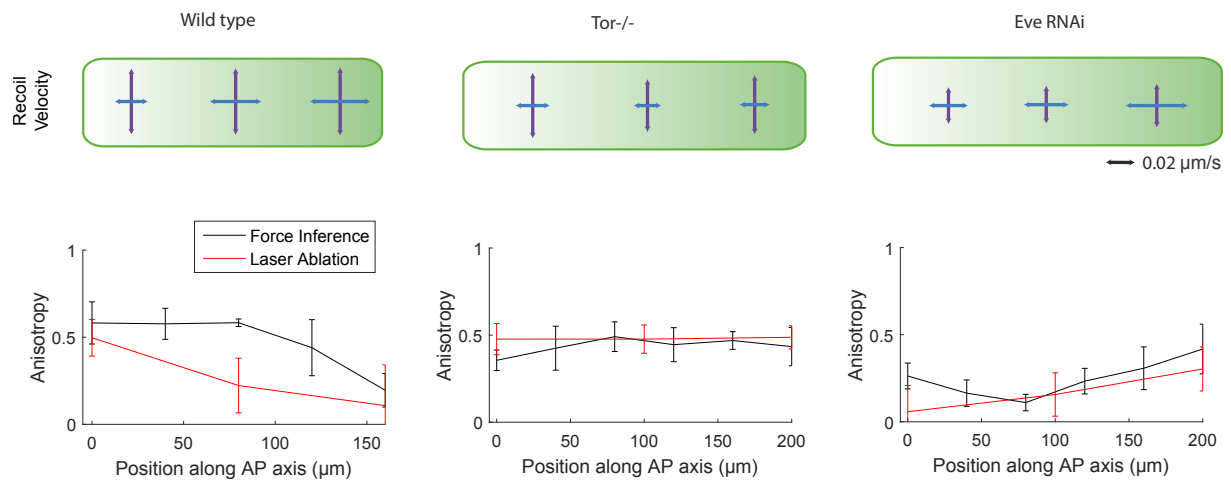


**Figure A.5: Stress anisotropy along the AP axis** Top : Horizontal and vertical recoil velocities measured by laser ablation in different conditions. Bottom : Anisotropy along the AP axis measured by force inference or laser ablation in different conditions. Anisotropy is defined as  $A=1-m/M$ , where  $M$  is the amplitude in the principal direction, and  $m$  the amplitude in the other direction.



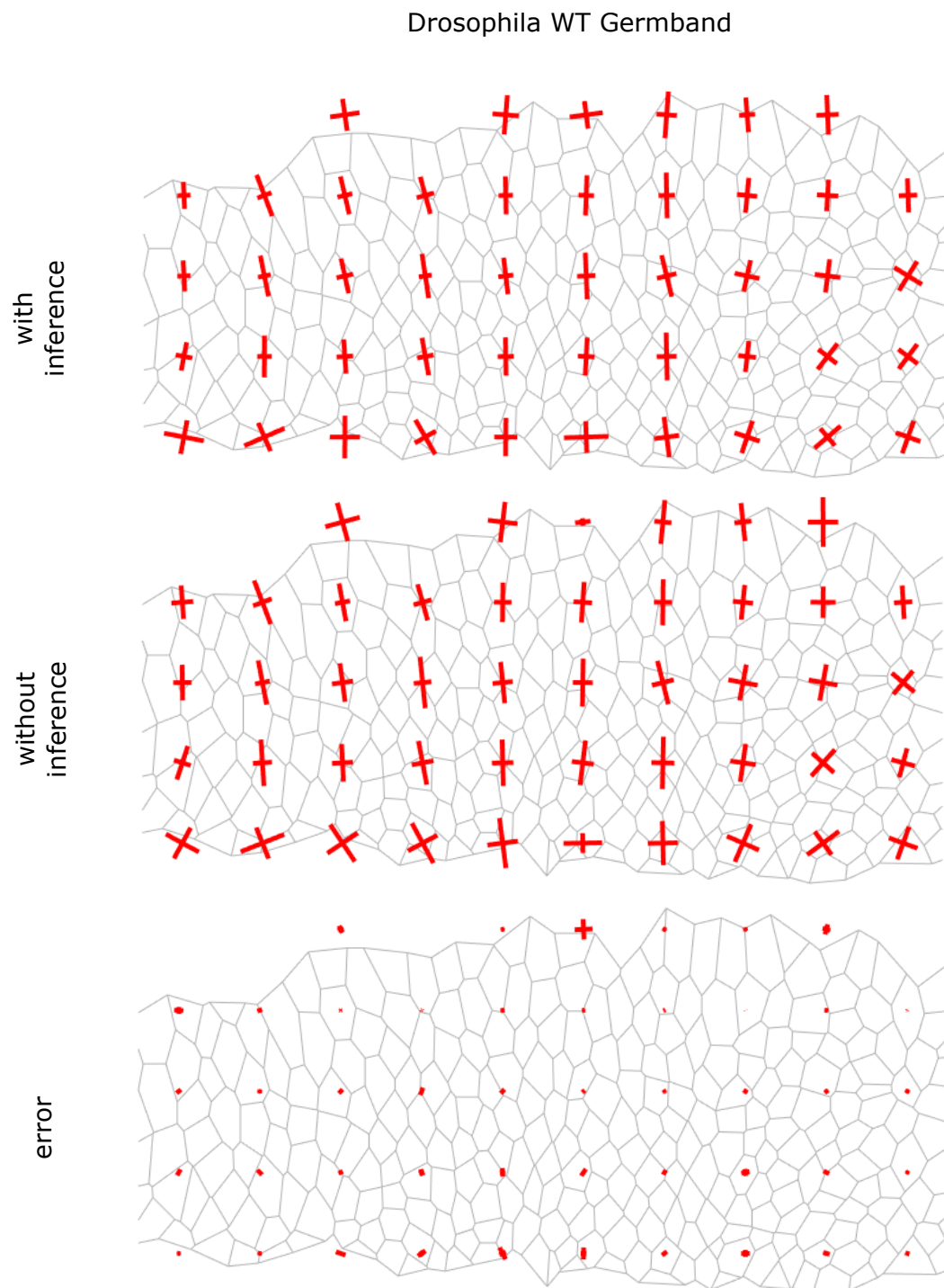


**Figure A.6: Stress estimates from cell shapes only in the WT germband** Stress estimates from cell shapes only in the WT germband Top - Stress computed using Batchelor formula and the results of force inference Middle - Stress computed using Batchelor formula assuming that tensions and pressures are homogeneous Bottom - Error (top minus middle)

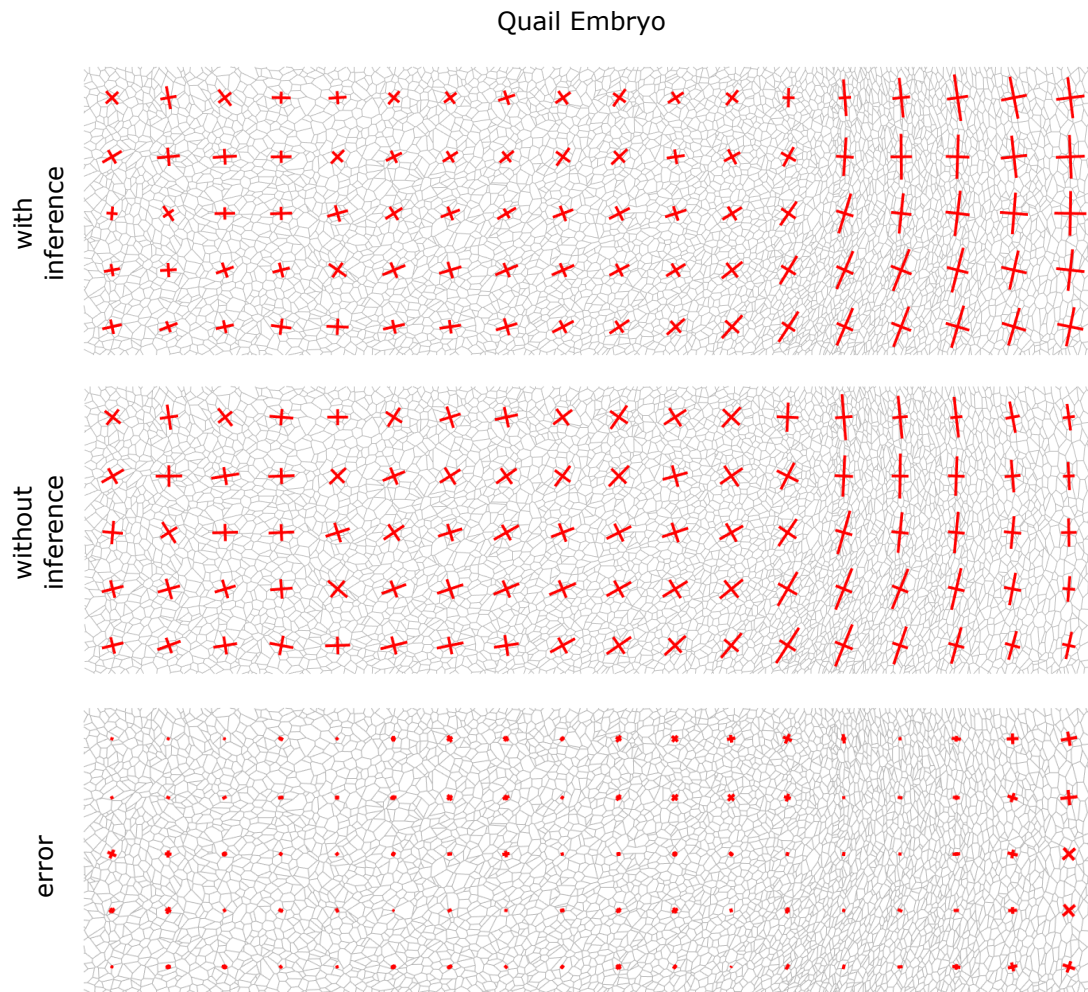


**Figure A.7: Stress estimates from cell shapes only in the quail embryo** Top - Stress computed using Batchelor formula and the results of force inference Middle - Stress computed using Batchelor formula assuming that tensions and pressures are homogeneous Bottom - Error (top minus middle)

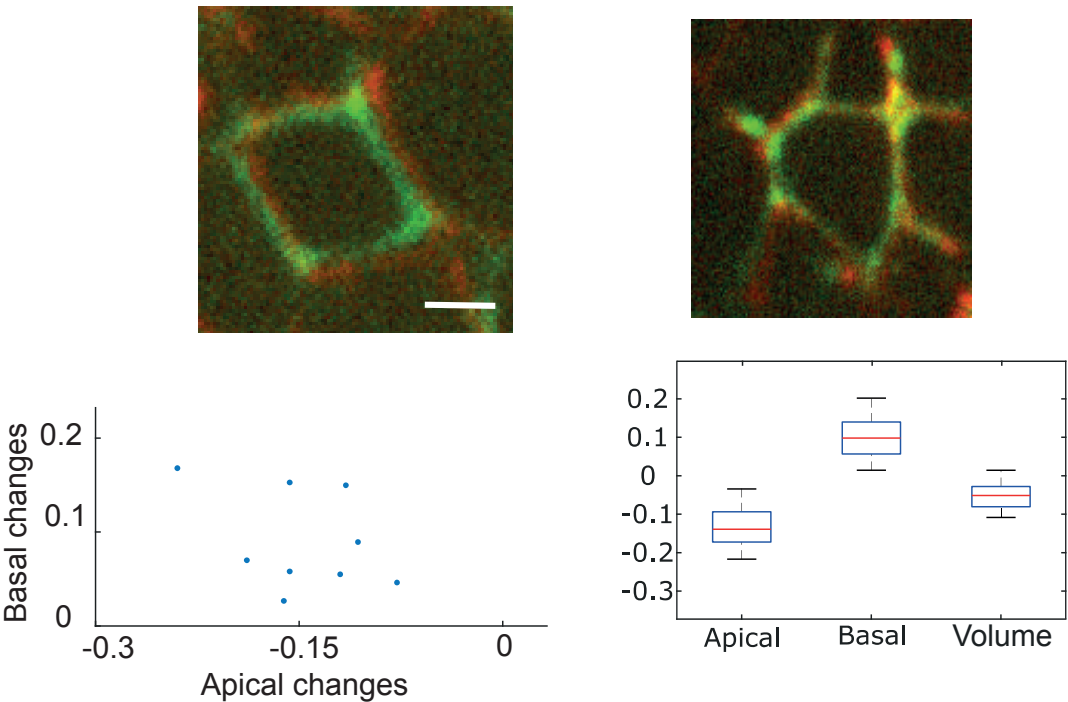


**Figure A.8: Ablation to isolate a cell** Up: Two example images showing the ablation effects, when a cell been isolated. Scale-bar: 5  $\mu m$  Bottom: scatter plot apical and basal area changes for those cells and the box plot for area and volume changes. Scale bar: 5  $mum$

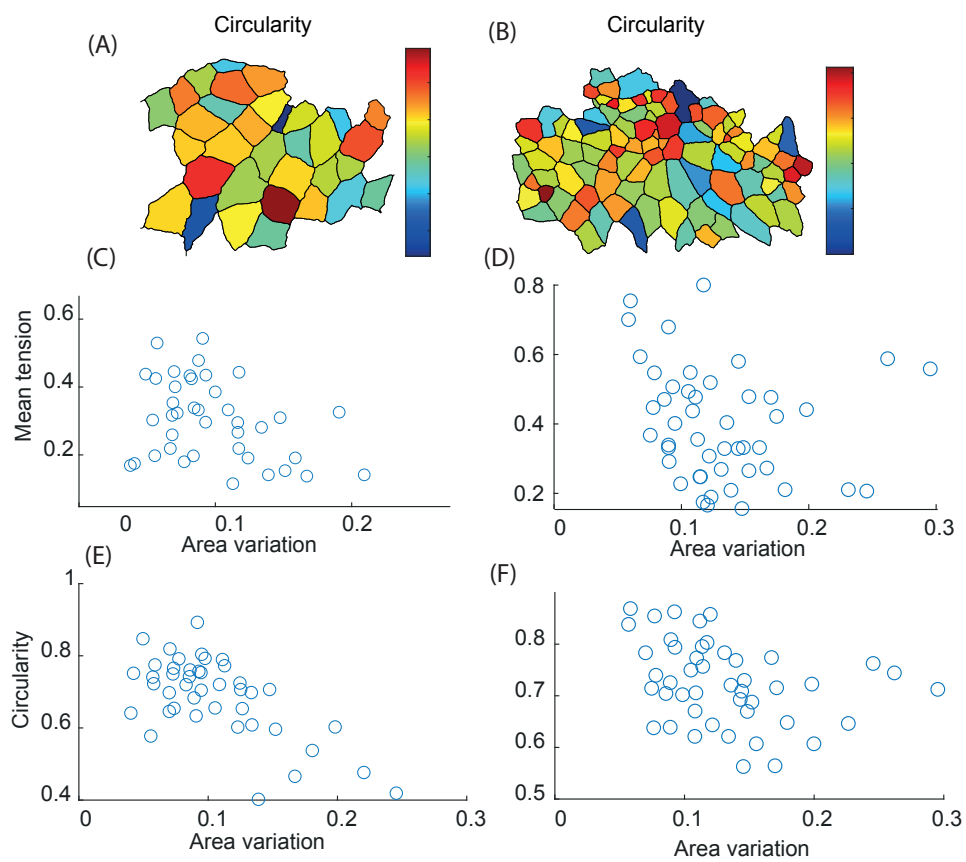


**Figure A.9:** Two examples showing the correlation between area changes, mean tension and circularity.  $R_c = 0.33, R_D = 0.49, R_E = 0.66, R_F = 0.5$

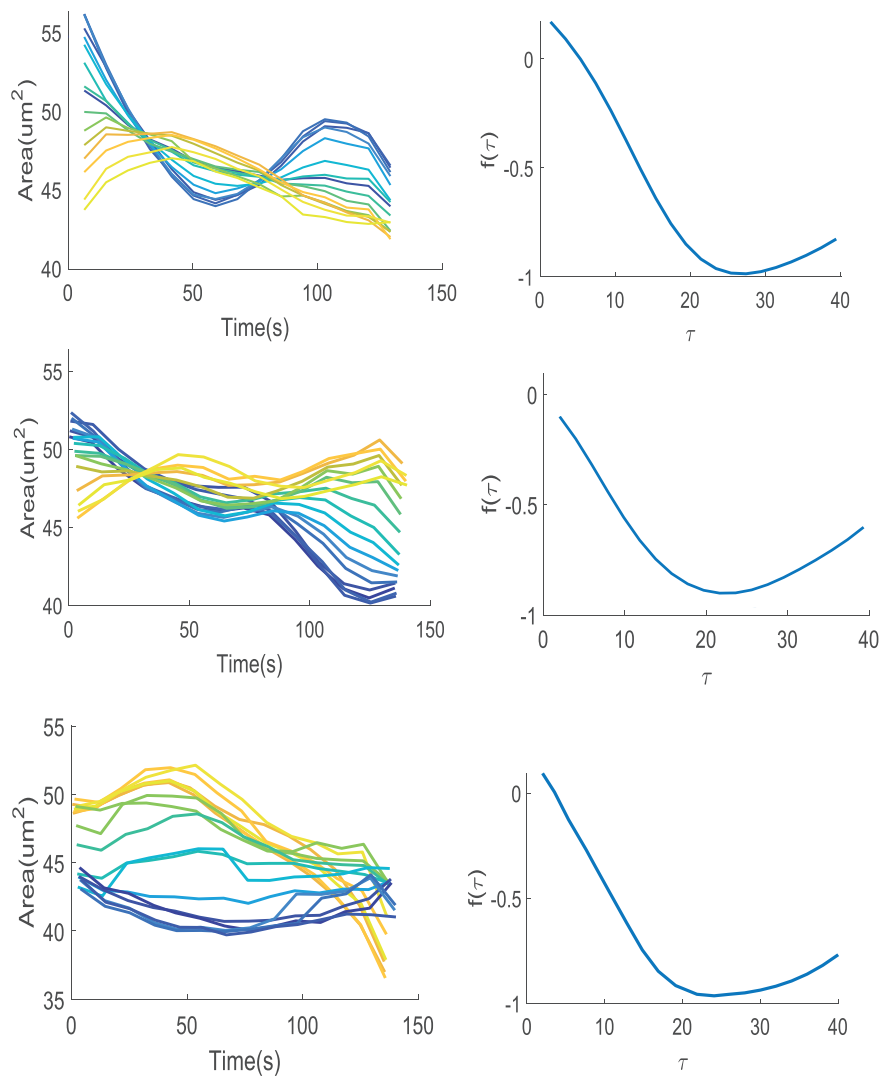


**Figure A.10:** Area changes of pulsed cells in time and space. The left panel represents area plot, (one color indicates one plane, yellowish:basal, bluish: apical). The right panel depicts the cross correlation calculated with the areas.

# Appendix B

## Article

OPEN

# Experimental validation of force inference in epithelia from cell to tissue scale

Weiyuan Kong<sup>1</sup>, Olivier Loison<sup>1</sup>, Pruthvi Chavadimane Shivakumar<sup>1</sup>, Eunice HoYee Chan<sup>1</sup>, Mehdi Saadaoui<sup>2,3</sup>, Claudio Collinet<sup>1</sup>, Pierre-François Lenne<sup>1</sup>  & Raphaël Clément<sup>1</sup> 

Morphogenesis relies on the active generation of forces, and the transmission of these forces to surrounding cells and tissues. Hence measuring forces directly in developing embryos is an essential task to study the mechanics of development. Among the experimental techniques that have emerged to measure forces in epithelial tissues, force inference is particularly appealing. Indeed it only requires a snapshot of the tissue, as it relies on the topology and geometry of cell contacts, assuming that forces are balanced at each vertex. However, establishing force inference as a reliable technique requires thorough validation in multiple conditions. Here we performed systematic comparisons of force inference with laser ablation experiments in four epithelial tissues from two animals, the fruit fly and the quail. We show that force inference accurately predicts single junction tension, tension patterns in stereotyped groups of cells, and tissue-scale stress patterns, in wild type and mutant conditions. We emphasize its ability to capture the distribution of forces at different scales from a single image, which gives it a critical advantage over perturbative techniques such as laser ablation. Overall, our results demonstrate that force inference is a reliable and efficient method to quantify the mechanical state of epithelia during morphogenesis, especially at larger scales when inferred tensions and pressures are binned into a coarse-grained stress tensor.

During embryonic development, a small set of coordinated cell behaviors, including cell division, cell death and cell shape changes, lead to dramatic changes in tissue shapes. These events rely on forces generated at the cell scale, which build up and induce tissue scale movements, such as tissue elongation, tissue invagination or tissue closure (reviewed in<sup>1</sup>). During epithelial morphogenesis, polarized contractile forces acting at cell junctions drive oriented cell intercalation and lead to convergent-extension<sup>2–4</sup>. Stress generated locally can also propagate passively within surrounding cells and tissues as in the *Drosophila* posterior midgut, which largely contributes to elongating the adjacent germband upon invagination<sup>5,6</sup>. The tight genetic control of force generation leads to remarkably stereotyped shape changes, which is exemplified by the robustness of morphogenesis at the embryo scale. A consequence is that misregulation of force generation patterns leads to important morphogenetic defects. Interestingly, such robustness can hold at the scale of a few cells, as revealed by the strikingly regular cellular arrangements of the *Drosophila* retina<sup>7</sup>.

A key step in understanding tissue morphogenesis is thus to establish reliable methods to assess the mechanical state of cells and tissues directly in the developing embryo. Evidently, measuring forces *in vivo* is not an easy task. A wide variety of techniques has recently been developed (for a review, see<sup>8</sup>), which include (but are not limited to) pipette aspiration<sup>9,10</sup>, magnetic tweezers<sup>11</sup>, laser cuts<sup>3,12</sup>, photoelasticity<sup>13</sup>, or deformable microdroplets<sup>14</sup>. All these techniques require to access the tissue of interest with a probe, and are therefore invasive and technically challenging. Optical tweezers have been used to perform non-invasive mechanical measurements at single junctions<sup>15,16</sup>, yet they only provide a small number of local measurements per embryo, and are thus difficult to implement to map the distribution of forces within a tissue. Force inference, which relies on the hypothesis that tensions equilibrate at each vertex, uses the geometry of cell contacts to infer a map of tensions and pressures from a tissue image<sup>17–20</sup>. Because force inference is non-invasive and does not require a specific experimental setup, it stands out as a simple and convenient method.

<sup>1</sup>Aix Marseille Univ, CNRS, IBDM, Turing Center for Living Systems, Marseille, France. <sup>2</sup>Department of Developmental and Stem Cell Biology, Institut Pasteur, 25 rue du Docteur Roux, 75724 Paris Cedex 15, France. <sup>3</sup>CNRS URA2578, rue du Dr Roux, 75015 Paris, France. Correspondence and requests for materials should be addressed to P.-F.L. (email: pierre-francois.lenne@univ-amu.fr) or R.C. (email: raphael.clement@univ-amu.fr)

As pointed out in a recent review<sup>8</sup>, it is now crucial to cross-validate different measurement techniques in model systems in order to assess their robustness and reliability. Such cross-validation experiments require the combination of two or more techniques, and each of them being a technical challenge, cross-validation efforts remain rare in this rather new field of research.

Here, we investigate the accuracy of force inference using cross-validation with laser ablation experiments. Ishihara and co-workers combined force inference and annular laser cuts to show that force inference could predict coarse stress polarity averaged over the whole field of view in the *Drosophila notum*<sup>21</sup>. However, a systematic, detailed cross-validation of force inference in different conditions and at different scales is chiefly missing, in particular for complex tension and stress patterns. To that end, we carried out our analysis at various spatial scales, in four distinct epithelia from two different animals, the fruit fly and the quail. We first validate our force inference algorithms on synthetic data. We then turn to the *Drosophila notum*, and study single junction tension, showing that force inference correlates fairly well with the recoil velocity of vertices following junctional laser cuts. We next turn to the *Drosophila* retinal ommatidia, and show that force inference adequately predicts tension patterns in these stereotyped groups of cells, in both wild type and mutant conditions. Finally, we show that force inference can predict complex tissue-scale stress patterns with unprecedented precision in the wild type and mutant *Drosophila* germband and in the quail early embryo.

Altogether, our cross-validation study on different tissues demonstrates that force inference can be confidently used in 2D to assess the mechanical state of a variety of epithelial tissues. As accuracy increases with the level of coarse graining, we believe it is particularly well suited to determine complex stress patterns at the tissue scale during morphogenesis.

## Results

**Preliminary – choice and validation of the inference methods.** Force inference is an inverse problem of mechanics, which aims at inferring the tensions and pressures that cause angle variations at cell vertices by precisely measuring these angles. It thus requires writing force balance equations at each vertex. A general difficulty is the indefiniteness caused by image boundaries, where edges are connected to one vertex only. The full inverse problem (one tension per edge and one pressure per cell) is indeed generally underdetermined, with fewer equations than unknowns<sup>21</sup>. Different strategies can be adopted to handle this indefiniteness and yield a plausible set of tensions and pressures. First, one can assume that intracellular pressure is constant across the tissue. The problem then becomes overdetermined (more equations than unknowns) and can be solved by computing the pseudo-inverse of the associated matrix<sup>18</sup>. As edges are rarely perfectly straight, suggesting pressure differences between cells, we chose to discard that assumption. Second, one can complement the contact angles measurements with the measurement of the radii of curvature between each pair of adjacent cells. Using Young-Laplace law, this provides another set of conditions that again lead to an overdetermined problem<sup>20</sup>. This is an ideal solution if edge tangents (for tensions) and curvatures (for pressures) can be accurately measured. Third, one can adopt a Bayesian approach, and incorporate statistical expectations for the system as a prior, for instance assuming a Gaussian distribution of tensions<sup>19</sup>. This is a good strategy when curvature measurements are difficult. In all cases, force inference provides relative tension estimates (and so do ablation experiments), as they are determined up to a multiplicative constant. Inferred pressures are determined up to an additive constant (hydrostatic pressure). A common convention is to scale tensions so that the average tension is 1, and to fix the reference average pressure to 0.

Before applying force inference to biological tissues, we first used data generated in silico, a standard procedure to validate proper implementation<sup>18–20</sup>. We generated synthetic data using Surface Evolver<sup>22</sup>, a software that uses energy minimization to drive a system governed by custom line/surface energies to equilibrium (see methods). Briefly, known tensions and pressures are assigned to a regular array, which is then driven to equilibrium. This allows direct comparison of inferred tensions and pressures to known tensions and pressures. Bayesian inference performs very well, as shown by comparisons between the true versus inferred tension and pressure maps (Fig. S1A–C). The correlation is excellent for both tension and pressure, with a Pearson's correlation coefficient above 0.9 (Fig. S1D,E), as expected for synthetic data<sup>19</sup>. We used a similar validation approach to validate our Laplace inference code. This time we used simulations of groups of cells mimicking *Drosophila* ommatidia, the only experimental system that we analyze with Laplace inference (see below). Again, we find an excellent agreement between simulations and force inference, as shown by the tension and pressure maps (Fig. S1F–H). Although the system only has 6 cells and 13 edges, the correlation remains excellent for both tensions and pressures (Fig. S1I,J).

In this article, we preferentially used Bayesian inference<sup>19</sup> for tissues with a large number of cells and small curvatures, that is, the *Drosophila notum* and germband, and the quail embryo. Indeed, we noticed that Laplace inference<sup>20</sup> is prone to error propagation when the system size increases (see methods and Fig. S2 for details). Briefly, this is due to the difficulty to properly determine edge tangents at vertices. Measuring tangents and curvatures requires fitting segmented, pixelated edges. This procedure can introduce errors that propagate to neighboring vertices and edges when the inverse problem is solved. This effect is substantial in the tissues mentioned above, as curvatures are usually tiny and thus hard to determine. Besides, edges often appear as a very open S upon segmentation. This is a typical source of dramatic projection errors upon tangent determination. In contrast, Laplace inference is very well suited for the ommatidia of the *Drosophila* retina. Indeed, ommatidia are stereotyped units composed of only 6 cells with highly stereotyped shapes and very high curvatures, which allow averaging and therefore much easier and reliable measurements of tangents and curvatures.

**Single junction tensions in the *Drosophila notum*.** The most straightforward experimental verification of force inference accuracy is to directly compare tensions inferred in single junctions to measurements obtained from single junction laser ablation, which is the most common experimental technique to evaluate junction tensions. In laser ablation experiments, a tightly focused laser disrupts the molecular structures that support



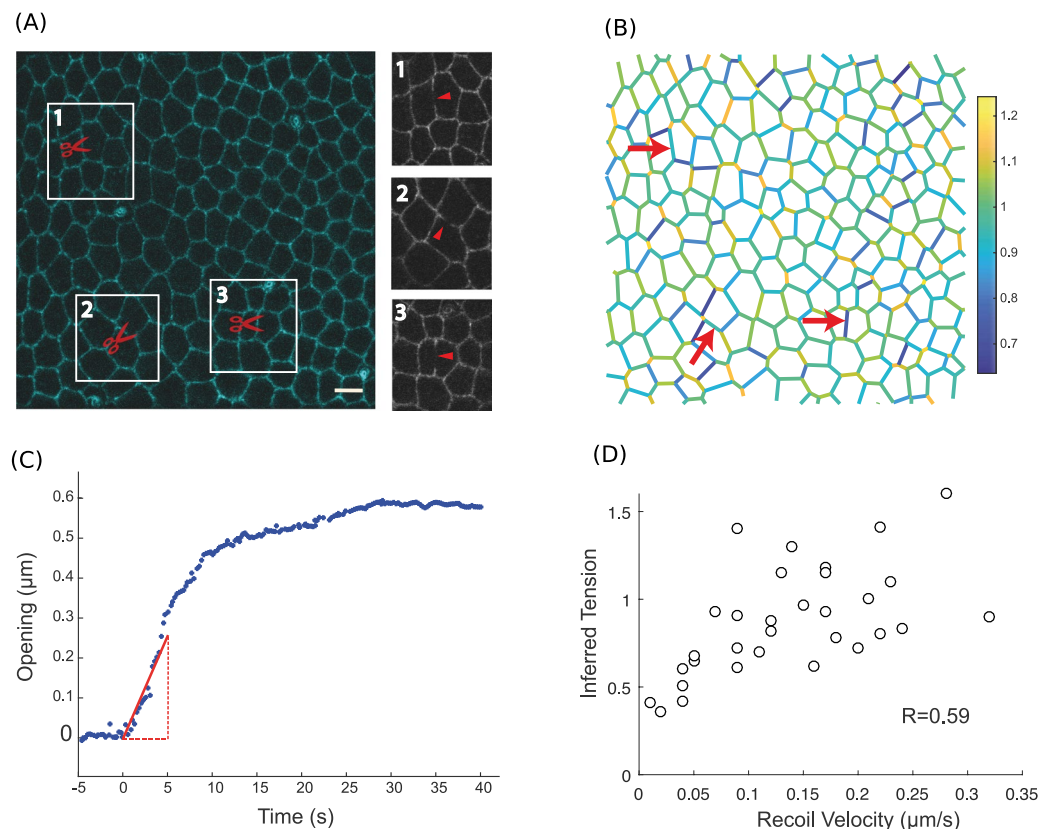


**Figure 1.** Force inference at the single junction scale in the *Drosophila notum* 21 h after pupa formation. (A) Subregion of the *Drosophila notum* 21 h after pupa formation. Scissors show ablation spots where recoil velocities will be measured. Insets show post-ablation snapshots of the considered junctions. Scale bar: 5  $\mu\text{m}$ . (B) Inferred tension map of the tissue region in (A) before the ablations. Red arrows indicate the location of ablations, where inferred tensions are extracted and compared to experimental recoil velocities. (C) Opening dynamics and initial recoil velocity. The red line shows a linear fit of the first 5 seconds, which is used to determine the initial recoil velocity. (D) Inferred tension vs. opening velocity ( $N = 31$  laser cuts from 10 pupae). Pearson's correlation coefficient is 0.59. Spearman's correlation coefficient is 0.63.

tension in a targeted junction. Upon release, tension is only balanced by fluid friction, so that the opening velocity following ablation is proportional to tension<sup>23</sup>. Providing that friction is the same among cuts, ablation thus provides relative estimates of tension. To compare force inference to laser ablation in single junctions, we used a rather regularly organized epithelium, the pupal notum of *Drosophila* around 21 h after pupa formation (Fig. 1A). Tension variations at this stage are not expected to be particularly oriented, as revealed by annular laser cuts<sup>24</sup>. Hence they are essentially random fluctuations that cause the system to slightly deviate from a regular array. Because force inference provides relative estimates, it is always delicate to compare tensions estimated from separate images. We thus hypothesized that the average tension was always the same in all of our images (normalized to 1). To moderate the influence of this assumption, for each field of view where force inference was performed, we did several (3 to 5) laser cuts, sufficiently spaced so as not to influence each other (Figs 1A, S3). Force inference was computed in an image taken prior to the laser cuts (Fig. 1B). We compared the inferred tensions to the initial recoil velocities of the cut junctions, measured by fitting the onset of the opening (Fig. 1C). We found a fairly good correlation coefficient of about 0.6 between opening velocities and inferred tensions (Fig. 1D). The discrepancy can arise from numerous sources: the intrinsic hypotheses of force inference, but also the errors made on velocity measurements, and the assumptions that tension is solely balanced by pure fluid friction and that fluid friction is homogeneous in the tissue. The correlation found despite these limiting factors suggests that both methods can provide reliable results. Of note, the ratios between the recoil velocities are not the same as the ratios between inferred tensions. This is not the case in simulations, which suggests that the error might arise from laser ablation experiments. Besides experimental noise, this might result from systematic nonlinear friction effects (friction force not simply proportional to velocity, so that the recoil velocity is not simply proportional to tension). In addition, since recoil velocities are estimated from a linear fit at the onset of the opening, an error is clearly made by approximating relaxation by a linear fit. The error made actually depends on the relaxation timescale, and thus on tension, which could also be a systematic source of error.

Clearly, measurements in single junctions are overall likely to be prone to more errors than measurements averaged over groups of junctions. Such groups can be based on position (coarse graining), orientation (to detect polarity), or biological identity. We therefore questioned next whether force inference could detect tension gradations between different, stereotyped groups of junctions.

**Tension patterns in wild type and mutant *Drosophila* ommatidia.** Stereotyped patterns of differential tension between subgroups of cells can drive robust geometric organization of multicellular structures. We wanted to assess whether force inference could detect such patterns of tensions. To achieve this, we turned to the retina of *Drosophila*, composed of highly stereotyped groups of cells called ommatidia (Fig. 2A). Previous studies showed that cone cell shapes and arrangement in ommatidia are determined by stereotyped differential tensions<sup>7,25–27</sup>. These tensions were shown to be determined by the amounts of Myosin-II (Myo-II) and E- and N- cadherins recruited at the considered junctions<sup>27</sup>. These amounts were in turn shown to be determined by the “identity” of junctions, that is, by the types of cadherins expressed in the two contacting cells<sup>27</sup>. Based on these previous results, we categorized junctions according to the cadherins expressed in the contacting cells. EN|EN junctions correspond to homotypic junctions separating two cells that both express E- and N-Cadherin. E|E junctions correspond to homotypic junctions separating two cells that both express E-Cadherin only. EN|E junctions correspond to heterotypic junctions separating a cell expressing E-Cadherin only from a cell expressing both E and N-Cadherin. These three types of junctions coexist in a wild type ommatidium (Fig. 2B).

We computed the averaged opening dynamics following laser cuts for each type of junctions, and extracted the corresponding initial recoil velocity (Fig. S4). As previously demonstrated<sup>27</sup>, this revealed a gradation of tensions according to junction type. Homotypic EN|EN junctions have the lowest tensions, E|E junctions have intermediate tensions, and heterotypic EN|E junctions have the highest tensions (Fig. 2D). Note that tensions are directly related to the amounts of Myo-II present at these junctions<sup>27</sup>. To perform force inference in this system, we averaged the geometry of  $N = 51$  ommatidia, and segmented the resulting image (Fig. 2C). As stated earlier, high and stereotyped curvatures in this system make it possible to properly measure the tangents and radii of curvature required for Laplace inference. We found that Laplace inference accurately predicts the pattern of tensions and its gradation among the three types of junctions (Fig. 2D). Note that the cell pressures can also be computed. As expected from Young-Laplace law, the pressure is higher in cone cells than in the surrounding cells (Fig. S5A).

We then turned to the analysis of mosaic experiments in which a fraction of cells do not express N-Cadherin<sup>27</sup>. Since the mutation affects random cells in the tissue, such experiments generate a variety of configurations, in which one or more cone cells are affected by the mutation (Fig. 2E). Interestingly, this modifies the pattern of junction types in the ommatidia, since junction type is determined by which cadherins are expressed by the contacting cells (Fig. 2F). To test whether force inference could still detect tension gradation in these modified conditions, we applied force inference to 5 different configurations of ommatidia (Fig. 2G). Note that, due to the stochastic generation of these configurations, inference is performed on a single ommatidium for each configuration, whereas an average over many ommatidia was used for the wild type condition. Strikingly, the gradation of tensions identified in the wild type condition is systematically detected by force inference in the various mutant configurations (Fig. 2H). This suggests that tensions are indeed determined by the combination of cadherins expressed by adjacent cells, through adhesion strength but also Myo-II level<sup>27</sup>. Inference results are also consistent with laser cuts averaged over all mutant configurations for each junction type (Fig. S5B).

Overall, the results obtained in the retina suggest that force inference can robustly detect tension patterns in stereotyped units of a few cells. This led us to investigate the ability of this technique to detect stress patterns at the scale of the tissue, relevant to many morphogenetic processes.

**Stress pattern in the avian embryo.** Force inference, by coarse graining tensions and pressures at the appropriate scale, can be used to build a map of the stress tensor<sup>19,28</sup>. Very promising results were obtained using this approach to determine the complex stress pattern of the entire *Drosophila* notum<sup>29</sup>. However comparison to experimental stress measurements was only performed at a very coarse level, looking at the overall anisotropy of the whole field of view, by binning tensions and pressures on the whole sample<sup>21</sup>. To investigate the ability of force inference to detect complex stress patterns at large scales, we first turned to the gastrulating avian embryo, using the quail as a model system (Fig. 3A). Although *Drosophila* is the most common model animal to study epithelial mechanics and epithelial morphogenesis, there is no reason that force inference general principles should not apply to other animals. At this early stage, the quail primitive ectoderm is essentially flat with about  $10^5$  cells. Previous studies carried out in chicken and quail during gastrulation have shown the presence of tangential Myosin cables at the margin between the embryo proper and the extra-embryonic territory, driving convergent extension of the presumptive primitive streak<sup>30,31</sup>. To test our force inference in this system, we used circular laser cuts and segmentation of fixed samples stained for ZO-1 (Fig. 3B), which labels the apical membrane, as described in<sup>31</sup>. As previously reported, the deformation following laser cuts is isotropic within the embryo proper, suggesting isotropic stress, but anisotropic at the margin. The principal direction of stress at the margin is orthoradial, that is, tangential to the margin itself (Fig. 3C). Due to the very large number of cells in the whole embryo, we restricted force inference to a region spanning radially from the center of the embryo to the posterior margin (red box, Fig. 3A). We did not detect obvious patterns of junctional tension amplitude (Fig. 3D). We then computed a coarse-grained stress tensor, obtained by binning the results of force inference over square subregions of few tens of cells (see methods). We then plotted its principal directions and amplitudes in each subregion, which recapitulates the anisotropy gradient revealed by circular ablations (Fig. 3F). In the embryonic territory, we find no stress anisotropy. As we get closer to the margin, stress gradually becomes anisotropic and oriented along the orthoradial direction, consistent with the outcome of circular laser cuts. Interestingly, we also observe a pressure gradient across the tissue, with higher pressures in the embryonic territory (Fig. 3E), which might be indicative of differences of mechanical state between the embryonic and extraembryonic territories.

This last analysis confirms the ability of force inference to detect stress patterns at the scale of thousands of cells, and shows that the approach is relevant to animals other than *Drosophila*. However, due to the very large size of the system and to experimental limitations preventing from directly measuring recoil velocities (see methods), our analysis remains essentially qualitative. This prompted us to perform another set of experiments in a system amenable to more precise quantifications.

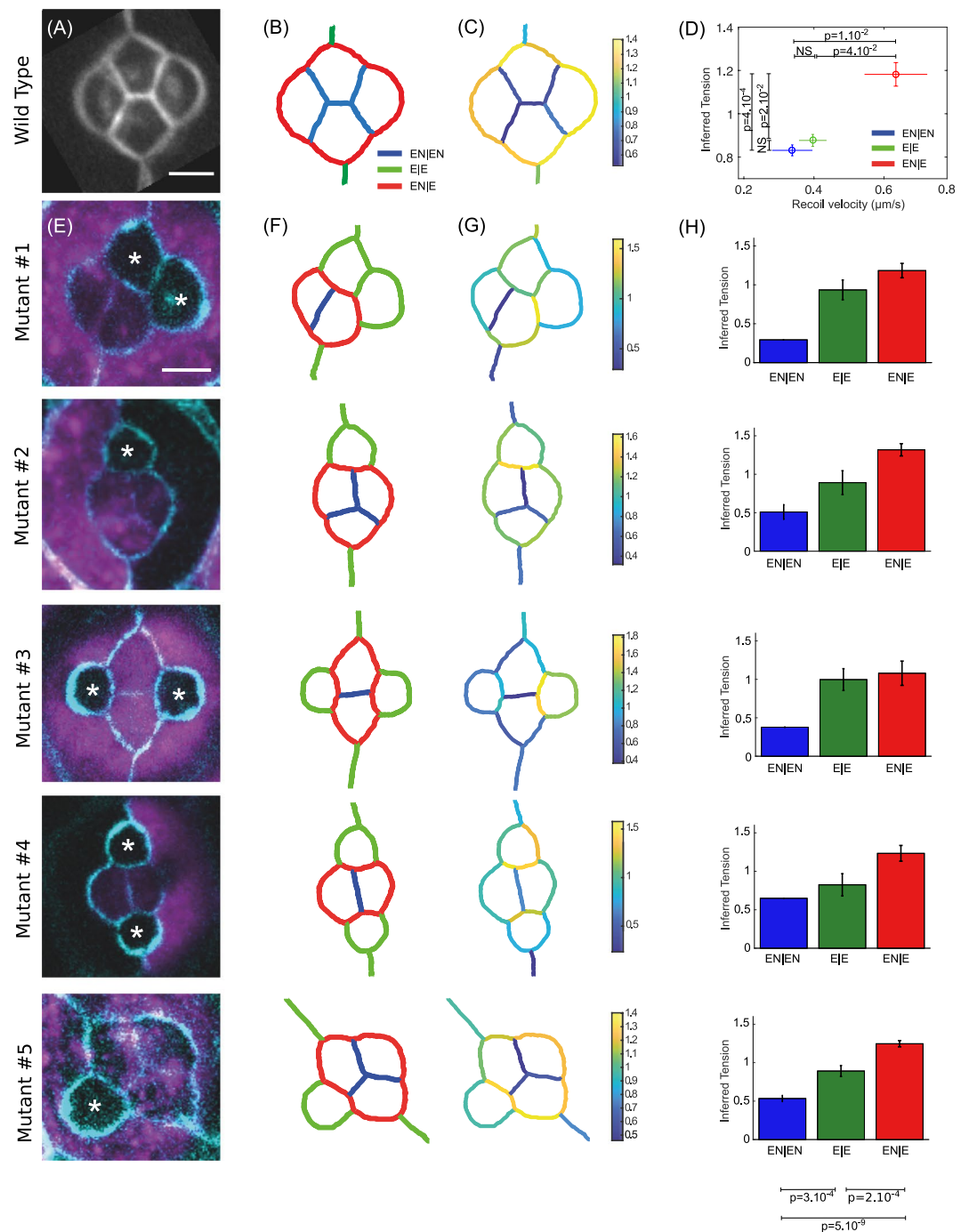


**Figure 2.** Force inference in the *Drosophila* retina. **(A)** The four cone cells of a WT ommatidium. The image results from an average over  $N = 51$  ommatidia. Scale bar:  $5 \mu\text{m}$ . **(B)** Segmented version of **(A)**, and nomenclature of the junction types: EN|EN junctions in blue, E|E in green, and EN|E in red. **(C)** Map of inferred tensions. **(D)** Mean inferred tension vs. mean recoil velocity for each junction type (EN|EN:  $N = 19$ , E|E:  $N = 16$ , EN|E:  $N = 22$ ). **(E)** Five different mutant configurations generated from the mosaic experiments. WT cells are in purple. Starred cells do not express N-Cad. This only affects cone cells, as surrounding cells do not express N-Cad. Scale bar:  $5 \mu\text{m}$ . **(F)** Pattern of junction types for each configuration. **(G)** Map of inferred tension in a single ommatidium for each configuration. **(H)** Average inferred tension for each junction type in each configuration (statistical tests at the bottom pull the five mutant configurations together).

**Stress pattern in the wild type and mutant *Drosophila* germband.** To that end, we turned to a mechanically well-characterized tissue, the embryonic germband of *Drosophila*, that is known to display stress polarity induced by Myo-II polarity, but also a stress gradient along the antero-posterior (AP) axis, due to the movement of the posterior midgut pulling on the tissue<sup>5,6</sup>.

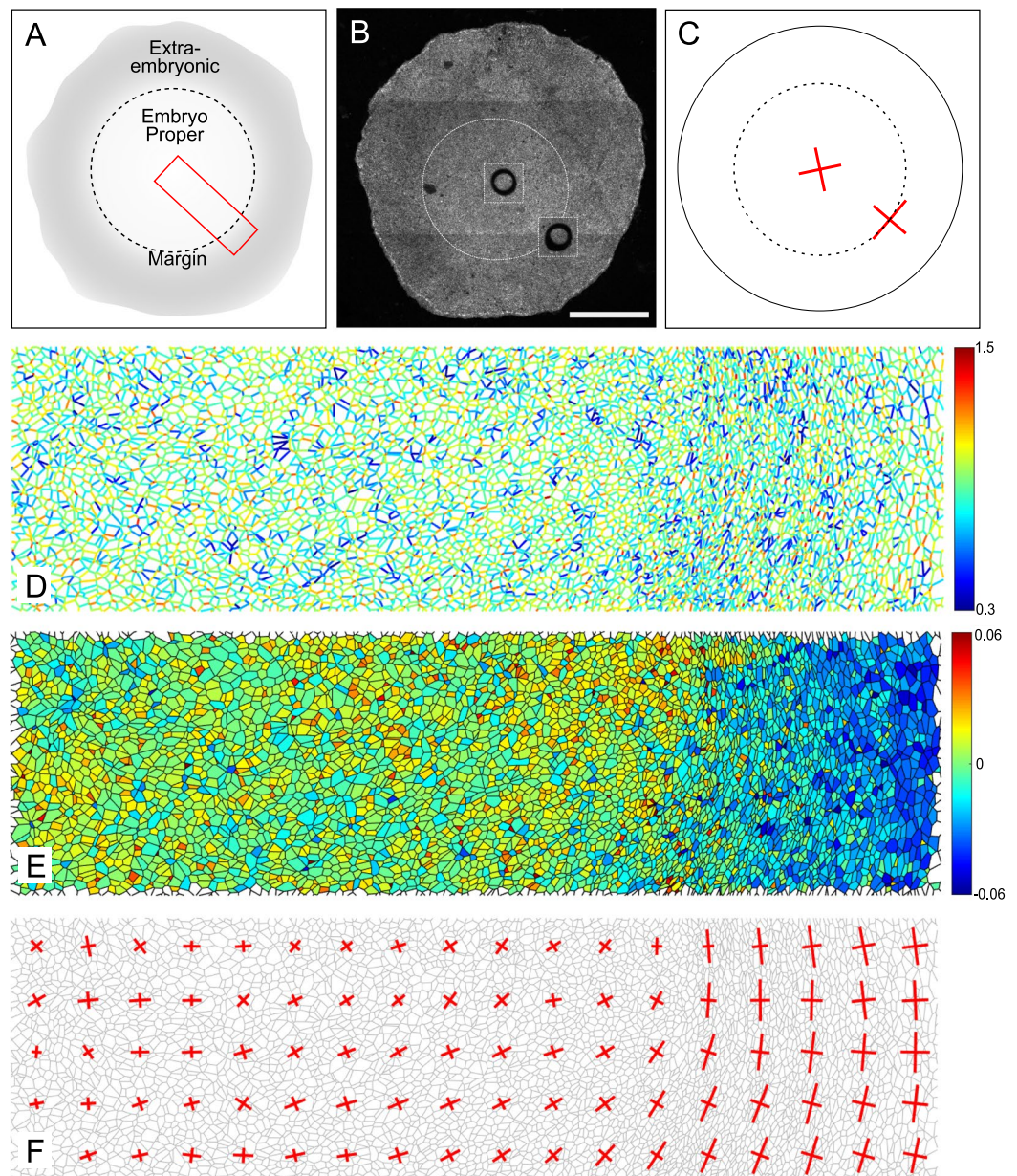


**Figure 3.** Tissue-scale force inference in the quail embryo. **(A)** Schematics of the embryonic and extra-embryonic territories. The red box shows the radial region analyzed with force inference. **(B)** Typical regions used for ablations in the embryonic region and in the posterior margin region. Images 2 minutes after a cut are superimposed on the original image. Scale bar: 1 mm **(C)** Strain measured in the embryonic and margin regions 2 minutes after the cut ( $N = 7$  from 4 embryos). Red crosses show the principal directions and amplitudes of tissue strain measured 2 minutes after the cuts. **(D)** Map of inferred tensions. **(E)** Map of inferred pressures. **(F)** Map of inferred stress. Red crosses show the principal directions and amplitudes of the stress tensor.

In the wild type germband, the polarized recruitment of Myo-II at dorso-ventral (DV) junctions is known to polarize stress and induce polarized cell intercalation. In addition, the posterior midgut, which undergoes rotation and invagination, has been shown to pull on the germband along the AP axis, inducing an additional gradient of stress along this axis (Fig. 4A, left panel). This is illustrated by the opening velocities measured following large AP- or DV-oriented line cuts performed in the anterior, middle and posterior regions of the germband (Fig. 4B, left panel). In the anterior region, away from the posterior midgut, stress is dominated by Myo-II polarity and is strongly polarized along the DV axis. In the middle region, getting closer to the pulling posterior midgut, stress along the AP axis increases, but remains smaller than stress along the DV axis. In the posterior region, stress along the AP axis becomes even larger due to the proximity to the posterior midgut, and stress along the AP and DV axes become comparable, so that stress polarity is lost. We performed force inference on the germband during this process. First, the tension map shows that tensions are indeed higher along the DV axis than along the AP axis (Fig. 4C, left panel), as abundantly reported in literature<sup>3,15,32</sup>. To obtain a better representation of polarity, we

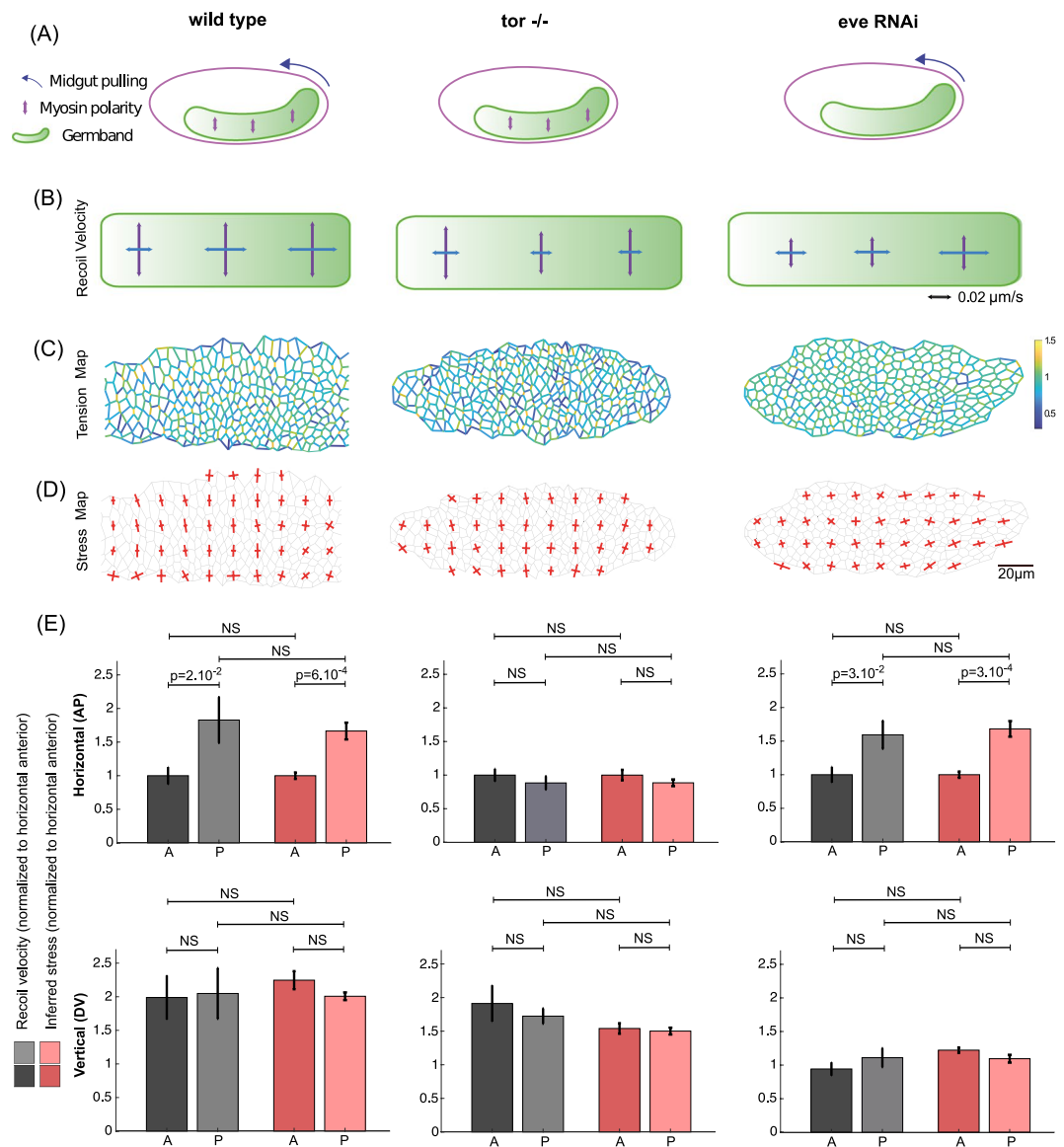


**Figure 4.** Tissue scale force inference in the Drosophila germband. **(A)** Scheme of stress sources in the germband. In the WT condition (left), Myo-II polarity generates stress along the DV axis, and posterior midgut invagination pulls on the germband from its posterior side. In the *Tor*<sup>-/-</sup> condition (middle), posterior midgut invagination is abolished, and Myo-II polarity is preserved. In the *Eve* RNAi condition (right), posterior midgut invagination is preserved, and Myo-II polarity is abolished. **(B)** Recoil velocities measured with PIV for each condition in the anterior, middle and posterior regions of the germband. Vertical arrows correspond to opening velocities along the DV axis (cuts along the AP axis), and horizontal arrows correspond to opening velocities along the AP axis (cuts along the DV axis). Each arrow results from an average over  $N = 7$  to  $N = 34$  experiments. **(C)** Map of inferred tension, in a representative germband for each condition. **(D)** Map of inferred stress. Red crosses show the principal directions and amplitudes of the stress tensor. **(E)** Bar plots of normalized recoil velocity and inferred stress in the horizontal direction (top row) and in the vertical direction (bottom row) for each condition. A stands for anterior, P for posterior. Anterior (resp. posterior) inferred stress is computed as an average over the three most anterior (resp. posterior) columns of **(D)**.

computed the stress tensor, binning over square subregions of typically 8–10 cells. We then plotted its principal directions and amplitudes in each subregion (Fig. 4D, left panel). The results are fully consistent with the laser cut experiments. In the anterior region, stress is largely polarized along the DV axis. Getting closer to the posterior, stress along the AP axis gradually increases, so that in the posterior region, DV polarity is strongly reduced. To further quantify the stress gradients, stress polarity, and the agreement between laser cuts and stress inference, we averaged inferred AP and DV stress in the anterior and posterior regions, and directly compared them to the measured AP and DV recoil velocities in these regions (Fig. 4E, left panels). We find an excellent quantitative agreement between inference and laser cuts. Note that this is also exemplified by a plot of stress anisotropy along the AP axis (Fig. S6). To further test force inference ability to detect stress patterns, we used mutant conditions in

which posterior midgut invagination (Torso<sup>-/-</sup>) or Myo-II polarity (Eve RNAi) are selectively impaired. In the absence of posterior midgut invagination, posterior pulling forces are abolished (Fig. 4A, middle panel), and the stress pattern is mostly determined by Myo-II polarity, with an important DV stress polarity from anterior to posterior (Fig. 4B, middle panel). This is fully recapitulated by the force inference approach (Fig. 4C–E middle panels). In contrast, in the absence of Myo-II polarization, the stress pattern is mostly determined by the posterior forces (Fig. 4A, right panel). Laser cuts show that stress along the DV axis is reduced across all the tissue, while the gradual increase of stress along the AP axis from anterior to posterior is maintained (Fig. 4B, right panel). The stress pattern is again fully recapitulated by the force inference approach (Fig. 4C–E right panels).

Altogether, the analyses of normal and impaired germband extension show that force inference can precisely recapitulate complex stress patterns across a dynamic epithelium undergoing morphogenetic movements. Force inference is also much faster than laser ablations, and the spatial resolution of the estimated stress is much higher.

**Stress tensor based on cell shapes only.** Last, we questioned whether cell shape anisotropy alone was a good indicator of stress anisotropy predicted by force inference at the tissue scale. Interestingly, an approximate stress tensor can be computed without solving the inverse problem, if one assumes that all tensions and pressures are homogeneous. This yields an approximation that is solely based on the contribution of cell shape anisotropies detected by segmentation. Indeed, junction orientations contribute to the stress tensor, with tensions being prefactors (see Batchelor's formula in the methods). Thus, the anisotropy of junction orientation, regardless of tensions, contributes to the anisotropy of stress. Similarly, gradients of junction length will contribute to gradients of stress magnitude.

This simplified analysis actually provides a good approximation of the stress obtained by force inference at the tissue scale, suggesting that junction orientation statistics largely contributes to determining the stress tensor. In the *Drosophila* germband, the error is negligible in most subregions (Fig. S7), even though junction tensions themselves are anisotropic (Fig. 4C). In the quail embryo, this approximation still yields good results, although the error is more important, especially close to the margin (Fig. S8). Besides this deviation from the result obtained with force inference, an obvious drawback of this simplified approach is that it cannot detect junction tension polarity or cell pressure gradients. However, an important advantage is that it does not require to implement force inference, but only segmentation and elementary computation. It is also much faster than force inference, especially in large systems where solving the inverse problem becomes computationally demanding. Finally, the results obtained with this approach suggest that even segmentation might not be mandatory, if the cell shape anisotropies can be properly detected from appropriate spectral analysis of the tissue image. This strategy was recently used to determine stress using Fourier transforms<sup>33</sup>. Our results suggest that it is certainly an interesting option, especially for tissues with a very large number of cells, or tissues in which segmentation is challenging due to imaging difficulties.

## Discussion

Advantages of force inference include that it is fully non-invasive, much easier to perform than perturbative experimental measurements, and does not require assumptions on the origin of forces involved or on the tissue rheology. However, it also comes with several assumptions. First and foremost, that tissue mechanics is essentially driven by in plane tensions and pressures. Second, that tensions are positive, and constant along cell edges. Third, that tensions equilibrate at each vertex, in other words that the magnitude of the net force at vertices (and thus of the friction force opposing movement) should be small compared to individual junctional tensions. This assumption is experimentally verified in various epithelial tissues, the velocity of cells and vertices during development being much smaller than the recoil velocity upon junction ablation. However, it is important to say that tissues in which edges are not tensed (wiggly junctions), tissues that significantly deviate from a 2D plane, or very dynamic tissues, should be considered more carefully. Whether force inference could confidently be used under these assumptions in classic epithelial monolayers was still unclear. Here, we conducted a thorough cross-validation in various epithelial tissues chosen from two animals, at different developmental stages, and with different geometries and dynamics. Our results demonstrate that force inference can be reliably used to analyze the mechanical state of various epithelia, from a few cells to thousands of cells.

We showed that force inference allows fairly good estimates of tension at single junctions. By providing a large set of measurements from single images, force inference can therefore be an asset to search for correlations between tension and protein distribution with good statistics<sup>32</sup>. However, we demonstrated that averaging over groups of junctions of interest, or coarse-graining tension and pressure into a binned stress tensor, significantly improved the reliability of the pattern detected. This is especially striking at the tissue scale. For the germband, a dynamic, morphogenetic tissue with a complex stress pattern, the advantages of using inference were obvious compared to laser cuts, which can be painfully long to perform as they require averaging over many animals. Inference over a single, well-segmented germband not only recapitulated the ablation findings but also allowed a more precise characterization of the stress pattern. Moreover, results obtained in the quail show that such tissue-scale analyses are robust in animals other than *Drosophila*. Taken together, our analyses of the *Drosophila* germband and of the quail embryo show that force inference is particularly well suited to determine stress patterns at the tissue scale during morphogenetic events, as previously done by Guirao and coworkers<sup>29</sup>. Considering that cell movements are likely to induce friction, this suggests that it remains small enough that the hypothesis of equilibrium at vertices remains valid. Force inference could also be an asset to study stress propagation and tissue rheology during morphogenesis, as tissue- or even animal-scale stress patterns and tissue flows can be established by active forces generated locally<sup>34</sup>.

## Methods

**Segmentation.** We used the Tissue Analyzer plugin for FIJI to segment our images<sup>35</sup>. The segmented data (vertices, edges, connectivity) was then passed to Matlab and used for force inference.

**Bayesian force inference.** Bayesian force inference was implemented in a custom Matlab script. The mathematical formulation of the method was first introduced by Ishihara and coworkers<sup>19</sup>. Both tensions and pressures are written as forces acting directly on vertices. The curvature of edges is not considered to solve the inverse problem. Tensions and pressures are determined simultaneously, and the problem is therefore underdetermined. A Gaussian prior on tension distribution is used to overcome the underdetermination. We used SuiteSparse to perform QR decomposition in Matlab<sup>36</sup>.

The stress tensor (Figs 3F and 4D) is then determined using Batchelor's formula<sup>19,28</sup>:

$$\sigma_{\mu\nu} = \left( - \sum_{i=\text{cells}} P_i a_i \delta_{\mu\nu} + \sum_{[ij]=\text{edges}} T_{ij} \frac{l_{ij}^\mu l_{ij}^\nu}{|l_{ij}|} \right) / \sum_{i=\text{cells}} a_i$$

where  $a_i$  is the area of cell  $i$ ,  $P_i$  its pressure,  $\delta$  is Kronecker's symbol,  $T_{ij}$  is the tension of the edge  $[ij]$  separating cells  $i$  and  $j$ , and  $l_{ij}$  the vector connecting the two vertices of edge  $[ij]$ . Red bars show principal directions of  $\sigma$ , and their length is proportional to the corresponding eigenvalues. Note that it is up to the user to choose the appropriate level of coarse-graining. Stress can be computed separately for each cell, or averaged over subregions of any desired size (here, 8–10 cells in the germband, and few tens of cells in the quail embryo).

**Laplace force inference.** Laplace force inference was implemented in a custom Matlab script. The mathematical formulation of the method was introduced by Broadland and coworkers<sup>20</sup>. First, tensions are determined separately by measuring the tangents at each vertex and solving force balance for the whole system (which is then independent of pressures and thus overdetermined). To determine the tangents, we performed linear fits of the first pixels of each edge (8 pixels in our analysis of ommatidia). Next, the curvature of each junction is measured using Taubin circle fitting method<sup>37</sup>. Once curvatures are determined, pressures can be computed using Laplace's law for each pair of adjacent cells. Again, this is an overdetermined system. Note that pressure determination is not crucial to our analysis of ommatidia, since we have no experimental data concerning cell pressures.

To test Laplace force inference with Surface Evolver, we first compute the equilibrium geometry with Surface Evolver, then compute a segmented mask image that we pass to Matlab for analysis. We used a default resolution of 50 pixels/edge for the mask images (on average, as edges have variable lengths). Note that the resolution affects the determination of tangents and curvatures, and thus the accuracy of force inference.

As stated earlier, Laplace force inference is ideal if tangents and curvatures can be determined accurately. Unfortunately, most of the time this is not the case. Indeed, in tissues such as the notum, the germband, the quail embryo or any other similarly organized monolayer, curvatures are small. This can make tangent and curvature measurements tough because of edge pixelation. Even more so, imaging and/or segmentation limitations can result in edges in the shape of a very open S (Fig. S2A), which not only makes tangents and curvatures difficult to assess but can also generate non-compatible angles for the two tangents at both extremities of an edge. Consequently, this inference method is very sensitive to tangent determination through fits of the edges first pixels, and to the number of pixels chosen for the fit. Using too few or too many fit pixels dramatically affects the result of Laplace force inference (Fig. S2B). We also find that determining tangents with circle fits of the whole edge (instead of linear fits of the first few pixels) yields poor results. Errors made on tangents propagate to neighboring edges when the matrix is inverted, which can lead to artefactual gradients in the inferred tension maps (Fig. S2B). A consequence of error propagation is that larger systems are prone to more error (Fig. S2C). This is true for our code, but even more so for CellFIT<sup>20</sup>. Note that we kept the resolution constant when we changed the system size (~50 px/edge). To further investigate error propagation, we introduced errors in a given simulation's inference matrix. First, we computed the matrix of a simulated tissue. We introduced a random error (up to 10%) on a single non-zero projection coefficient randomly chosen in the matrix. We then solved the inverse problem, and computed the correlation between the inferred tensions with and without error introduction. Repeating this operation hundreds of times shows that introduction of an error on projection angles rapidly affects the overall result, even more so when the system has more cells (Fig. S2D). Finally, we provide as examples of error propagation the tension maps provided by our code and by CellFIT for a wild-type *Drosophila* germband (Fig. S2E). Clearly, these maps have artefactual tension gradients, that are not present when we use Bayesian inference. In contrast, Laplace inference is very well suited for ommatidia, as they have high curvatures and only few cells.

**Tissue simulations (surface evolver).** The synthetic tissue data was generated using Surface Evolver v2.7<sup>22</sup>. Surface Evolver evolves the given surface towards its minimal energy configuration by a gradient descent method. In our case we used a classical energy function of the form<sup>38,39</sup>:

$$E = \sum_{[ij]=\text{edges}} \gamma_{ij} l_{ij} + \frac{1}{2} \sum_{i=\text{cells}} k_p (p_i - p_i^0)^2 + \frac{1}{2} \sum_{i=\text{cells}} k_a (a_i - a_i^0)^2$$

where  $p_i$  and  $a_i$  are the perimeter and area of cell  $i$ , and  $p_i^0$  and  $a_i^0$  its target perimeter and target area.  $k_p$  and  $k_a$  are the strengths associated to the perimeter and area constraints, respectively.  $\gamma_{ij}$  is the line tension in edge  $[ij]$ , and  $l_{ij}$  its length.

The pressure in cell  $i$  ("known" pressure) is then given by  $P_i = -k_a (a_i - a_i^0)$ , and the total tension of edge  $[ij]$  ("known" tension) is given by  $T_{ij} = \gamma_{ij} + k_p (p_i - p_i^0) + k_p (p_j - p_j^0)$ .

In the tissue simulation (Fig. S1B), the target area is set to 0.87 and  $k_a$  is set to 2. For the sake of simplicity, the target perimeters are all set to 0.  $k_p$  is set to 0.15. Line tensions  $\gamma_{ij}$  are randomly assigned from a Gaussian distribution (mean = 1, std = 1/6) prior to equilibration.

In the ommatidium simulation (Fig. S1G), the target area is set to 5.5 for top-bottom cone cells, 5 for right-left cone cells and 40.49 for surrounding cells.  $k_a$  is set to 38.2 and  $k_p$  is set to 0. Tensions  $T_{ij} = \gamma_{ij}$  are directly set to 0.75 for E|E junctions, 0.6 for EN|EN junctions, and 1.45 for EN|E junctions.

Note that whether these values are realistic or not is of little concern, since their only purpose is to demonstrate the proper implementation of force inference.

**Tissue curvature.** Most biological tissues are not completely flat. When using force inference, one should be careful about this aspect, as approximating out-of-plane forces looking at their 2D projection can introduce significant errors if the curvature is important. For the tissues analyzed in this paper, we measured the ratio  $Q = h/L$  between the height  $h$  required to image the apical surface and the image size  $L$ , which provides a non-dimensional estimate of curvature. We find that  $Q$  is about 1.5% in our notum images, 3.5% in our retina images, 4.3% in our germband images, and 3.5% in our quail images, ensuring that the apical surfaces of tissues analyzed throughout the paper were reasonably flat.

**Flies and quails.** For the experiments in the *Drosophila notum*, Ecad:GFP/Sqh:MCherry flies were used.

For the experiments in the *Drosophila* ommatidia, E-CAD:GFP; N-CAD:mkate2 flies were used<sup>27</sup>. Mosaic experiments were also described in a previous paper<sup>27</sup>.

For the experiments in the *Drosophila* germband, a; E-cad::GFP<sup>K1</sup> fly line was used as wild type, embryos from a; tor<sup>4</sup>, E-cad::GFP<sup>K1In</sup> were used as Torso<sup>-/-</sup> and dsRNAs against even-skipped injected in embryos form; E-cad::GFP<sup>K1</sup> flies as previously described<sup>2,6</sup> to obtain eve loss-of-function embryos.

For quail embryo stainings, quail embryos were fixed in ice cold 4% formaldehyde/PBS for at least 1 h, permeabilized in PBS/0.1% Triton X-100 (PBT 0.1%) before a blocking step in PBT 0.1%/2% BSA (from Roche)/10% FBS (from Gibco). Primary antibodies used in this study are mouse anti-ZO1 (Invitrogen ZO1-1A12), rabbit anti-pMyosin light chain 2 (Cell Signaling Technology CST-3671S and CST-3674S), mouse anti- $\beta$ -Catenin (BD Transduction Laboratories<sup>TM</sup>, clone 14) and rabbit anti-h/mCaspase3 (RD Systems AF835). Secondary antibodies coupled to AlexaFluor 488, 555, or 647 were obtained from Invitrogen and used at 1:200 dilutions. Embryos were then mounted with DAPI-containing Fluoromount-GTM (eBioscience) between slide and coverslip.

**Laser ablations.** Laser ablation experiments in *Drosophila* were performed on a previously described setup<sup>3</sup>. Junction cuts in the retina were described in a previous article<sup>27</sup>. Line cuts in the germband were also described in a previous article<sup>6</sup>.

Laser ablation experiments in quail embryos were performed live using a 355-nm pulsed laser (75–100% power), a UGA-42 module from Rapp Optoelectronic coupled to a Zeiss LSM 880 and a 5X or 10X objective (see<sup>31</sup> for details).

**Ablation measurements.** In the *Drosophila notum*, we used kymographs along lines parallel to the severed junctions to automatically track the movement of vertices. Kymographs were then oversampled and treated with a Gaussian filter to avoid pixelation effects in vertex detection. Vertices positions were determined at each time point with a Gaussian fit of the intensity. Despite these efforts, the data can still be quite noisy. Besides, we needed to fit separately each single opening curve, without the possibility to average over several junctions as we wanted to do single junction comparisons with force inference. Thus, to determine the initial recoil velocity we had to perform a linear fit on the first 5 seconds. The fitting time was determined empirically, as too short fitting times are very much affected by noise, and too long fitting times yield poor estimates as opening is rather exponential or bi-exponential than linear. Note that we used linear fits of the onset of relaxation rather than exponential or bi-exponential fits of the full relaxation process for an empirical reason. Only fitting the first few points clearly focuses error minimization on the onset of relaxation, whereas fitting the whole relaxation with exponentials might overall give a better fit, but possibly at the expense of the onset of opening, as it is only a small subset of the relaxation curve.

In the *Drosophila* retina, automated detection with kymographs could not be used, due to smaller cells, edge curvatures, and higher signal loss following ablations. Hence, we used a manual tracking approach of the vertices, using FIJI. In this case, opening curves could be averaged over several junctions, which yielded much less noisy curves. Hence we could estimate the opening velocity on a much smaller timescale, looking at the first 250 ms. Note that the gradation observed is still found if we fit curves independently on a longer timescale (as it is done in the notum), then average velocities for each junction type. This strategy was actually the one used in our previous paper<sup>27</sup>, and yielded a similar gradation. Velocities determined here are closer to the actual “initial” velocity, as they are measured on a shorter timescale after the cut. The higher values found here suggest that it is indeed the case.

In the *Drosophila* germband, the opening velocities were determined by Particle Image Velocimetry (PIV), as several junctions are involved in the opening process. The measurement routine was described in a previous article<sup>6</sup>. In short, PIV is computed between a snapshot taken upon ablation and a snapshot taken 2 s after ablation. The velocity field is averaged in a region adjacent to the cut line to obtain a scalar velocity value.

In the quail embryo, tissue strain was evaluated based on the deformation of the tissue 2 minutes after the cut, from a PIV analysis of the resulting time-lapse movies. Note that the initial opening velocity could not be measured since relaxation occurred on a time scale comparable to the time taken to make the cuts (see<sup>31</sup> for details). This prevented a quantitative analysis of initial recoil velocities vs. inferred stress.



**Statistics.** We use Pearson's correlation coefficient to determine the correlation in scatter plots. We use unpaired Student t-tests to determine whether distribution means are significantly different. N.S. stands for non-significant and is used when  $p > 0.05$ . If  $p < 0.05$ , its value is reported directly on the graph. Error bars on all plots represent the standard error of the mean.

## Data Availability

Data will be made available upon request.

## References

1. Heisenberg, C. P. & Bellaïche, Y. Forces in tissue morphogenesis and patterning. *Cell* **153** (2013).
2. Bertet, C., Sulak, L. & Lecuit, T. Myosin-dependent junction remodelling controls planar cell intercalation and axis elongation. *Nature* **429**, 667–71 (2004).
3. Rauzi, M., Verant, P., Lecuit, T. & Lenne, P.-F. Nature and anisotropy of cortical forces orienting *Drosophila* tissue morphogenesis. *Nat. Cell Biol.* **10**, 1401–10 (2008).
4. Fernandez-Gonzalez, R. *et al.* Myosin II Dynamics Are Regulated by Tension in Intercalating Cells. *Dev. Cell* **17**, 736–743 (2009).
5. Lye, C. M. *et al.* Mechanical Coupling between Endoderm Invagination and Axis Extension in *Drosophila*. *PLoS Biol.* **13**, 1–27 (2015).
6. Collinet, C., Rauzi, M., Lenne, P. & Lecuit, T. Local and tissue-scale forces drive oriented junction growth during tissue extension. *Nat. Cell Biol.* **17**, 1247–1258 (2015).
7. Hayashi, T. & Carthew, R. W. Surface mechanics mediate pattern formation in the developing retina. *Nature* **431**, 647–652 (2004).
8. Sugimura, K., Lenne, P.-F. & Graner, F. Measuring forces and stresses *in situ* in living tissues. *Development* **143**, 186–196 (2016).
9. Guevorkian, K., Colbert, M. J., Durth, M., Dufour, S. & Brochard-Wyart, F. Aspiration of biological viscoelastic drops. *Phys. Rev. Lett.* **104**, 1–4 (2010).
10. Maitre, J. L. *et al.* Adhesion Functions in Cell Sorting by Mechanically Coupling the Cortices of Adhering Cells. *Science* (80-). **338**, 253–256 (2012).
11. Doubrovinski, K., Swan, M., Polyakov, O. & Wieschaus, E. F. Measurement of cortical elasticity in *Drosophila melanogaster* embryos using ferrofluids. *Proc. Natl. Acad. Sci.* **114**, 201616659 (2017).
12. Ma, X., Lynch, H. E., Scully, P. C. & Hutson, M. S. Probing embryonic tissue mechanics with laser hole drilling. *Phys. Biol.* **6** (2009).
13. Nienhaus, U., Aegerter-Wilmsen, T. & Aegerter, C. M. Determination of mechanical stress distribution in *Drosophila* wing discs using photoelasticity. *Mech. Dev.* **126**, 942–949 (2009).
14. Campàs, O. *et al.* Quantifying cell-generated mechanical forces within living embryonic tissues. *Nat. Methods* **11**, 183–189 (2014).
15. Bambardekar, K., Clément, R., Blanc, O., Chardès, C. & Lenne, P.-F. Direct laser manipulation reveals the mechanics of cell contacts *in vivo*. *Proc. Natl. Acad. Sci.* **112**, 1416–1421 (2015).
16. Clément, R., Dehapiot, B., Collinet, C., Lecuit, T. & Lenne, P. F. Viscoelastic Dissipation Stabilizes Cell Shape Changes during Tissue Morphogenesis. *Curr. Biol.* 3132–3142, <https://doi.org/10.1016/j.cub.2017.09.005> (2017).
17. Stein, M. B. & Gordon, R. Epithelia as bubble rafts: A new method for analysis of cell shape and intercellular adhesion in embryonic and other epithelia. *J. Theor. Biol.* **97**, 625–639 (1982).
18. Chiou, K. K., Hufnagel, L. & Shraiman, B. I. Mechanical stress inference for two dimensional cell arrays. *PLoS Comput. Biol.* **8** (2012).
19. Ishihara, S. & Sugimura, K. Bayesian inference of force dynamics during morphogenesis. *J. Theor. Biol.* **313**, 201–211 (2012).
20. Brodland, G. W. *et al.* CellFIT: A cellular force-inference toolkit using curvilinear cell boundaries. *PLoS One* **9** (2014).
21. Ishihara, S. *et al.* Comparative study of non-invasive force and stress inference methods in tissue. *Eur. Phys. J. E* **36**, 45 (2013).
22. Brakke, K. A. The Surface Evolver. *Exp. Math.* **1**, 141–165 (1992).
23. Rauzi, M. & Lenne, P.-F. Probing cell mechanics with subcellular laser dissection of actomyosin networks in the early developing *Drosophila* embryo. *Methods Mol. Biol.* **1189**, 209–218 (2015).
24. Bonnet, I. *et al.* Mechanical state, material properties and continuous description of an epithelial tissue. *J. R. Soc. Interface* **9**, 2614–2623 (2012).
25. Käfer, J., Hayashi, T., Marée, A. F. M., Carthew, R. W. & Graner, F. Cell adhesion and cortex contractility determine cell patterning in the *Drosophila* retina. *Proc. Natl. Acad. Sci. USA* **104**, 18549–18554 (2007).
26. Hilgenfeldt, S., Erisken, S. & Carthew, R. W. Physical modeling of cell geometric order in an epithelial tissue. *Proc. Natl. Acad. Sci.* **105** (2008).
27. Chan, E. H., Chavadimane Shivakumar, P., Clément, R., Laugier, E. & Lenne, P.-F. Patterned cortical tension mediated by N-cadherin controls cell geometric order in the *Drosophila* eye. *Elife* **6**, 1–27 (2017).
28. Batchelor, G. K. The stress system in a suspension of force-free particles. *J. Fluid Mech.* **41**, 545–570 (1970).
29. Guirao, B. *et al.* Unified quantitative characterization of epithelial tissue development. *Elife* **4**, 1–52 (2015).
30. Rozbicki, E. *et al.* Myosin-II-mediated cell shape changes and cell intercalation contribute to primitive streak formation. *Nat. Cell Biol.* **17**, 397–408 (2015).
31. Saadaoui, M., Corson, F., Rocancourt, D., Roussel, J. & Gros, J. A tensile ring drives tissue flows to shape the gastrulating amniote embryo. *bioRxiv* **33**, 412767 (2018).
32. Kale, G. R. *et al.* Distinct contributions of tensile and shear stress on E-cadherin levels during morphogenesis. *Nat. Commun.* **9** (2018).
33. Durande, M. *et al.* Fast determination of cell anisotropy and size in epithelial tissue images using Fourier Transform. *arXiv Prepr.* 1–13 (2018).
34. Dicko, M. *et al.* Geometry can provide long-range mechanical guidance for embryogenesis. *PLoS Comput. Biol.* **13**, 1–30 (2017).
35. Aigouy, B. *et al.* Cell Flow Reorients the Axis of Planar Polarity in the Wing Epithelium of *Drosophila*. *Cell* **142**, 773–786 (2010).
36. Davis, T. A. Algorithm 915, SuiteSparseQR: Multifrontal Multithreaded Rank-revealing Sparse QR Factorization. *ACM Trans. Math. Softw.* **38**, 8:1–8:22 (2011).
37. Taubin, G. Estimation of planar curves, surfaces, and nonplanar space curves defined by implicit equations with applications to edge and range image segmentation. *IEEE Trans. Pattern Anal. Mach. Intell.* **13**, 1115–1138 (1991).
38. Nagai, T. & Honda, H. A dynamic cell model for the formation of epithelial tissues. *Philos. Mag. B* 699–720, <https://doi.org/10.1080/13642810108205772> (2001).
39. Ouchi, N. B., Glazier, J. A., Rieu, J. P., Upadhyaya, A. & Sawada, Y. Improving the realism of the cellular Potts model in simulations of biological cells. *Phys. A Stat. Mech. its Appl.* **329**, 451–458 (2003).

## Acknowledgements

We thank Claire Chardès for her assistance with the laser ablation setup; S. Ishihara and K. Sugimura for suggesting using SuiteSparse for QR decompositions; Jérôme Gros and Francis Corson for their assistance with the quail data; and François Graner for his helpful comments on the manuscript. We also thank members of Lenne and Lecuit groups for discussions throughout the course of this project and for providing a stimulating scientific environment. WK is supported by a Ph.D. fellowship from the LabEx INFORM (ANR-11-LABX-0054)

and of the A\*MIDEX project (ANR-11-IDEX-0001-02), funded by the “Investissements d’Avenir” French Government program. The project was in part funded by the ANR grant ANR-17-CE13-0032. We acknowledge France-BioImaging infrastructure supported by the French National Research Agency (ANR-10-INBS-04-01, «Investments for the future»).

### Author Contributions

W.K. conducted the laser cutting experiments in the notum and analyzed the data. P.S. conducted the laser cutting experiments in the retina, W.K. and P.S. analyzed the data. E.C. conducted the mosaic experiments in the retina. C.C. conducted the laser cutting experiments in the germband and analyzed the data. M.S. conducted the laser cutting experiments in the quail. R.C., W.K. and O.L. implemented the force inference codes and their verification with Surface Evolver. W.K. conducted the force inference analysis in the notum and in the retina. R.C. conducted the force inference analysis in the germband and in the quail. R.C. and P.F.L. designed the project. R.C., W.K. and P.F.L. discussed the data. R.C. and W.K. wrote the paper. All authors commented on it.

### Additional Information

**Supplementary information** accompanies this paper at <https://doi.org/10.1038/s41598-019-50690-3>.

**Competing Interests:** The authors declare no competing interests.

**Publisher’s note** Springer Nature remains neutral with regard to jurisdictional claims in published maps and institutional affiliations.



**Open Access** This article is licensed under a Creative Commons Attribution 4.0 International License, which permits use, sharing, adaptation, distribution and reproduction in any medium or format, as long as you give appropriate credit to the original author(s) and the source, provide a link to the Creative Commons license, and indicate if changes were made. The images or other third party material in this article are included in the article’s Creative Commons license, unless indicated otherwise in a credit line to the material. If material is not included in the article’s Creative Commons license and your intended use is not permitted by statutory regulation or exceeds the permitted use, you will need to obtain permission directly from the copyright holder. To view a copy of this license, visit <http://creativecommons.org/licenses/by/4.0/>.

© The Author(s) 2019

## Bibliography

- Aigouy B, Umetsu D, E. S., Aigouy, B., Umetsu, D., & Eaton, S. (2016). Segmentation and Quantitative Analysis of Epithelial Tissues. *Methods Mol Biol*, 1478, 227–239. [https://doi.org/10.1007/978-1-4939-6371-3\\_13](https://doi.org/10.1007/978-1-4939-6371-3_13)
- Aigouy, B., Cortes, C., Liu, S., & Prud'Homme, B. (2020). EPySeg: a coding-free solution for automated segmentation of epithelia using deep learning. *Development (Cambridge, England)*, 147(24). <https://doi.org/10.1242/dev.194589>
- Albert, B. (2002). Molecular Biology of the Cell. In *Journal of Clinical Pathology* (4th ed., Vol. 43, Issue 4). <https://doi.org/10.1136/jcp.43.4.351-c>
- Alomari, M. (2004). Color Atlas of Cytology, Histology and Microscopic Anatomy Wolfgang Keuhnel. 2003, 534 pages. Thieme, New York 2003, ISBN 3-13-562404-8 (GTV), ISBN 1-58890-175-0 (TNY). *Annals of Saudi Medicine*, 24(5), 403–403. <https://doi.org/10.5144/0256-4947.2004.403>
- Baena-López, L. A., Baonza, A., & García-Bellido, A. (2005). The orientation of cell divisions determines the shape of Drosophila organs. *Current Biology*, 15(18), 1640–1644. <https://doi.org/10.1016/j.cub.2005.07.062>
- Bambardekar, K., Clément, R., Blanc, O., Chardès, C., & Lenne, P.-F. F. (2015). Direct laser manipulation reveals the mechanics of cell contacts in vivo. *Proceedings of the National Academy of Sciences*, 112(5), 1416–1421. <https://doi.org/10.1073/pnas.1418732112>
- Batchelor, G. K. (1970). The stress system in a suspension of force-free particles. *Journal of Fluid Mechanics*, 41(3), 545–570. <https://doi.org/10.1017/s0022112070000745>
- Bertet, C., Sulak, L., & Lecuit, T. (2004a). Myosin-dependent junction remodelling controls planar cell intercalation and axis elongation. *Nature*, 429(6992), 667–671. <https://doi.org/10.1038/nature02590>
- Bi, D., Yang, X., Marchetti, M. C., & Manning, M. L. (n.d.). *Motility-Driven Glass and Jamming Transitions in Biological Tissues*. <https://doi.org/10.1103/PhysRevX.6.021011>
- Blair, S. S. (2003). Genetic mosaic techniques for studying Drosophila development. *Development*, 130(21), 5065–5072. <https://doi.org/10.1242/dev.00774>
- Blaser, H., Reichman-Fried, M., Castanon, I., Dumstrei, K., Marlow, F. L. L., Kawakami, K., Solnica-Krezel, L., Heisenberg, C. P., & Raz, E. (2006). Migration of Zebrafish Primordial Germ Cells: A Role for Myosin Contraction and Cytoplasmic Flow. *Developmental Cell*, 11(5), 613–627. <https://doi.org/10.1016/j.devcel.2006.09.023>
- Boller, K., Vestweber, D., & Kemler, R. (1985). Cell-adhesion molecule uvomorulin is localized in the intermediate junctions of adult intestinal epithelial cells. *Journal of Cell Biology*, 100(1), 327–332. <https://doi.org/10.1083/jcb.100.1.327>
- Bonnet, I., Marcq, P., Bosveld, F., Fetler, L., Bellaïche, Y., & Graner, F. (2012). Mechanical state, material properties and continuous description of an epithelial tissue. *Journal of The Royal Society Interface*, 9(75), 2614–2623. <https://doi.org/10.1098/rsif.2012.0263>
- Brodland, G. W., Veldhuis, J. H., Kim, S., Perrone, M., Mashburn, D., & Hutson, M. S. (2014). CellFIT: A cellular force-inference toolkit using curvilinear cell boundaries. *PLoS ONE*, 9(6), e99116. <https://doi.org/10.1371/journal.pone.0099116>
- Campàs, O., Mammoto, T., Hasso, S., Sperling, R. A., O'connell, D., Bischof, A. G., Maas, R., Weitz, D. A., Mahadevan, L., & Ingber, D. E. (2014). Quantifying cell-generated mechanical forces within living embryonic tissues. *Nature Methods*, 11(2), 183–189. <https://doi.org/10.1038/nmeth.2761>
- Chan, E. H., Chavadimane Shivakumar, P., Clément, R., Laugier, E., & Lenne, P.-F. (2017). Patterned cortical tension mediated by N-cadherin controls cell geometric order in the Drosophila eye. *ELife*, 6, 1–27. <https://doi.org/10.7554/eLife.22796>
- Chaurasia, A., & Culurciello, E. (2017). LinkNet: Exploiting Encoder Representations for Efficient Semantic Segmentation. *2017 IEEE Visual Communications and Image Processing, VCIP 2017, 2018-January*, 1–4. <https://doi.org/10.1109/VCIP.2017.8305148>
- Chengappa, P., Sao, K., Jones, T. M., & Petrie, R. J. (2018). Intracellular Pressure : A Driver of Cell Morphology and Movement. In *International Review of Cell and Molecular Biology* (1st ed., Vol. 337). Elsevier Inc. <https://doi.org/10.1016/bs.ircmb.2017.12.005>
- Collinet, C., Rauzi, M., Lenne, P.-F. F. P., & Lecuit, T. (2015). Local and tissue-scale forces drive oriented junction growth during tissue extension. *Nature Cell Biology*, 17(10), 1247–1258. <https://doi.org/10.1038/ncb3226>
- Condic, M. L., Fristrom, D., & Fristrom, J. W. (1991). Apical cell shape changes during Drosophila imaginal leg disc elongation: a novel morphogenetic mechanism. In *Development* (Vol. 111, Issue 1). The Company of Biologists. <https://doi.org/10.1242/DEV.111.1.23>
- Coravos, J. S., Mason, F. M., & Martin, A. C. (2017). Actomyosin Pulsing in Tissue Integrity Maintenance during Morphogenesis. In *Trends in Cell Biology* (Vol. 27, Issue 4, pp. 276–283). Elsevier Ltd. <https://doi.org/10.1016/j.tcb.2016.11.008>
- David, D. J. V., McGill, M. A., McKinley, R. F. A., & Harris, T. J. C. (2012). Live imaging of Drosophila embryos: Quantifying protein numbers and dynamics at subcellular locations. *Methods in Molecular Biology*, 839, 1–17.

## Bibliography

- [https://doi.org/10.1007/978-1-61779-510-7\\_1](https://doi.org/10.1007/978-1-61779-510-7_1)
- Davidson, L. A., Koehl, M. A., Keller, R., & Oster, G. F. (1995). How do sea urchins invaginate? Using biomechanics to distinguish between mechanisms of primary invagination. *Development*, *121*(7), 2005–2018. <https://doi.org/10.1242/dev.121.7.2005>
- Davis, T. A. (2018). Algorithm 9xx: SuiteSparse:GraphBLAS: graph algorithms in the language of sparse linear algebra. In *ACM Trans. Math. Softw.* *1, 1, Article* (Vol. 1).
- Dicko, M., Saramito, P., Blanchard, G. B., Lye, C. M., Sanson, B., & Étienne, J. (2017). Geometry can provide long-range mechanical guidance for embryogenesis. *PLoS Computational Biology*, *13*(3), 1–30. <https://doi.org/10.1371/journal.pcbi.1005443>
- Durande, M., Tlili, S., Homan, T., Guirao, B., Graner, F., & Delanoë-Ayari, H. (2018). Fast determination of coarse grained cell anisotropy and size in epithelial tissue images using Fourier transform. *Physical Review E*, *99*(6). <https://doi.org/10.1103/PhysRevE.99.062401>
- Etournay, R., Popović, M., Merkel, M., Nandi, A., Blasse, C., Aigouy, B., Brandl, H., Myers, G., Salbreux, G., Jülicher, F., & Eaton, S. (2015). Interplay of cell dynamics and epithelial tension during morphogenesis of the *Drosophila* pupal wing. *ELife*, *4*(JUNE2015), 1–51. <https://doi.org/10.7554/eLife.07090>
- Farge, E. (2003). Mechanical induction of Twist in the *Drosophila* foregut/stomodaeal primordium. *Current Biology*, *13*(16), 1365–1377. [https://doi.org/10.1016/S0960-9822\(03\)00576-1](https://doi.org/10.1016/S0960-9822(03)00576-1)
- Farhadifar, R., Röper, J. C., Aigouy, B., Eaton, S., & Jülicher, F. (2007). The Influence of Cell Mechanics, Cell-Cell Interactions, and Proliferation on Epithelial Packing. *Current Biology*, *17*(24), 2095–2104. <https://doi.org/10.1016/j.cub.2007.11.049>
- Fehon, R. G., McClatchey, A. I., & Bretscher, A. (2010). Organizing the cell cortex: The role of ERM proteins. In *Nature Reviews Molecular Cell Biology* (Vol. 11, Issue 4, pp. 276–287). Nat Rev Mol Cell Biol. <https://doi.org/10.1038/nrm2866>
- Firmino, J., Rocancourt, D., Saadaoui, M., Moreau, C., & Gros, J. (2016). Cell Division Drives Epithelial Cell Rearrangements during Gastrulation in Chick. *Developmental Cell*, *36*(3), 249–261. <https://doi.org/10.1016/j.devcel.2016.01.007>
- Fischer-Friedrich, E., Hyman, A. A., Jülicher, F., Müller, D. J., & Helenius, J. (2014). Quantification of surface tension and internal pressure generated by single mitotic cells. *Scientific Reports*, *4*(1), 1–8. <https://doi.org/10.1038/srep06213>
- Gelbart, Michael A., He, B., Martin, A. C., Thiberge, S. Y., Wieschaus, E. F., & Kaschube, M. (2012). Volume conservation principle involved in cell lengthening and nucleus movement during tissue morphogenesis. *Proceedings of the National Academy of Sciences*, *109*(47), 19298–19303. <https://doi.org/10.1073/pnas.1205258109>
- González-Bermúdez, B., Guinea, G. V., & Plaza, G. R. (2019). Advances in Micropipette Aspiration: Applications in Cell Biomechanics, Models, and Extended Studies. *Biophysical Journal*, *116*(4), 587–594. <https://doi.org/10.1016/j.bpj.2019.01.004>
- Gracia, M., Theis, S., Proag, A., Gay, G., Benassayag, C., & Suzanne, M. (2019). Mechanical impact of epithelial–mesenchymal transition on epithelial morphogenesis in *Drosophila*. *Nature Communications* *2019 10:1*, *10*(1), 1–17. <https://doi.org/10.1038/s41467-019-10720-0>
- Graner, F., & Glazier, J. A. (1992). Simulation of biological cell sorting using a two-dimensional extended Potts model. *Physical Review Letters*, *69*(13), 2013–2016. <https://doi.org/10.1103/PhysRevLett.69.2013>
- Grumbling, G., & Strelets, V. (2006). FlyBase: anatomical data, images and queries. *Nucleic Acids Research*, *34*(Database issue), D484–D488. <https://doi.org/10.1093/nar/gkj068>
- Guirao, B., Rigaud, S. U., Bosveld, F., Bailles, A., Lopez-Gay, J., Ishihara, S., Sugimura, K., Graner, F., & Bellaiche, Y. (2015). Unified quantitative characterization of epithelial tissue development. *ELife*, *4*(DECEMBER2015), 1–52. <https://doi.org/10.7554/eLife.08519>
- Gumbiner, B. M. (2005). Regulation of cadherin-mediated adhesion in morphogenesis. *Nature Reviews Molecular Cell Biology*, *6*(8), 622–634. <https://doi.org/10.1038/nrm1699>
- Harvey Lodish, Arnold Berk, Lawrence Zipursky, Paul Matsudaira, David Baltimore, and J. D. (2000). Molecular Cell Biology - NCBI Bookshelf. In *4th edition New York W.H.Freeman & Co Ltd* (p. 1280). <https://www.ncbi.nlm.nih.gov/books/NBK21475/>
- Hayashi, T., & Carthew, R. W. (2004). Surface mechanics mediate pattern formation in the developing retina. *Nature*, *431*(7009), 647–652. <https://doi.org/10.1038/nature02952>
- Hayes, P., & Solon, J. (2017). *Drosophila* dorsal closure: An orchestra of forces to zip shut the embryo. In *Mechanisms of Development* (Vol. 144, pp. 2–10). Elsevier Ireland Ltd. <https://doi.org/10.1016/j.mod.2016.12.005>
- Hilfer, S. R., Esteves, R. A., & Sanzo, J. F. (1989). Invagination of the otic placode: Normal development and experimental manipulation. *Journal of Experimental Zoology*, *251*(2), 253–264. <https://doi.org/10.1002/jez.1402510213>
- Honda, H., & Eguchi, G. (1980). How much does the cell boundary contract in a monolayered cell sheet? *Journal of Theoretical Biology*, *84*(3), 575–588. [https://doi.org/10.1016/S0022-5193\(80\)80021-X](https://doi.org/10.1016/S0022-5193(80)80021-X)

## Bibliography

- Hufnagel, L., Teleman, A. A., Rouault, H., Cohen, S. M., & Shraiman, B. I. (2007). On the mechanism of wing size determination in fly development. *Proceedings of the National Academy of Sciences of the United States of America*, *104*(10), 3835–3840. <https://doi.org/10.1073/pnas.0607134104>
- Ingber, D. E. (2006). Cellular mechanotransduction: putting all the pieces together again. *The FASEB Journal*, *20*(7), 811–827. <https://doi.org/10.1096/fj.05-5424rev>
- Ishihara, S., Sugimura, K., Cox, S. J., Bonnet, I., Bellaïche, Y., & Graner, F. (2013). Comparative study of non-invasive force and stress inference methods in tissue. *The European Physical Journal E*, *36*(4), 45. <https://doi.org/10.1140/epje/i2013-13045-8>
- Ishihara, Shuji, & Sugimura, K. (2012). Bayesian inference of force dynamics during morphogenesis. *Journal of Theoretical Biology*, *313*, 201–211. <https://doi.org/10.1016/j.jtbi.2012.08.017>
- Jaderberg, M., Simonyan, K., Zisserman, A., & Kavukcuoglu, K. (2015). Spatial Transformer Networks. *Advances in Neural Information Processing Systems*, *2015-January*, 2017–2025. <http://arxiv.org/abs/1506.02025>
- Juanes-García, A., Llorente-González, C., & Vicente-Manzanares, M. (2018). Nonmuscle Myosin II. In *Encyclopedia of Signaling Molecules* (pp. 3541–3553). Springer International Publishing. [https://doi.org/10.1007/978-3-319-67199-4\\_101734](https://doi.org/10.1007/978-3-319-67199-4_101734)
- K, S., F, R., P, L., & E, M. (2010). Sequential activation of apical and basolateral contractility drives ascidian endoderm invagination. *Current Biology: CB*, *20*(17), 1499–1510. <https://doi.org/10.1016/J.CUB.2010.06.075>
- Käfer, J., Hayashi, T., Marée, A. F. M., Carthew, R. W., & Graner, F. (2007). Cell adhesion and cortex contractility determine cell patterning in the *Drosophila* retina. *Proceedings of the National Academy of Sciences of the United States of America*, *104*(47), 18549–18554. <https://doi.org/10.1073/pnas.0704235104>
- Kaiser, W., & Garrett, C. G. B. (1961). Two-photon excitation in CaF<sub>2</sub>: Eu<sup>2+</sup>. *Physical Review Letters*, *7*(6), 229–231. <https://doi.org/10.1103/PhysRevLett.7.229>
- Kale, G. R., Yang, X., Philippe, J., Mani, M., & Lenne, P. (2018). Two contractile pools of actomyosin distinctly load and tune E-cadherin levels during morphogenesis. <https://doi.org/doi.org/10.1101/255158>
- Kawasak, K., Naga, T., & Nakashima, K. (1989). Vertex models for two-dimensional grain growth. *Philosophical Magazine B: Physics of Condensed Matter: Statistical Mechanics, Electronic, Optical and Magnetic Properties*, *60*(3), 399–421. <https://doi.org/10.1080/13642818908205916>
- Keller, R., Davidson, L., Edlund, A., Elul, T., Ezin, M., Shook, D., & Skoglund, P. (2000). Mechanisms of convergence and extension by cell intercalation. *Philosophical Transactions of the Royal Society B: Biological Sciences*, *355*(1399), 897–922. <https://doi.org/10.1098/rstb.2000.0626>
- Krens, S. F. G. G., Veldhuis, J. H., Barone, V., Čapek, D., Maître, J.-L. L., Brodland, G. W., & Heisenberg, C.-P. P. (2017). Interstitial fluid osmolarity modulates the action of differential tissue surface tension in progenitor cell segregation during gastrulation. *Development (Cambridge)*, *144*(10), 1798–1806. <https://doi.org/10.1242/dev.144964>
- Krieg, M., Arboleda-Estudillo, Y., Puech, P. H., Käfer, J., Graner, F., Müller, D. J., & Heisenberg, C. P. (2008). Tensile forces govern germ-layer organization in zebrafish. *Nature Cell Biology*, *10*(4), 429–436. <https://doi.org/10.1038/ncb1705>
- Kuhn, H. W. (1955). The Hungarian method for the assignment problem. *Naval Research Logistics Quarterly*, *2*(1–2), 83–97. <https://doi.org/10.1002/nav.3800020109>
- Kurn, H., & Daly, D. T. (2020). Histology, Epithelial Cell. In *StatPearls*. StatPearls Publishing. <http://www.ncbi.nlm.nih.gov/pubmed/32644489>
- Lau, K., Tao, H., Liu, H., Wen, J., Sturgeon, K., Sorfazlian, N., Lazic, S., Burrows, J. T. A., Wong, M. D., Li, D., Deimling, S., Ciruna, B., Scott, I., Simmons, C., Henkelman, R. M., Williams, T., Hadjantonakis, A. K., Fernandez-Gonzalez, R., Sun, Y., & Hopyan, S. (2015). Anisotropic stress orients remodelling of mammalian limb bud ectoderm. *Nature Cell Biology*, *17*(5), 569–579. <https://doi.org/10.1038/ncb3156>
- Lecuit, T., & Lenne, P.-F. (2007). Cell surface mechanics and the control of cell shape, tissue patterns and morphogenesis. *Nature Reviews. Molecular Cell Biology*, *8*(8), 633–644. <https://doi.org/10.1038/nrm2222>
- Leptin, M., & Grunewald, B. (1990). Cell shape changes during gastrulation in *Drosophila*. *Development*, *110*(1).
- Levayer, R., & Lecuit, T. (2012). Biomechanical regulation of contractility: Spatial control and dynamics. *Trends in Cell Biology*, *22*(2), 61–81. <https://doi.org/10.1016/j.tcb.2011.10.001>
- Lomakin, A. J., Lee, K. C., Han, S. J., Bui, D. A., Davidson, M., Mogilner, A., & Danuser, G. (2015). Competition for actin between two distinct F-actin networks defines a bistable switch for cell polarization. *Nature Cell Biology*, *17*(11), 1435–1445. <https://doi.org/10.1038/ncb3246>
- Lye, C. M., Blanchard, G. B., Naylor, H. W., Muresan, L., Huisken, J., Adams, R. J., & Sanson, B. (2015). Mechanical Coupling between Endoderm Invagination and Axis Extension in *Drosophila*. *PLoS Biology*, *13*(11), 1–27. <https://doi.org/10.1371/journal.pbio.1002292>
- Ma, X., Lynch, H. E., Scully, P. C., & Hutson, M. S. (2009). Probing embryonic tissue mechanics with laser hole drilling. *Physical Biology*, *6*(3), 1–17. <https://doi.org/10.1088/1478-3975/6/3/036004>
- Maître, J. L., Berthoumieux, H., Krens, S. F. G., Salbreux, G., Jülicher, F., Paluch, E., & Heisenberg, C. P. (2012). Adhesion functions in cell sorting by mechanically coupling the cortices of adhering cells. *Science*, *338*(6104),

## Bibliography

- 253–256. <https://doi.org/10.1126/science.1225399>
- Marder, M. (1987). Soap-bubble growth. *Physical Review A*, *36*(1), 438–440. <https://doi.org/10.1103/PhysRevA.36.438>
- Marée, A. F. M., Grieneisen, V. A., & Hogeweg, P. (2007). The Cellular Potts Model and Biophysical Properties of Cells, Tissues and Morphogenesis. In *Single-Cell-Based Models in Biology and Medicine* (pp. 107–136). Birkhäuser Basel. [https://doi.org/10.1007/978-3-7643-8123-3\\_5](https://doi.org/10.1007/978-3-7643-8123-3_5)
- Marieb, E. N. B. (1989). *Human anatomy and physiology*.
- Marinari, E., Mehonic, A., Curran, S., Gale, J., Duke, T., & Baum, B. (2012). Live-cell delamination counterbalances epithelial growth to limit tissue overcrowding. *Nature*, *484*(7395), 542–545. <https://doi.org/10.1038/nature10984>
- Martin, A. C. (2020). The physical mechanisms of Drosophila gastrulation: Mesoderm and endoderm invagination. *Genetics*, *214*(3), 543–560. <https://doi.org/10.1534/genetics.119.301292>
- Martin, A. C., Gelbart, M., Fernandez-Gonzalez, R., Kaschube, M., & Wieschaus, E. F. (2010). Integration of contractile forces during tissue invagination. *Journal of Cell Biology*, *188*(5), 735–749. <https://doi.org/10.1083/jcb.200910099>
- Martin, A. C., Kaschube, M., & Wieschaus, E. F. (2009). Pulsed contractions of an actin-myosin network drive apical constriction. *Nature*, *457*(7228), 495–499. <https://doi.org/10.1038/nature07522>
- Michel, G., Tonon, T., Scornet, D., Cock, J. M., & Kloareg, B. (2010). The cell wall polysaccharide metabolism of the brown alga *Ectocarpus siliculosus*. Insights into the evolution of extracellular matrix polysaccharides in Eukaryotes. *New Phytologist*, *188*(1), 82–97. <https://doi.org/10.1111/j.1469-8137.2010.03374.x>
- Miyawaki, A. (2011). Development of Probes for Cellular Functions Using Fluorescent Proteins and Fluorescence Resonance Energy Transfer. *Annual Review of Biochemistry*, *80*(1), 357–373. <https://doi.org/10.1146/annurev-biochem-072909-094736>
- Mongera, A., Rowghanian, P., Gustafson, H. J., Shelton, E., Kealhofer, D. A., Carn, E. K., Serwane, F., Lucio, A. A., Giammona, J., & Campàs, O. (2018). A fluid-to-solid jamming transition underlies vertebrate body axis elongation. *Nature*, *561*(7723), 401–405. <https://doi.org/10.1038/s41586-018-0479-2>
- Monier, B., Gettings, M., Gay, G., Mangeat, T., Schott, S., Guarner, A., & Suzanne, M. (2015). Apico-basal forces exerted by apoptotic cells drive epithelium folding. *Nature*, *518*(7538), 245–248. <https://doi.org/10.1038/nature14152>
- Muñoz, R. F., Le, H. N., Ippen, C. G., Diaz, M. A., Urizar, G. G., Soto, J., Mendelson, T., Delucchi, K., & Lieberman, A. F. (2007). Prevention of Postpartum Depression in Low-Income Women: Development of the Mamás y Bebés/Mothers and Babies Course. *Cognitive and Behavioral Practice*, *14*(1), 70–83. <https://doi.org/10.1016/j.cbpra.2006.04.021>
- Nagai, T., & Honda, H. (2009). Computer simulation of wound closure in epithelial tissues: Cell-basal-lamina adhesion. *Physical Review E - Statistical, Nonlinear, and Soft Matter Physics*, *80*(6), 061903. <https://doi.org/10.1103/PhysRevE.80.061903>
- Narayanan, V., Schappell, L. E., Mayer, C. R., Duke, A. A., Armiger, T. J., Arsenovic, P. T., Mohan, A., Dahl, K. N., Gleghorn, J. P., & Conway, D. E. (2020). Osmotic Gradients in Epithelial Acini Increase Mechanical Tension across E-cadherin, Drive Morphogenesis, and Maintain Homeostasis. *Current Biology*, *30*(4), 624–633.e4. <https://doi.org/10.1016/j.cub.2019.12.025>
- Nishimura, T., Honda, H., & Takeichi, M. (2012). Planar cell polarity links axes of spatial dynamics in neural-tube closure. *Cell*, *149*(5), 1084–1097. <https://doi.org/10.1016/j.cell.2012.04.021>
- Okuzono, T., & Kawasaki, K. (1995). Intermittent flow behavior of random foams: A computer experiment on foam rheology. *Physical Review E*, *51*(2), 1246–1253. <https://doi.org/10.1103/PhysRevE.51.1246>
- Orr, R., De Vos, N. J., Singh, N. A., Ross, D. A., Stavrinou, T. M., & Fiatarone-Singh, M. A. (2006). Power training improves balance in healthy older adults. *Journals of Gerontology - Series A Biological Sciences and Medical Sciences*, *61*(1), 78–85. <https://doi.org/10.1093/gerona/61.1.78>
- Palavalli, A., Tizón-Escamilla, N., Rupprecht, J. F., & Lecuit, T. (2021). Deterministic and Stochastic Rules of Branching Govern Dendrite Morphogenesis of Sensory Neurons. *Current Biology*, *31*(3), 459–472.e4. <https://doi.org/10.1016/j.cub.2020.10.054>
- Pećina-Šlaus, N. (2003). Tumor suppressor gene E-cadherin and its role in normal and malignant cells. In *Cancer Cell International* (Vol. 3, Issue 1, p. 17). BioMed Central. <https://doi.org/10.1186/1475-2867-3-17>
- Petrie, R. J., Koo, H., & Yamada, K. M. (2014). Generation of compartmentalized pressure by a nuclear piston governs cell motility in a 3D matrix. *Science*, *345*(6200), 1062–1065. <https://doi.org/10.1126/science.1256965>
- Pollard, T. D., Blanchoin, L., & Mullins, R. D. (2000). Molecular Mechanisms Controlling Actin Filament Dynamics in Nonmuscle Cells. *Annual Review of Biophysics and Biomolecular Structure*, *29*(1), 545–576. <https://doi.org/10.1146/annurev.biophys.29.1.545>
- Polyakov, O., He, B., Swan, M., Shaevitz, J. W., Kaschube, M., & Wieschaus, E. (2014). Passive mechanical forces control cell-shape change during drosophila ventral furrow formation. *Biophysical Journal*, *107*(4), 998–1010. <https://doi.org/10.1016/j.bpj.2014.07.013>

## Bibliography

- Pouille, P. A., Ahmadi, P., Brunet, A. C., & Farge, E. (2009). Mechanical signals trigger myosin II redistribution and mesoderm invagination in drosophila embryos. *Science Signaling*, 2(66). <https://doi.org/10.1126/scisignal.2000098>
- Poumellec, B., Lancry, M., Chahid-Erraji, A., & Kazansky, P. G. (2011). Modification thresholds in femtosecond laser processing of pure silica: review of dependencies on laser parameters [Invited]. *Optical Materials Express*, 1(4), 766. <https://doi.org/10.1364/ome.1.000766>
- Rauzi, M., & Lenne, P. F. (2015). Probing cell mechanics with subcellular laser dissection of actomyosin networks in the early developing Drosophila embryo. *Methods in Molecular Biology*, 1189, 209–218. [https://doi.org/10.1007/978-1-4939-1164-6\\_14](https://doi.org/10.1007/978-1-4939-1164-6_14)
- Rauzi, Matteo, Verant, P., Lecuit, T., & Lenne, P. F. (2008). Nature and anisotropy of cortical forces orienting Drosophila tissue morphogenesis. *Nature Cell Biology*, 10(12), 1401–1410. <https://doi.org/10.1038/ncb1798>
- Roca-Cusachs, P., Conte, V., & Trepats, X. (2017). Quantifying forces in cell biology. *Nature Cell Biology*, 19(7), 742–751. <https://doi.org/10.1038/ncb3564>
- Roh-Johnson, M., Shemer, G., Higgins, C. D., McClellan, J. H., Werts, A. D., Tulu, U. S., Gao, L., Betzig, E., Kiehart, D. P., & Goldstein, B. (2012). Triggering a cell shape change by exploiting preexisting actomyosin contractions. *Science*, 335(6073), 1232–1235. <https://doi.org/10.1126/science.1217869>
- Rozbicki, E., Chuai, M., Karjalainen, A. I., Song, F., Sang, H. M., Martin, R., Knölker, H. J., Macdonald, M. P., & Weijer, C. J. (2015). Myosin-II-mediated cell shape changes and cell intercalation contribute to primitive streak formation. *Nature Cell Biology*, 17(4), 397–408. <https://doi.org/10.1038/ncb3138>
- Saadaoui, M., Corson, F., Rocancourt, D., Roussel, J., Statistique, L. D. P., Supérieure, E. N., & M Saadaoui, F. C. D. R. J. R. J. G. (2018). A tensile ring drives tissue flows to shape the gastrulating amniote embryo. *BioRxiv*, 33(0), 1–25.
- Sanyal, S., & Glazier, J. A. (2006). Viscous instabilities in flowing foams: A Cellular Potts Model approach. *Journal of Statistical Mechanics: Theory and Experiment*, 10, p10008. <https://doi.org/10.1088/1742-5468/2006/10/P10008>
- Serwane, F., Mongera, A., Rowghanian, P., Kealhofer, D. A., Lucio, A. A., Hockenbery, Z. M., & Campàs, O. (2017). In vivo quantification of spatially varying mechanical properties in developing tissues. *Nature Methods*. <https://doi.org/10.1038/nmeth.4101>
- Shivakumar, P. C., & Lenne, P.-F. (2016). *Laser Ablation to Probe the Epithelial Mechanics in Drosophila BT - Drosophila: Methods and Protocols* (C. Dahmann (ed.); pp. 241–251). Springer New York. [https://doi.org/10.1007/978-1-4939-6371-3\\_14](https://doi.org/10.1007/978-1-4939-6371-3_14)
- Sinha, B., Köster, D., Ruez, R., Gonnord, P., Bastiani, M., Abankwa, D., Stan, R. V., Butler-Browne, G., Védie, B., Johannes, L., Morone, N., Parton, R. G., Raposo, G., Sens, P., Lamaze, C., & Nassoy, P. (2011). Cells respond to mechanical stress by rapid disassembly of caveolae. *Cell*, 144(3), 402–413. <https://doi.org/10.1016/j.cell.2010.12.031>
- Steinberg, M. S. (1996). Adhesion in development: An historical overview. *Develop. Biol.*, 180(0312), 377–388.
- Sugimura, K., Lenne, P. F., & Graner, F. (2016). Measuring forces and stresses in situ in living tissues. *Development (Cambridge)*, 143(2), 186–196. <https://doi.org/10.1242/dev.119776>
- Sui, L., Alt, S., Weigert, M., Dye, N., Eaton, S., Jug, F., Myers, E. W., Jülicher, F., Salbreux, G., & Dahmann, C. (2018). Differential lateral and basal tension drive folding of Drosophila wing discs through two distinct mechanisms. *Nature Communications* 2018 9:1, 9(1), 1–13. <https://doi.org/10.1038/s41467-018-06497-3>
- Suzanne, M., & Steller, H. (2013). Shaping organisms with apoptosis. In *Cell Death and Differentiation* (Vol. 20, Issue 5, pp. 669–675). Nature Publishing Group. <https://doi.org/10.1038/cdd.2013.11>
- Svoboda, K., & Block, S. M. (1994). Biological applications of optical forces. In *Annual Review of Biophysics and Biomolecular Structure* (Vol. 23, pp. 247–285). Annual Reviews Inc. <https://doi.org/10.1146/annurev.bb.23.060194.001335>
- Tabata, T., & Takei, Y. (2004). Morphogens, their identification and regulation. *Development*, 131(4), 703–712. <https://doi.org/10.1242/dev.01043>
- Tetley, R. J., Blanchard, G. B., Fletcher, A. G., Adams, R. J., & Sanson, B. (2016). Unipolar distributions of junctional myosin II identify cell stripe boundaries that drive cell intercalation throughout drosophila axis extension. *ELife*, 5(MAY2016). <https://doi.org/10.7554/eLife.12094>
- Tinevez, J. Y., Schulze, U., Salbreux, G., Roensch, J., Joanny, J. F., & Paluch, E. (2009). Role of cortical tension in bleb growth. *Proceedings of the National Academy of Sciences of the United States of America*, 106(44), 18581–18586. <https://doi.org/10.1073/pnas.0903353106>
- Townes, P. L., & Holtfreter, J. (1955). Directed movements and selective adhesion of embryonic amphibian cells. *Journal of Experimental Zoology*, 128(1), 53–120. <https://doi.org/10.1002/jez.1401280105>
- Tsukita, S., & Furuse, M. (1999). Occludin and claudins in tight-junction strands: Leading or supporting players? In *Trends in Cell Biology* (Vol. 9, Issue 7, pp. 268–273). Elsevier Ltd. [https://doi.org/10.1016/S0962-8924\(99\)01578-0](https://doi.org/10.1016/S0962-8924(99)01578-0)
- Vale, R. D., & Milligan, R. A. (2000). The way things move: Looking under the hood of molecular motor proteins. In

## Bibliography

- Science* (Vol. 288, Issue 5463, p. 88). American Association for the Advancement of Science. <https://doi.org/10.1126/science.288.5463.88>
- Walck-Shannon, E., & Hardin, J. (2014). Cell intercalation from top to bottom. In *Nature Reviews Molecular Cell Biology* (Vol. 15, Issue 1, pp. 34–48). NIH Public Access. <https://doi.org/10.1038/nrm3723>
- Wang, X., Merkel, M., Sutter, L. B., Erdemci-Tandogan, G., Manning, M. L., & Kasza, K. E. (2020). Anisotropy links cell shapes to tissue flow during convergent extension. *Proceedings of the National Academy of Sciences of the United States of America*, *117*(24), 13541–13551. <https://doi.org/10.1073/pnas.1916418117>
- Yin, C., Kiskowski, M., Pouille, P. A., Farge, E., & Solnica-Krezel, L. (2008). Cooperation of polarized cell intercalations drives convergence and extension of presomitic mesoderm during zebrafish gastrulation. *Journal of Cell Biology*, *180*(1), 221–232. <https://doi.org/10.1083/jcb.200704150>
- Zallen, J. A., & Wieschaus, E. (2004). Patterned gene expression directs bipolar planar polarity in *Drosophila*. *Developmental Cell*, *6*(3), 343–355. [https://doi.org/10.1016/S1534-5807\(04\)00060-7](https://doi.org/10.1016/S1534-5807(04)00060-7)